CABARET Schemes for improved wave propagation and viscous flow modelling

Submitted in partial fulfilment of the requirements of the Degree of

Doctor of Philosophy

in the

School of Engineering and Materials Science

Queen Mary University of London

by

Abhishek Chintagunta

Supervisor: Dr. Sergey Karabasov

January, 2019

"This thesis is dedicated to my God and Saviour Jesus Christ."

Jesus also told this parable to some who trusted in themselves that they were righteous, and treated others with contempt: "Two men went up into the temple to pray, one a Pharisee and the other a tax collector. The Pharisee, standing by himself, prayed thus: 'God, I thank you that I am not like other men, extortioners, unjust, adulterers, or even like this tax collector. I fast twice a week; I give tithes of all that I get.' But the tax collector, standing far off, would not even lift up his eyes to heaven, but beat his breast, saying, 'God, be merciful to me, a sinner!' I tell you, this man went down to his house justified, rather than the other. For everyone who exalts himself will be humbled, but the one who humbles himself will be exalted." Luke 18, The Bible.

Declaration

I, Abhishek Chintagunta, confirm that the research included within this thesis is my own work or that where it has been carried out in collaboration with, or supported by others, that this is duly acknowledged below and my contribution indicated. Previously published material is also acknowledged below.

I attest that I have exercised reasonable care to ensure that the work is original, and does not to the best of my knowledge break any UK law, infringe any third party's copyright or other Intellectual Property Right, or contain any confidential material.

I accept that the College has the right to use plagiarism detection software to check the electronic version of the thesis.

I confirm that this thesis has not been previously submitted for the award of a degree by this or any other university.

The copyright of this thesis rests with the author and no quotation from it or information derived from it may be published without the prior written consent of the author.

Signature: Abhishek Chintagunta

Date: 28th January, 2019

List of publications:

1. Flux-corrected dispersion-improved CABARET schemes for linear and nonlinear wave propagation problems, A Chintagunta, SE Naghibi, SA Karabasov, Computers & Fluids, 2018.

2. CABARET Schemes for improved wave propagation and viscous flow modelling, The Russell Binions Memorial PhD Research Symposium, Queen Mary university of London, London, 2018.

3. Dispersion Improved CABARET for Computational Aeroacoustics, Abhishek Chintagunta, Anton Markesteijn, Seyedeh Elnaz Naghibi, Sergey A Karabasov, 23rd AIAA CEAS Aeroacoustics Conference, 2017.

4. A dispersion improved CABARET Scheme for linear acoustic propagation problems, S.A. Karabasov, Abhishek Chintagunta, Fourth International Workshop Computational Experiment in Aeroacoustics CEAA, 2016.

Abstract

The dispersion improved Compact Accurately Boundary Adjusting high-REsolution Technique (CABARET) schemes are presented as an upgrade of the original CABARET for improved wave propagation modeling. The new modification retains many attractive features of the original CABARET scheme such as shock-capturing and low dissipation. It is simple for implementation in the existing CABARET codes and leads to greater accuracy for solving linear wave propagation problems. A non-linear version of the dispersion-improved CABARET scheme is introduced to deal with contact discontinuities and shocks efficiently. The properties of the new linear and nonlinear CABARET schemes are analyzed for numerical dissipation and dispersion error based on Von Neumann analysis. The properties of the new linear and nonlinear CABARET schemes are demonstrated for one-dimensional, two-dimensional, and three-dimensional flows. Furthermore, the viscous terms in the full three-dimensional CABARET unstructured Navier-Stokes solver have been updated from the vertex approach to the collocated approach, resulting in efficient computational time.

Acknowledgements

I want to thank Dr Sergey Karabasov the foremost for his invaluable help, support and patience for the entire time during my PhD study. This thesis is not possible without his knowledge in the subject and the expertise in research. Dr Sergey is a kind and generous person and is worthy of imitation. It has been my honour to be his student.

I would like to also thank Dr Anton, Dr Elnaz, and Dr Vasily, for their helpful input in the present work.

Secondly, I would like to thank my wife Mercy for her constant support and help. And my parents-in-law who were a constant source of prayer, support, and help. I would like to thank the Church family at SREC, Southampton, who are a family to us away from home.

Finally, I would like to thank Anuroopa Kalyan and Saqib for their companionship at the University and making it a fun and pleasant experience.

Table of Contents

List of Figures

List of Tables

Chapter 1

Introduction and Literature review

Aerodynamic noise generated by an aircraft is a major concern for designers. Notably, during take-off and landing the noise pollution affects the communities in and around airports. Hence, stringent noise reduction requirements for aircraft are updated continuously by the International Civil Aviation Organization (ICAO), as newer permissible thresholds (a 10dB reduction by the year 2020 with respect to the noise levels in the year 2000) for noise levels are being defined (Leylekian et al., 2014). For example, the noise generated by the airframe and jet is a significant contributor to external noise emission. Therefore, for optimal aircraft designs, more quantitative noise predictions are needed for components such as the wing, the propeller fan, and the nozzle (Tam, 2004; Zaman et al., 2011).

1.1 Motivation

Broadly, the numerical approach to analyse aerodynamic noise is known as Computational Aero-Acoustics (CAA). Following Wagner et al. (2007), and Colonius and Lele (2004), CAA methods are broadly classified into two groups, direct methods, and hybrid methods.

The direct methods are similar to Direct Numerical Simulation (DNS) in Computational Fluid Dynamics (CFD). Here, the full compressible Navier-Stokes equations are solved for the flow field and the acoustic field. Analogously, these methods need substantial computational resources, due to a large number of cells or points needed for the large domain extending to the observer. Furthermore, many CFD schemes, which are designed to solve the near-field

problem (i.e., close to the body or surface of geometry), have high dispersion and dissipation errors which distort and damp the acoustic waves in the far-field. Briefly, the dispersion and the dissipation errors in the numerical scheme correspond to the errors in phase and the errors in magnitude of a wave. As shown in Figure 1.1, the dissipation error accounts for the error in computing the amplitude of the sinusoidal wave, and the dispersion error corresponds to the error in computing the phase of the sinusoidal wave.

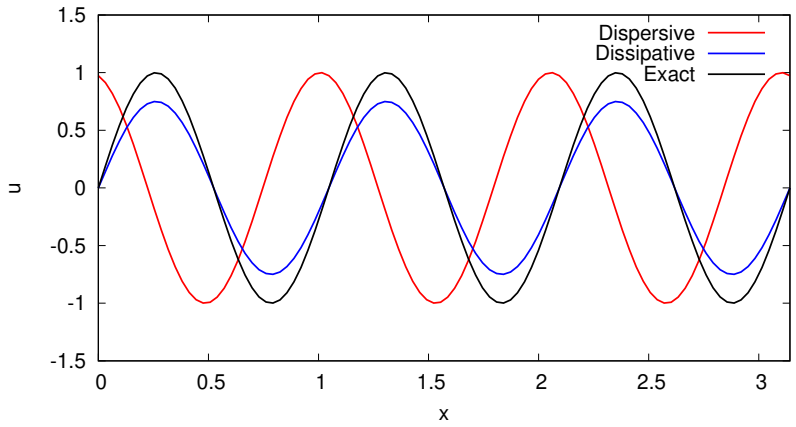

Figure 1.1: Numerical errors in computing a sinusoidal wave.

The hybrid methods use a model decomposition to decouple the aerodynamic field in the near-field and the acoustic waves in the far-field. This leads to a combination of methods which transport the acoustic waves in the far-field and the sound generating aerodynamic field in the near-field. The decoupling is possible because the flow-field can be thought of as the superimposing of the aerodynamic field and the acoustic field. Accurate methods for solving the governing Navier-Stokes (NS) equations play an essential role in CAA. For efficiency, the underlying CFD schemes involved should have low dispersion, and dissipation to not distort or dampen the acoustic waves, as well as, remain practical to handle complex flows (such as shock-capturing) and geometries (such as a simple computational stencil). The present work of the thesis is aimed to

improve the dispersion properties of the CABARET scheme, which can satisfy both these requirements.

Generally, the NS governing equations consist of advection, viscous, and source terms. The following section 1.2.1 briefly reviews the progress, although not exhaustive, of different numerical methods focused on the advection methods.

1.2 Literature review

1.2.1 Advection modelling methods

The wave propagation phenomena of the hydrodynamic and the acoustic waves in aero-acoustics involve capturing the large disparity of scales from turbulence to acoustic waves. The numerical methods that are used to compute these waves efficiently are required to preserve a wide range of fluid and acoustic features. This includes preserving the phase and amplitude of small acoustic perturbations, which are typically few orders of magnitude or smaller than the hydrodynamic waves, and the capturing of non-linearities in flow, such as shocks.

For a given fluid flow problem, several numerical methods may be employed to compute the numerical solution accurately. However, the requirements for solving computational aero-acoustics (CAA) problems differ significantly from the typical aerodynamic problems which use general CFD numerical methods. Some significant considerations, as stated by Lele (1997); Tam (1995), are as follows.

Firstly, aerodynamic problems of interest typically correspond to small reduced frequencies where other phenomena such as smaller high-frequency turbulence waves, are represented by averaging. Aero-acoustic problems have a wide range of frequencies, especially high-frequency waves with extremely

small wavelengths, in accordance with the human hearing range that spans from 200Hz to 4kHz. The space-time distribution of interfering acoustic waves is needed to compute the intensity of far-field sound which is relevant for engineering aeroacoustic problems of aircraft noise certification. Secondly, the amplitude of the acoustic waves are typically three to four order of magnitude lower than the amplitude of the aerodynamic pressure variation of the flow, hence, can be easily smeared by numerical dissipation. These conditions imply that the numerical method should have both low dissipation and dispersion properties for wave propagation modelling. A useful measure of wave propagation properties for computational schemes in CAA is the number of grid points (or degrees of freedom) per wavelength (ppw) required to preserve a certain accuracy. Conventional CFD methods typically use large PPW counts (more than 20 for second-order schemes) resulting in large computational grids. In comparison to aero-acoustic specific numerical methods which use smaller grids, as they need lesser PPW (typically around 6-8 or less) (Bogey and Bailly, 2004; Haider et al., 2015).

Also, CAA problems which involve both the linear wave propagation and the non-linear wave phenomena it is desirable to have a high-resolution scheme. This means that the scheme is able to achieve a second or higher order of accuracy in the smooth parts with less PPW, and able to capture discontinuities with few grid points free from any spurious oscillations (Harten, 1983), in addition to low dispersion and dissipation. All these requirements lead to the fundamental CFD problem of how to mitigate the problems arising from dispersion and diffusion errors in the schemes, without compromising the stability and accuracy for non-linear flows. An example of a linear wave progressing to a non-linear wave as it travels in the x-direction is shown in Figure 1.2. In this example, a linear wave steepens (i.e. accelerates at the apex of the wave) as it travels, thereby having a sudden jump in velocity (u). The steep region of the wave accelerates further as it eventually catches up and overtake the wave in front of it to form a

non-linear or discontinuities region. A prime example of the non-linear region is the shock formation.

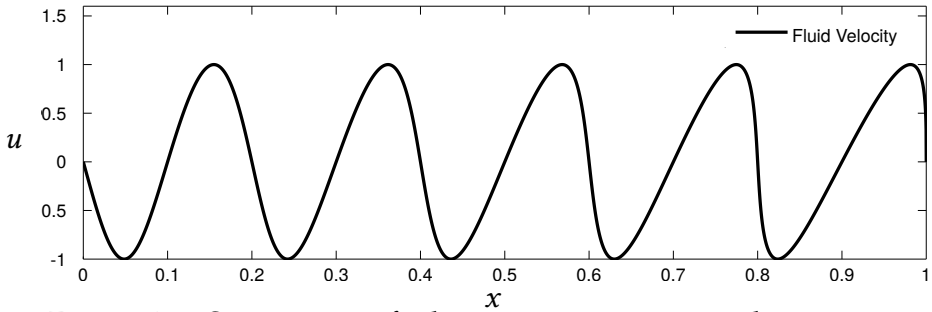

Figure 1.2: Steepening of a linear wave into a non-linear wave.

The different numerical methods which have been used to resolve the near field aerodynamic source in CAA are based on Finite-Difference (FD), Finite-Volume (FV) and Finite-Element methods (FE). A brief overview of each method is presented as follows.

Firstly, the FD methods have been the choice scheme, owing to their ease of implementation for simple grids and in extending the schemes to high-order accuracy, both to spatial and temporal terms in the governing equations. These schemes have the advantage of the aforementioned desirable properties to solve wave propagation problems. The Dispersion Relation Preserving (DRP) explicit scheme by Tam and Webb (1993a), showed that the choice of stencil coefficients for the spatial discretisation terms led to significant error reduction in dispersion compared to the same spatial ordered central scheme. This error reduction in the dispersion is reflected in the accuracy of the scheme at high wavenumbers, i.e., for high-frequency wave propagation.

Although the above scheme is limited to structured grids, efforts have been made to extend its application. Specifically, the DRP scheme has been applied to block structured grids (Huang et al., 2008) and overset grids (Schoenwald et al., 2007). Alternatively, a family of explicit high-order Bogey and Bailly (2004) proposed FD schemes of order 8, 10 and 12 using 9, 11 and 13 points in the stencil, respectively. It was primarily to achieve spectral-like resolution aimed

at Large Eddy Simulations (LES). Moreover, the scheme was enhanced to handle shocks (Bogey et al., 2009) by introducing a shock sensor to detect shocks.

Nevertheless, the above-mentioned types of grid generation methods require specialised knowledge or extra effort to avoid loss in solution accuracy. The grid generation in multiple blocks require specialist knowledge and also, are difficult to generate for complex geometries. Furthermore, grid generation using the overset method requires sophisticated post-processing to figure out the regions to be deleted or cut-out to obtain the actual flow field (Liseikin, 1999). Additionally, these grids may result in numerical instability in non-linear regions of the flow. One of the significant aspects of the above high-order schemes is the large stencil and the complexity of their implementation for complex geometries leading to non-uniform grids.

Another popular scheme to consider is the Weighted Essentially Non-Oscillatory (WENO) method. WENO is a high-resolution scheme (Harten et al., 1997), which can be applied to complex grids. However, due to its long stencil to obtain high-order accuracy, the scheme incurs high computational costs on unstructured grids. Such schemes can also have additional overheads for massively parallel calculations with a limited memory per processor, for example, vector-processing units like Graphics Processing Units (GPU) which demand a minimal memory footprint to avoid latency in calculations.

Secondly, the FE methods based on Discontinuous Galerkin (DG) schemes (Cockburn et al., 2000) are a class of high-order schemes which can be easily applied to complex grids. Although the small stencil is an attractive feature of the DG schemes, the Courant-Friedrichs-Lewy (CFL) number is severely restricted, as it is inversely proportional to the order of the scheme (Dumbser et al., 2014). This restriction on the time-step makes them very expensive for solving unsteady problems such as in CAA, which comprise a wide range of frequencies. Furthermore, the pre-conditioning of the system of equations is an active

field of research (Smears, 2016).

On the other hand, FV methods of second-third order of accuracy remain an attractive alternative to high-order methods for the ease of their implementation for industrial CAA problems. Second-order FD high-resolution scheme, CABARET (Compact Accurately Boundary Adjusting high-REsolution Technique), which is non-dissipative (when flux-limiters are not used) and low-dispersion over a wide range of CFL numbers (Karabasov and Goloviznin, 2009). CABARET has low-computational cost compared to the above mentioned high-order methods, due to its compact one-cell stencil for linear advection, and is also fully discrete, i.e., in both space and time. Furthermore, the scheme is directly adapted to the finite-volume (FV) framework and hence, can handle complex geometries. The present work is devoted to the further development of the CABARET method. Mainly, the improvement in wave propagation properties of the original CABARET scheme within a finite-volume approach applicable to general CAA and CFD problems is the focus of the present research.

1.3 Novelty

The thesis contains original contributions as follows:

- The existing dispersion scheme of Goloviznin and Samarskii (1998a) was focused on the one-step three-level CABARET scheme and was applied for the one-dimensional linear equation. The present work has extended this to the two-level predictor-corrector CABARET scheme, which is suitable for finite-volume implementation. Furthermore, this was generalised for a multi-dimensional case with systems of equations (gas dynamics) (Chintagunta et al., 2017).
- A non-linear version of the dispersion improved scheme is introduced to efficiently deal with discontinuities, as discussed in section 2.3. The ef-

ficiency of the new scheme has been demonstrated for linear advection equation, isothermal gas dynamics equations, and the Euler equations, in chapter 4.

- The dispersion improved scheme for linear wave propagation has been demonstrated as fourth-order accurate in linear advection test. This was also shown through the Taylor series analysis following a similar analysis of Danilin (2013). This has been presented in section 2.2.

- The viscous modelling of the laminar viscous stresses of the CABARET MILES solver have been upgraded from the method used in Faranosov et al. (2013a) to a more efficient Collocated approach, as presented in section 3.1.

The outline of the thesis is as follows. The next chapter presents the improvements to the standard CABARET scheme concerning the wave propagation properties. The discussion on the viscous terms modelling along with the suitable formulation is presented in Chapter 3. Following which, Chapter 4 presents the numerical results demonstrating the performance of the dispersion improved scheme in comparison with several existing schemes as well the improvement in viscous modelling for various problems.

Chapter 2

Dispersion improved CABARET schemes

The present Chapter describes the CABARET schemes and the new dispersion improved variant in section 2.1 (Karabasov and Goloviznin, 2009). This is presented for the scalar conservation law, i.e., the advection equation. Furthermore, the different non-linear correction procedures are presented in section 2.3 (Chintagunta et al., 2017) and the related dispersion term correction is discussed in section 2.3.1. Finally, the extension of the above schemes to the hyperbolic conservation law, i.e., the Euler equations are presented in section 2.5.

2.1 Linear CABARET scheme

The CABARET scheme is a conservative finite-difference scheme and is a single-step scheme on compact stencil of one- cell. It is based on a compact formulation of the second-order Upwind Leapfrog (UL) scheme (Goloviznin and Samarskii, 1998a,b; Karabasov, 2007) by introducing separate conservation and flux variables and is fully discrete in space and time. Let us consider the scalar conservation law for conservation variable u and flux variable f (where $f = f(u)$)

$$\frac{\partial u}{\partial t} + \frac{\partial f}{\partial x} = 0 \tag{2.1}$$

The above equation is considered on a finite-difference stencil as shown in Figure 2.1. The grid is both non-uniform in space (with spacing $\Delta x_j = x_{j+\frac{1}{2}} - x_{j-\frac{1}{2}}$) and time (with time-step of $\Delta t_{n+\frac{1}{2}} = t_{n+1} - t_n$) about a point j corresponding to the conservative variables, and the flux variables f at half steps.

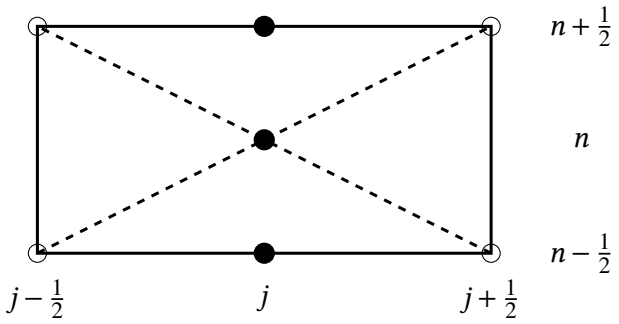

Figure 2.1: The 1D CABARET stencil, the conservative variables are at solid circles and the flux variables at the open circles.

Assuming the availability of n^{th} time-step variables, a predictor step with half-time step can be written using forward-time central space approximation as

$$\frac{u_j^{n+\frac{1}{2}} - u_j^n}{\frac{1}{2}\Delta t^{n+\frac{1}{2}}} + \frac{f_{j+\frac{1}{2}}^n - f_{j-\frac{1}{2}}^n}{\Delta x_j} = 0 \tag{2.2}$$

Following this, the $(n+1)^{th}$ time-step variables can be evaluated in the corrector step using the backward-time central-space approximation as

$$\frac{u_j^{n+1} - u_j^{n+\frac{1}{2}}}{\frac{1}{2}\Delta t^{n+\frac{1}{2}}} + \frac{f_{j+\frac{1}{2}}^{n+1} - f_{j-\frac{1}{2}}^{n+1}}{\Delta x_j} = 0 \tag{2.3}$$

The flux unknowns $f_{j+\frac{1}{2}}^{n+1}$ and $f_{j-\frac{1}{2}}^{n+1}$ are evaluated by a simple upwind extrapolation, assuming that the sign of the wave speed is constant temporarily, as

$$\begin{aligned} u_{j+\frac{1}{2}}^{n+1} &= 2u_j^{n+\frac{1}{2}} - u_{j-\frac{1}{2}}^n, \text{if} \quad \frac{\partial f}{\partial u} > 0 \\ u_{j+\frac{1}{2}}^{n+1} &= 2u_{j+1}^{n+\frac{1}{2}} - u_{j-\frac{3}{2}}^n, \text{if} \quad \frac{\partial f}{\partial u} < 0 \end{aligned} \tag{2.4}$$

The equations (2.11) to (2.4) constitute the CABARET scheme, and is an explicit single-step method. Because of the compact computational stencil CABARET retains its second-order approximation for non-uniform spatial and

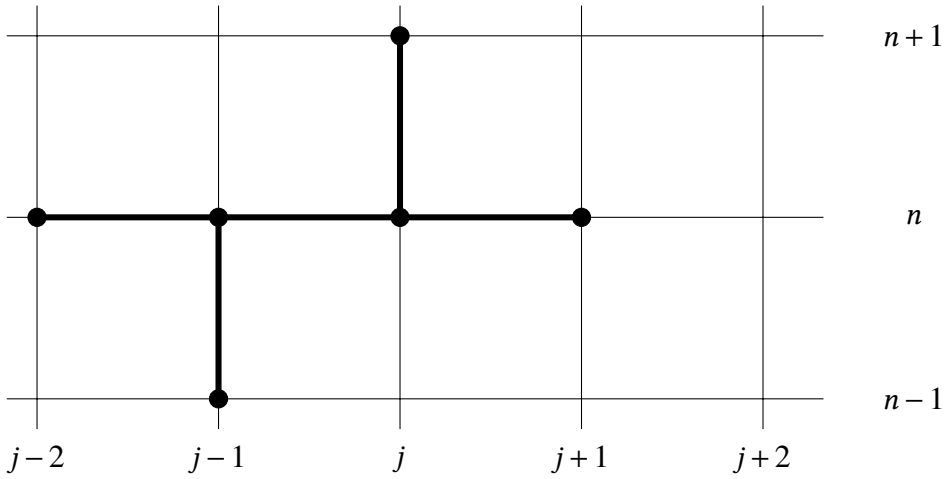

Figure 2.2: The 1D CABARET dispersion stencil, the thick lines represent the new dispersion stencil.

temporal grids, for sufficient accurate evaluation of the flux variables. The non-linear correction to make the above scheme non-oscillatory is presented in section 2.3.

2.1.1 Dispersion improved CABARET scheme

The dispersion improved version of CABARET scheme (referred with a suffix DISP) was proposed by Goloviznin and Samarskii (1998b) for the linear advection equation with constant wave speed (c). The dispersion improvement was achieved by adding an anti-dispersion correction term to the predictor and the corrector steps. Let us consider the non-staggered three-level finite-difference CABARET scheme.

$$\frac{u_j^{n+1} - u_j^n}{2\Delta t^n} + \frac{u_{j-1}^n - u_{j-1}^{n-1}}{2\Delta t^n} + \frac{f_j^n - f_{j-1}^n}{\Delta x_j} = 0 \tag{2.5}$$

The dispersion improvement is introduced by modifying the flux function to include a second-order term proportional to the third derivative of (f) in space for the stencil shown in Figure 2.2.

$$f_j^n \rightarrow f_j^n = f(u_j^n) + \delta f_j^n \tag{2.6}$$

The anti-dispersion term δf_j^n is evaluated as

$$\delta f_j^n = -\frac{\mu_j}{\Delta \bar{x}_j}\left[\frac{f_{j+1}^n - f_j^n}{\Delta x_{j+1}} - \frac{f_j^n - f_{j-1}^n}{\Delta x_j}\right] \tag{2.7}$$

$$\Delta \bar{x}_j = \frac{1}{2}\left(\Delta x_{j+1} + \Delta x_j\right) \tag{2.8}$$

$$\mu_j = \epsilon_d \left(\Delta {x_{j+1}}^2 - 3\mathrm{CFL}_j \Delta x_j \Delta \bar{x}_j + 2\mathrm{CFL}_j^2 \Delta x_j^2\right) \tag{2.9}$$

Here, CFL_j is the local CFL number (given by $\mathrm{CFL} = \frac{c\Delta t^n}{\Delta x_j}$) for cell (j) at time (n) and ϵ_d is a tunable calibration parameter whose optimum value can be evaluated analytically based on spectral analysis presented in section 2.1.2.

Furthermore, the coefficient of dispersion (μ) for uniform grid spacing and constant time step, becomes

$$\mu = \epsilon_d \Delta x^2 (1 - \mathrm{CFL})(1 - 2\mathrm{CFL}) \tag{2.10}$$

At CFL = $0.5, 1$ the coefficient of dispersion (μ_j) becomes zero. This corresponds to the CFL numbers at which the original CABARET scheme is exact for linear advection equation. Also, this flux derivative addition still retains zero-dissipation error of the original CABARET scheme as will be demonstrated in the next sections. It is useful also to note the dispersion improved CABARET scheme applied to the staggered grid for the stencil shown in Figure 2.3. The predictor-corrector steps along with the extrapolation can be written for the cell (j) as follows.

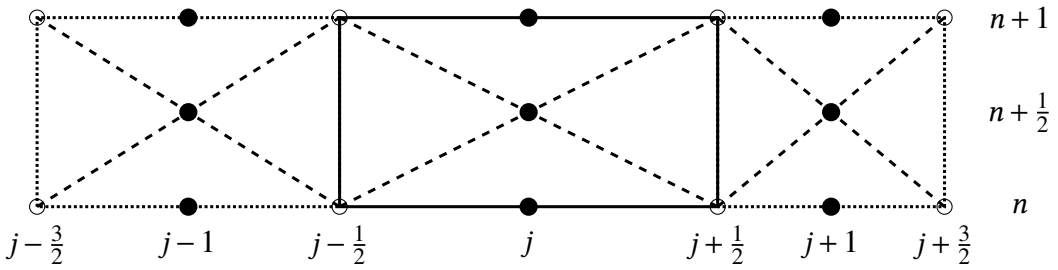

Figure 2.3: The 1D CABARET dispersion stencil, the dotted lines represent the new dispersion stencil.

$$\frac{u_j^{n+\frac{1}{2}} - u_j^n}{0.5\Delta t^n} + \frac{f_{j+\frac{1}{2}}^n - f_{j-\frac{1}{2}}^n}{\Delta x_j} = 0 \tag{2.11}$$

$$\frac{u_j^{n+1} - u_j^n}{0.5\Delta t^n} + \frac{f_{j+\frac{1}{2}}^{n+1} - f_{j-\frac{1}{2}}^{n+1}}{\Delta x_j} = 0 \tag{2.12}$$

$$f_{j+\frac{1}{2}} \to f_{j+\frac{1}{2}} + \delta f_{j+\frac{1}{2}}; \quad \delta f_{j+\frac{1}{2}} = \frac{\mu_j}{\bar{\Delta x_j}} \left[\frac{f_{j+\frac{1}{2}} - f_{j-\frac{1}{2}}}{\Delta x_j} - \frac{f_{j-\frac{1}{2}} - f_{j-\frac{3}{2}}}{\Delta x_{j-1}} \right] \tag{2.13}$$

here, $\Delta x_j = 0.5(\Delta x_j + \Delta x_{j-1})$. Also, depending on the direction of the wave propagation i.e., sign of $\frac{df}{du}$, the extrapolation step can be written as

$$\begin{aligned} \frac{df}{du} > 0: \quad m, M &= min, max(u_{j-\frac{1}{2}}^n, 2u_j^n, u_{j+\frac{1}{2}}^n), \\ u_{j+\frac{1}{2}}^{n+1} &= median(m, 2u_j^n - u_{j-\frac{1}{2}}^n, M) \end{aligned} \tag{2.14}$$

$$\begin{aligned} \frac{df}{du} < 0: \quad m, M &= min, max(u_{j+\frac{1}{2}}^n, 2u_{j+1}^n, u_{j+\frac{3}{2}}^n), \\ u_{j+\frac{1}{2}}^{n+1} &= median(m, 2u_{j+1}^n - u_{j+\frac{3}{2}}^n, M) \end{aligned} \tag{2.15}$$

As shown, the computational stencil of the dispersion improved CABARET for the one-dimensional advection equation involves 3 space-time cells compared to the standard CABARET which takes just 1 cell. The difference becomes less for applications which involve characteristics of opposite signs meeting at the same cell face, e.g., gas dynamics, where the dispersion improved CABARET

still involves 3 cells while the standard CABARET stencil extends to 2 cells.

Furthermore, when solving equations of a convection-diffusion-type, where the diffusion approximation for CABARET typically involves cell-center variables (Faranosov et al., 2013a), the computational stencil becomes 3 cells in each coordinate direction for both versions of the CABARET algorithm. The dissipation and dispersion properties of the dispersion improved CABARET scheme have been presented in the following section for the linear advection equation.

2.1.2 Linear spectral analysis

The Von Neumann stability analysis (Hirsch, 2007) has been applied to the three-time-level form of the advection equation (2.5) to assess its dissipation and dispersion properties. The dispersion improved CABARET scheme for a grid of constant spacing in space (Δx) and time step (Δt) and a constant wave speed (c) can be written in the final form as

$$\frac{u_j^{n+1}-u_j^n}{2\Delta t}+\frac{u_{j-1}^n-u_{j-1}^{n-1}}{2\Delta t}+\frac{(f_j^n+\delta f_j^n)-(f_{j-1}^n+\delta f_{j-1}^n)}{\Delta x}=0 \tag{2.16}$$

$$\frac{u_j^{n+1}-u_j^n}{2\Delta t}+\frac{u_{j-1}^n-u_{j-1}^{n-1}}{2\Delta t}+c\frac{u_j^n-u_{j-1}^n}{\Delta x}= \frac{c\mu}{\Delta x^3}\left[(u_{j+1}^n-2u_j^n+u_{j-1}^n)-(u_j^n-2u_{j-1}^n+u_{j-2}^n)\right] \tag{2.17}$$

For the linear advection equation, a travelling wave with wavenumber k and frequency ω of the form $u_j^n=e^{i(\omega n\Delta t+kj\Delta x)}$ is sought as a partial solution. On substitution the equation (2.17) becomes

$$e^{-ikj\Delta x}\frac{e^{i\omega(n+1)\Delta t}-e^{i\omega n\Delta t}}{2\Delta t}+e^{-ik(j-1)\Delta x}\frac{e^{i\omega n\Delta t}-e^{i\omega(n-1)\Delta t}}{2\Delta t}+$$
$$ce^{i\omega n\Delta t}\frac{e^{-ikj\Delta x}-e^{-ik(j-1)\Delta x}}{\Delta x}=\frac{\mu c}{\Delta x^3}e^{i\omega n\Delta t}\left(e^{-ik(j+1)\Delta x}-2e^{-ikj\Delta x}+e^{-ik(j-1)\Delta x}\right)-$$
$$\frac{\mu c}{\Delta x^3}\left(e^{-ikj\Delta x}-2e^{-ik(j-1)\Delta x}+e^{-ik(j-2)\Delta x}\right) \quad (2.18)$$

$$g^2-g\left[(1-2\mathrm{CFL})(1-h)+\frac{2\mu\mathrm{CFL}}{\Delta x^2}\left(h^{-1}-3+3h-h^2\right)\right]-h=0 \quad (2.19)$$

where, $h=e^{ik\Delta x}$, and $g=e^{i\omega\Delta t}$. This is the characteristic equation which can be simplified further as

$$g^2-gh^{\frac{1}{2}}\left[(1-2\mathrm{CFL})(h^{-\frac{1}{2}}-h^{\frac{1}{2}})+\frac{2\mu\mathrm{CFL}}{\Delta x^2}\left(h^{-\frac{1}{2}}-h^{\frac{1}{2}}\right)^3\right]-h=0 \quad (2.20)$$

The roots of the equation solving for g are

$$g=\frac{1}{2}h^{\frac{1}{2}}\left(id+\sqrt{4-d^2}\right)=h^{\frac{1}{2}}e^{i\theta},\text{where } \theta=arcsin(\frac{d}{2}) \quad (2.21)$$

here, $d=\left[-2(1-2\mathrm{CFL})sin\frac{k\Delta x}{2}+16\mathrm{CFL}\frac{\mu}{\Delta x^2}sin^3\frac{k\Delta x}{2}\right]$, and θ is real if $4-d^2\geq 0$.

Notably with $\mu=0$ in equation (2.19) we can recover the characteristic equation (denoted by subscript $cabaret$) of the original CABARET scheme as

$$g_{cabaret}^2-g_{cabaret}\left[(1-2\mathrm{CFL})(1-h)\right]-h=0 \quad (2.22)$$

The roots of this characteristic equation are

$$g_{cabaret}=\frac{1}{2}h^{\frac{1}{2}}\left(id_{cabaret}+\sqrt{4-d_{cabaret}^2}\right)=h^{\frac{1}{2}}e^{i\theta_{cabaret}} \quad (2.23)$$

where, $\theta_{cabaret}=arcsin(\frac{d_{cabaret}}{2})$ and $d_{cabaret}=\left[-2(1-2\mathrm{CFL})sin\frac{k\Delta x}{2}\right]$.

Substituting μ from equation (2.9) in the inequality to satisfy the necessary

condition of non-dissipative scheme yields

$$-1 \leq -(1-2\text{CFL}) + 8\epsilon_d(1-\text{CFL})(1-2\text{CFL})\text{CFL} \leq 1 \tag{2.24}$$

$$e(\text{CFL}) = (1-2\text{CFL})[8\epsilon_d\text{CFL}(1-\text{CFL}) - 1] \tag{2.25}$$

The above equation is a cubic polynomial function $e(\text{CFL})$ with $0 \leq \text{CFL} \leq 1$. The function $e(\text{CFL})$ passes through ($e(1) = 1, e(0) = -1, e(\frac{1}{2}) = 0$) for any given value of ϵ_d, and with $\text{CFL} = \frac{1}{2}$ as its inflection point. The next step would be to find the optimal value of ϵ_d to satisfy the inequality. For this the function can be differentiated and the roots of the differential function are found as follows.

$$e'(\text{CFL}) = 48\epsilon_d\text{CFL}^2 - 48\epsilon_d\text{CFL} + (2 + 8\epsilon_d) \tag{2.26}$$

$$\text{with roots } \text{CFL}^{1,2} = \frac{1}{2}\left(1 \pm \sqrt{\frac{2\epsilon_d - 1}{6\epsilon_d}}\right) \tag{2.27}$$

Due to the symmetry of the polynomial with respect to the inflection point, three possible cases can be found where $e(\text{CFL})$ lies between -1 and 1, as shown in Figure 2.4.

1. $e(\text{CFL})$ is monotonic in the whole domain i.e., $\text{CFL}^{1,2} \in \mathbb{R}^+$
2. $e(\text{CFL})$ is monotonic when $0 \leq \text{CFL} \leq 1$
3. $e(\text{CFL})$ is not monotonic when $0 \leq \text{CFL} \leq 1$ but its extremum values are between -1 and 1 i.e., $-1 \leq e(\text{CFL}) \leq 1$

As shown, the valid ranges for ϵ_d in the function $e(\text{CFL})$ to be monotone in the interval $0 \leq \text{CFL} \leq 1$ could be $[-0.5, 0) \cup [0, 0.5]$. This condition ensures that the dispersion improved CABARET scheme is non-dissipative as $|g| = 1$. Hence,

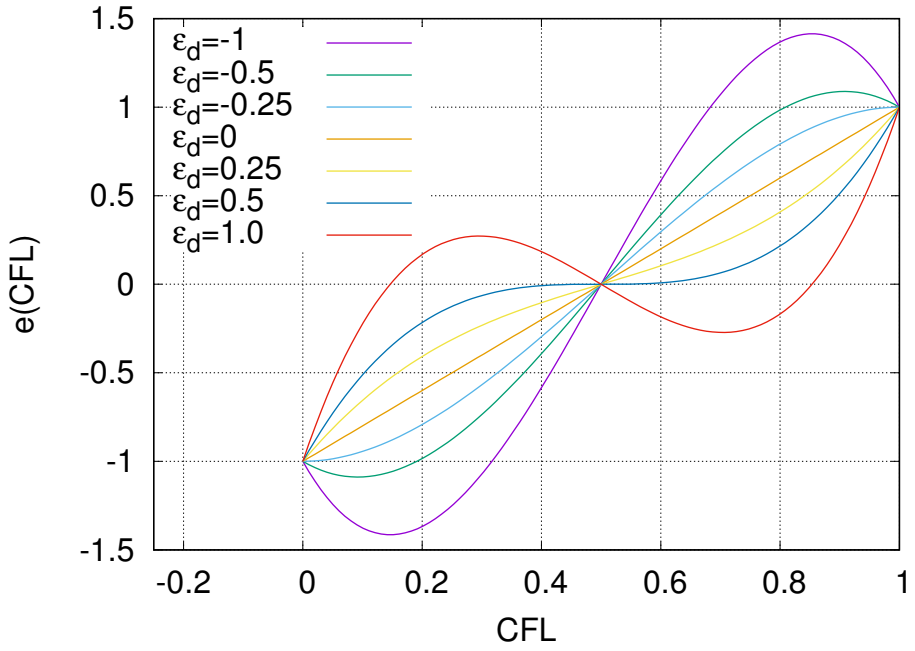

Figure 2.4: Plot showing the variation of e(CFL) for different ϵ_d

the only source of error in g will be dispersion error i.e., the difference between the ideal travelled distance $kc\Delta t$ and the distance propagated by the scheme, given in equation (2.21) . The error in the phase can be computed as

$$e_{phase} = arg\left(e^{ick\Delta t}\right) - arg\left(e^{i(\frac{k\Delta x}{2}+\theta)}\right) = k\Delta x(\text{CFL} - \frac{1}{2}) - \theta \tag{2.28}$$

From the definition of θ the above equation becomes

$$e_{phase} = k\Delta x(\text{CFL} - \frac{1}{2}) - arcsin\left[-(1-2\text{CFL})\text{p} + 8\epsilon_d \text{CFL}(1-\text{CFL})(1-2\text{CFL})\text{p}^3\right] \tag{2.29}$$

where $\text{p} = sin\frac{k\Delta x}{2}$. Also, a relative dispersion error can be computed by normalising the phase error (e_{phase}) with $ck\Delta t$ resulting in

$$e_{dispersion} = 1 - \frac{1}{2\text{CFL}} - \frac{\theta}{k\Delta x \text{CFL}} \tag{2.30}$$

The optimum value of ϵ_d, at which the overall absolute value of phase error

is minimum over the allowable range of CFL and $k\Delta x$ can be found by

$$\frac{d}{d\epsilon_d}\int_0^1\int_0^{\frac{2\pi}{ppw}}|e_{phase}|d(k\Delta x)d(\text{CFL}) = 0 \tag{2.31}$$

where ppw stands for the number of points per wavelength of the numerical wave resolution, the surface e_{phase} passes through three parallel lines CFL = $0, \frac{1}{2}, 1$, and is also symmetric about CFL = $\frac{1}{2}$, hence, one can minimize the enclosed volume by making its tangent plane horizontal along this line.

$$\frac{d|e_{phase}|}{d\epsilon_d}\bigg|_{\text{CFL}=0.5} = 0 \tag{2.32}$$

which simplifies to

$$k\Delta x - 2sin\frac{k\Delta x}{2} + 4\epsilon_d sin^3\frac{k\Delta x}{2} = 0 \tag{2.33}$$

and finally we get an expression for ϵ_d as

$$\epsilon_d = \frac{2sin\frac{k\Delta x}{2} - k\Delta x}{4sin^3\frac{k\Delta x}{2}} \tag{2.34}$$

The optimum distribution of the anti-dispersion coefficient for varying $0 \leq k\Delta x \leq \pi$ and a range of $5 \leq ppw \leq 30$ is shown in Figures 2.5 and 2.6. The plots show approximately that the value of optimal ϵ_d reaches -0.083 for the limiting case of ppw and grid spacing.

The phase error distribution with respect to CFL and $k\Delta x$ are shown in Figures 2.7 to 2.11 for four different values of ϵ_d directs to an optimal value of $-\frac{1}{12}$ as ppw tends to infinity. This value is close to the suggested value of -0.08 by Goloviznin and Samarskii (1998a). In Figure 2.7, the variation of the phase error e_{phase} is plotted for ppw = 10, for varying CFL and ϵ_d, this shows that even for 10 ppw the dispersion error was reduced by four times compared to standard CABARET, as also shown in the zoomed in Figure 2.8. Also, figures 2.9,

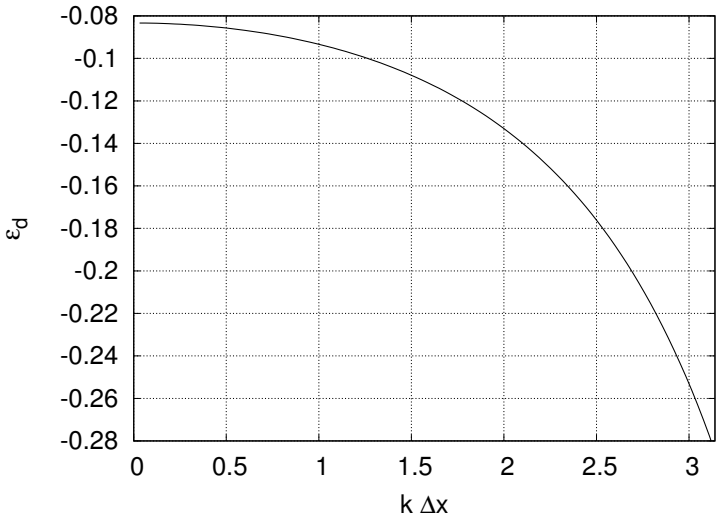

Figure 2.5: Plot showing the distribution of ϵ_d for varying $k\Delta x$

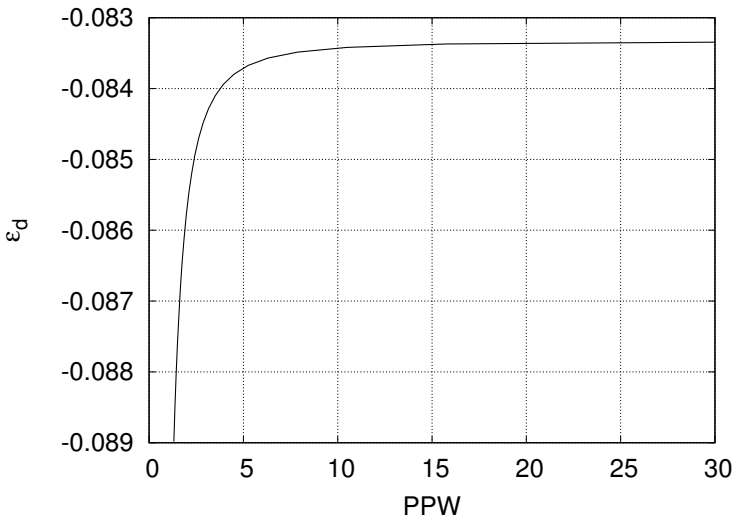

Figure 2.6: Plot showing the distribution of ϵ_d for varying ppw

2.10, and 2.11 show the behaviour of the phase error for CFL = $0.1, 0.3, 0.8$ respectively, and varying $k\Delta x$. This shows that for a range of CFL values the dispersion error is contained.

Furthermore, the dissipation error and the phase error for the CABARET scheme and the dispersion improved CABARET scheme at the optimal coefficient of dispersion, are shown. Also, Figures 2.12, 2.13 show the surfaces of the phase error of the CABARET scheme and the dispersion improved CABARET scheme respectively. The significant reduction in the phase error over the full range of CFL numbers and grid spacings can be observed. The abnormal two

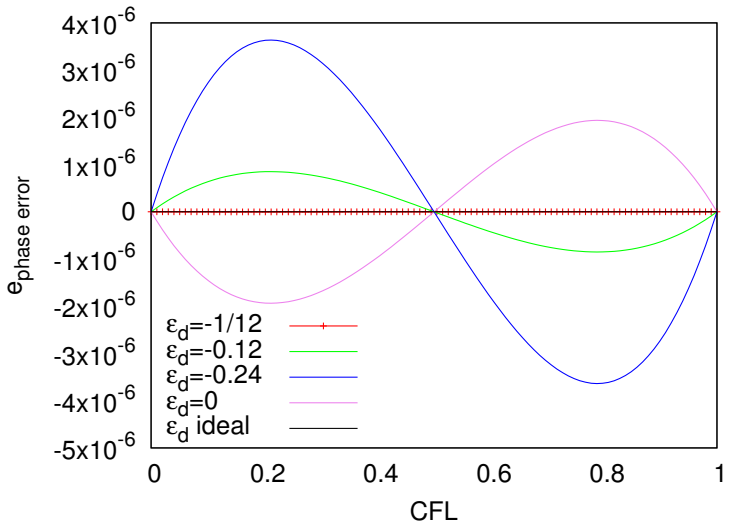

Figure 2.7: Plot showing the phase error (e_{phase}) distribution for ppw = 10 and varying ϵ_d and CFL

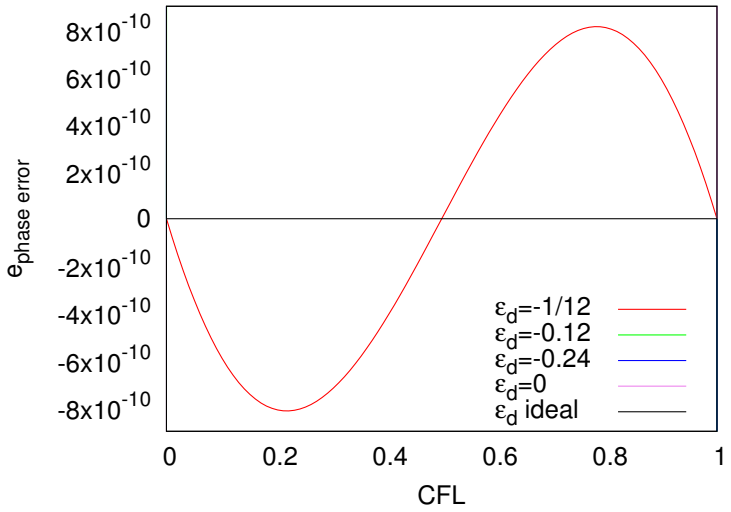

Figure 2.8: Plot showing the zoomed-in phase error (e_{phase}) distribution for ppw = 10 and varying ϵ_d and CFL

peaks of dispersion, which correspond to high wave and small CFL numbers (Karabasov and Goloviznin, 2009) for the CABARET scheme have also been significantly reduced with the dispersion improvement as shown in the surface plot of the phase error in Figure 2.13. The following section describes the non-linear CABARET schemes used in the present work to make the schemes monotone and effective in handling discontinuities.

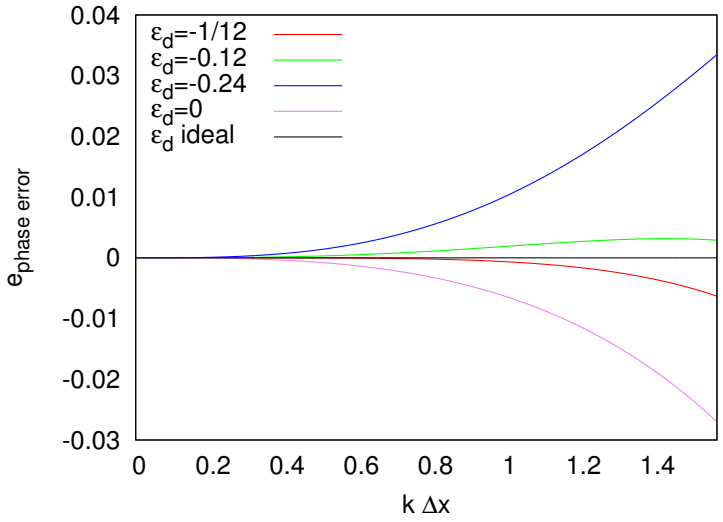

Figure 2.9: Plot showing the phase error (e_{phase}) distribution for CFL = 0.1 and varying ϵ_d and $k\Delta x$

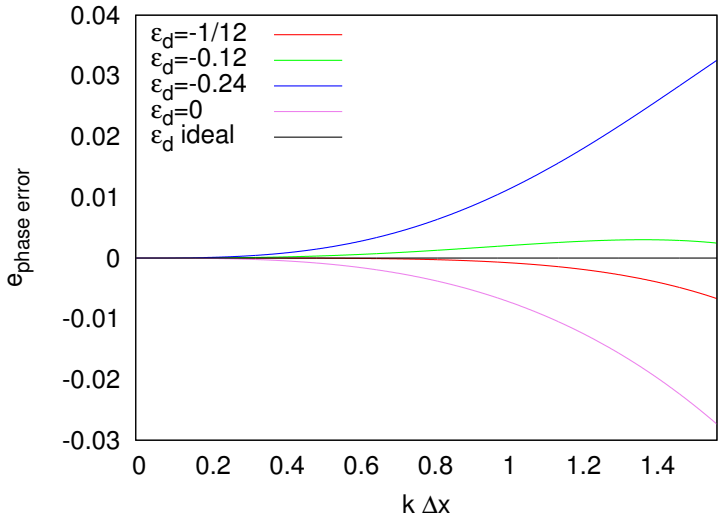

Figure 2.10: Plot showing the phase error (e_{phase}) distribution for CFL = 0.3 and varying ϵ_d and $k\Delta x$

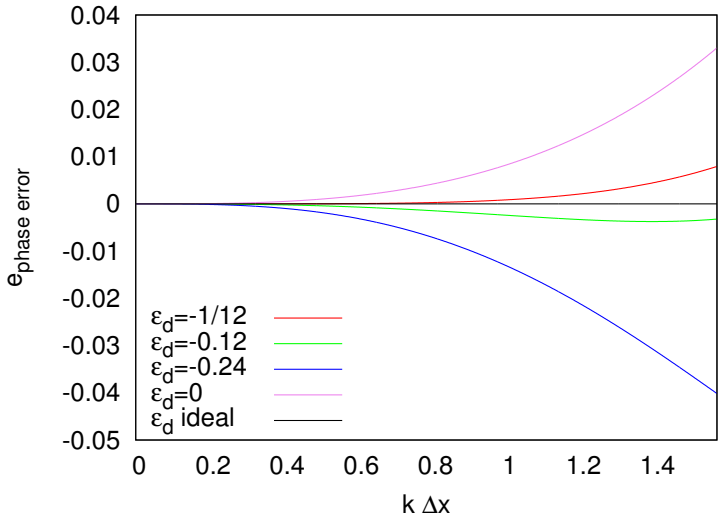

Figure 2.11: Plot showing the phase error (e_{phase}) distribution for CFL = 0.8 and varying ϵ_d and $k\Delta x$

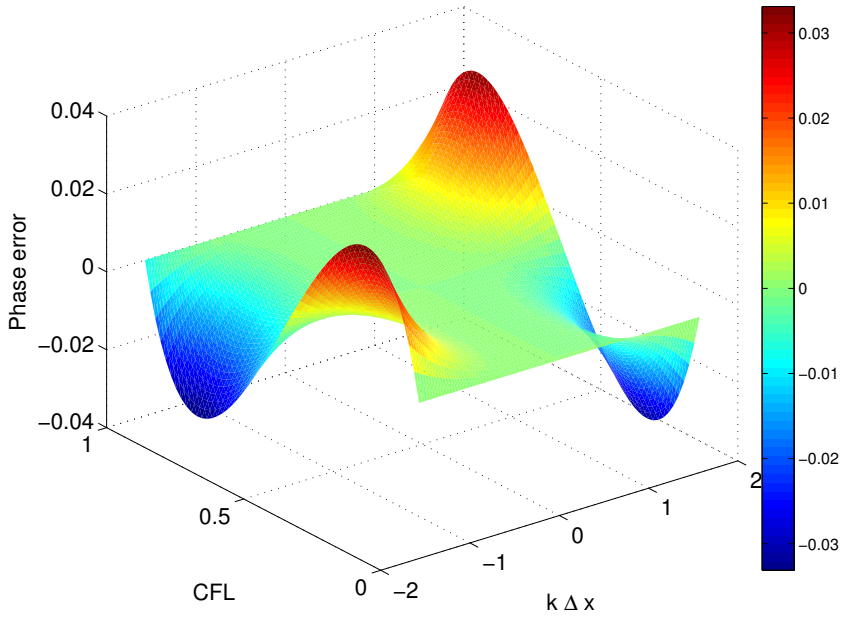

Figure 2.12: Surface plot of the phase error for the CABARET scheme

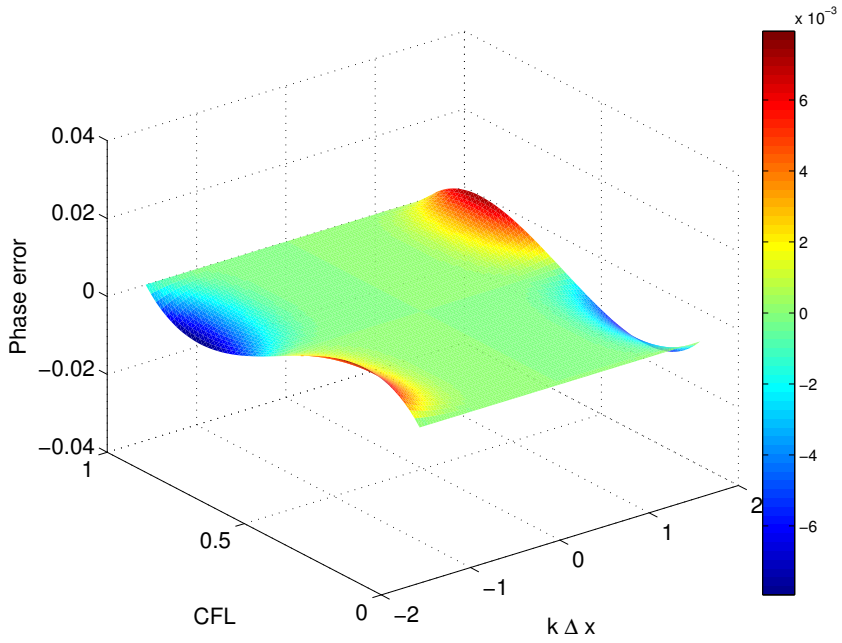

Figure 2.13: Surface plot of the phase error for the Dispersion improved CABARET scheme for the optimal $\epsilon_d = \frac{-1}{12}$

2.2 Order of accuracy

Analysis of the order of accuracy of the dispersion improved CABARET scheme is presented in this section, which has been proposed by Danilin (2013). The baseline CABARET scheme without the non-linear correction is formally second order accurate for all range of CFL numbers ($0 \leq \text{CFL} \leq 1$). As demonstrated by Karabasov and Goloviznin (2009) the standard CABARET scheme, is found to be second-order accurate.

The order of accuracy for the dispersion improved CABARET variant is evaluated using the standard Taylor series expansion in both space and time. We start with the three-level CABARET form from equation (2.5) and obtain the truncated terms to be identical to the anti-dispersion terms. Assuming constant wave speed (c), we have

$$\frac{u_{j+1}^{n+1} - u_{j+1}^{n}}{2\Delta t^{n}} + \frac{u_{j}^{n} - u_{j}^{n-1}}{2\Delta t^{n}} + c\frac{u_{j+1}^{n} - u_{j}^{n}}{\Delta x_{j}} = 0 \tag{2.35}$$

By summing up the predictor (2.11) and the corrector (2.12) step, expressing the cell centre variables through the flux variables using (2.4), and re-arranging the following three-time-level finite difference scheme is obtained:

$$\frac{u_{j+\frac{1}{2}}^{n+1} - u_{j+\frac{1}{2}}^{n}}{2\Delta t} + \frac{u_{j-\frac{1}{2}}^{n} - u_{j-\frac{1}{2}}^{n-1}}{2\Delta t} + c\frac{u_{j+\frac{1}{2}}^{n} - u_{j-\frac{1}{2}}^{n}}{\Delta x} = \mu\left(\frac{\partial^3 u}{\partial x^3}\right) + O(\Delta x^4). \tag{2.36}$$

the second term on the right-hand-side is based on the fact that the central differences of the anti-dispersion term approximate the corresponding derivatives with the error of $O(\Delta x^2)$ and μ itself is $O(\Delta x^2)$.

The Taylor series expansion for function say, $\phi(x, y)$ about the points (x_0, y_0) is given by

$$\phi(x-x_0, y-y_0) = \sum_0^{\infty} \left[\frac{1}{n!} \sum_{k=0}^{n} \binom{n}{k} \frac{\partial^n \phi}{\partial x^{n-k} \partial y^k}\bigg|_{x_0,y_0} (x-x_0)^{n-k}(y-y_0)^k \right] \tag{2.37}$$

$$\binom{n}{k} = \frac{n!}{(n-k)!k!} \tag{2.38}$$

Using the Taylor series expansion and dropping the subscripts of all derivatives that are defined at the cell-centre point j and time level n for readability, each term in the equation (2.5) is expanded around the point j and at the time-step n: (please note that the subscripts for Δx and the derivatives in the Taylor series have been dropped for readability)

$$\begin{aligned}
u_{j+\frac{1}{2}}^{n+1} =& u_j^n + \left[\frac{\Delta x}{2}\frac{\partial u}{\partial x} + \Delta t \frac{\partial u}{\partial t} \right] \\
&+ \frac{1}{2!}\left[\frac{\Delta x^2}{2!}\frac{\partial^2 u}{\partial x^2} + \Delta t \Delta x \frac{\partial^2 u}{\partial t \partial x} + \Delta t^2 \frac{\partial^2 u}{\partial t^2} \right] \\
&+ \frac{1}{3!}\left[\frac{\Delta x^3}{8}\frac{\partial^3 u}{\partial x^3} + \frac{3\Delta t \Delta x^2}{4}\frac{\partial^3 u}{\partial x^2 \partial t} + \frac{3\Delta x \Delta t^2}{2}\frac{\partial^3 u}{\partial t^2 \partial x} + \Delta t^3 \frac{\partial^3 u}{\partial t^3} \right] \\
&+ \frac{1}{4!}\left[\frac{\Delta x^4}{16}\frac{\partial^4 u}{\partial x^4} + \frac{\Delta t \Delta x^3}{2}\frac{\partial^4 u}{\partial x^3 \partial t} + \frac{3\Delta t^2 \Delta x^2}{2}\frac{\partial^4 u}{\partial x^2 \partial t^2} + 2\Delta t^3 \Delta x \frac{\partial^4 u}{\partial x \partial t^3} + \Delta t^4 \frac{\partial^4 u}{\partial t^4} \right] \\
&+ O(\Delta x^5),
\end{aligned}$$

$$\begin{aligned}
u_{j-\frac{1}{2}}^{n-1} =& u_j^n + \left[-\frac{\Delta x}{2}\frac{\partial u}{\partial x} - \Delta t \frac{\partial u}{\partial t} \right] \\
&+ \frac{1}{2!}\left[\frac{\Delta x^2}{2!}\frac{\partial^2 u}{\partial x^2} + \Delta t \Delta x \frac{\partial^2 u}{\partial t \partial x} + \Delta t^2 \frac{\partial^2 u}{\partial t^2} \right] \\
&+ \frac{1}{3!}\left[-\frac{\Delta x^3}{8}\frac{\partial^3 u}{\partial x^3} - \frac{3\Delta t \Delta x^2}{4}\frac{\partial^3 u}{\partial x^2 \partial t} - \frac{3\Delta x \Delta t^2}{2}\frac{\partial^3 u}{\partial t^2 \partial x} - \Delta t^3 \frac{\partial^3 u}{\partial t^3} \right] \\
&+ \frac{1}{4!}\left[\frac{\Delta x^4}{16}\frac{\partial^4 u}{\partial x^4} + \frac{\Delta t \Delta x^3}{2}\frac{\partial^4 u}{\partial x^3 \partial t} + \frac{3\Delta t^2 \Delta x^2}{2}\frac{\partial^4 u}{\partial x^2 \partial t^2} + 2\Delta t^3 \Delta x \frac{\partial^4 u}{\partial x \partial t^3} + \Delta t^4 \frac{\partial^4 u}{\partial t^4} \right] \\
&+ O(\Delta x^5)
\end{aligned}$$

$$
\begin{aligned}
u^n_{j+\frac{1}{2}} &= u^n_j + \left[\frac{\Delta x}{2}\frac{\partial u}{\partial x} + \frac{1}{2!}\frac{\Delta x^2}{4}\frac{\partial^2 u}{\partial x^2} + \frac{1}{3!}\frac{\Delta x^3}{8}\frac{\partial^3 u}{\partial x^3} + \frac{1}{4!}\frac{\Delta x^4}{16}\frac{\partial^4 u}{\partial x^4}\right] + O(\Delta x^5), \\
u^n_{j-\frac{1}{2}} &= u^n_j + \left[-\frac{\Delta x}{2}\frac{\partial u}{\partial x} + \frac{1}{2!}\frac{\Delta x^2}{4}\frac{\partial^2 u}{\partial x^2} - \frac{1}{3!}\frac{\Delta x^3}{8}\frac{\partial^3 u}{\partial x^3} + \frac{1}{4!}\frac{\Delta x^4}{16}\frac{\partial^4 u}{\partial x^4}\right] + O(\Delta x^5),
\end{aligned}
\tag{2.39}
$$

Here, it was assumed that $\Delta x \approx \Delta t$ in accordance with the advection CFL stability condition. On substitution of the terms given by equations (2.39) to (2.39) in the equation (2.5), the following equation is obtained

$$
\frac{\partial u}{\partial t} + c\frac{\partial u}{\partial x} + \left[\frac{c\Delta x^2}{24}\frac{\partial^3 u}{\partial x^3} + \frac{\Delta x^2}{8}\frac{\partial^3 u}{\partial x^2 \partial t} + \frac{\Delta t \Delta x}{4}\frac{\partial^3 u}{\partial x \partial t^2} + \frac{\Delta t^2}{6}\frac{\partial^3 u}{\partial t^3}\right] = \mu\left(\frac{\partial^3 u}{\partial x^3}\right) + O(\Delta x^4),
\tag{2.40}
$$

This equation (2.40) can be further simplified by expressing all time variables in terms of spatial derivatives using the governing linear advection equation

$$
\begin{aligned}
&\frac{\partial u}{\partial t} + c\frac{\partial u}{\partial x} = 0, \quad \frac{\partial u}{\partial t} = -c\frac{\partial u}{\partial x}, \\
&\frac{\partial^3 u}{\partial t \partial x^2} = \frac{\partial}{\partial x^2}\frac{\partial u}{\partial t} = \frac{\partial}{\partial x^2}\left(-c\frac{\partial u}{\partial x}\right) = -c\frac{\partial^3 u}{\partial x^3}, \\
&\frac{\partial^3 u}{\partial x \partial t^2} = \frac{\partial}{\partial x}\frac{\partial}{\partial t}\frac{\partial u}{\partial t} = \frac{\partial}{\partial x}\frac{\partial}{\partial t}\left(-c\frac{\partial u}{\partial x}\right) = -c\frac{\partial^2}{\partial x^2}\frac{\partial u}{\partial t} = c^2\frac{\partial^3 u}{\partial x^3}, \\
&\frac{\partial^3 u}{\partial t^3} = \frac{\partial}{\partial t^2}\left(-c\frac{\partial u}{\partial x}\right) = -c^3\frac{\partial^3 u}{\partial x^3},
\end{aligned}
\tag{2.41}
$$

to obtain

$$
\frac{\partial u}{\partial t} + c\frac{\partial u}{\partial x} - \frac{c}{12}(\Delta x - c\Delta t)(\Delta x - 2c\Delta t)\frac{\partial^3 u}{\partial x^3} = \mu\left(\frac{\partial^3 u}{\partial x^3}\right) + O(\Delta x^4),
\tag{2.42}
$$

which is identical to

$$
\frac{\partial u}{\partial t} + \frac{\partial f}{\partial x} = O(\Delta x^4)
\tag{2.43}
$$

since, $\mu = \frac{-1}{12}\Delta x^2(1 - \text{CFL})(1 - 2\text{CFL})$ in accordance with equation (2.10).

The above shows that the dispersion improved CABARET scheme (2.11)-(2.4) is fourth-order accurate in space and time for linear wave propagation for the suggested value of the anti-dispersion parameter.

To demonstrate the fourth order of accuracy for linear wave propagation, the dispersion improved CABARET scheme has been applied to the linear advection equation to propagate a wave profile modulated by a Gaussian profile (Bogey and Bailly, 2004; Karabasov and Goloviznin, 2009).

The corresponding initial-boundary-value problem is described by equation (2.1) where $\frac{\partial f}{\partial u} = 1$ and the initial condition and the computational domain size are defined by equation (2.44)

$$u(x, t = 0) = sin\left(\frac{2\pi x}{8}\right) exp\left(-\ln(2)\left(\frac{x}{3}\right)^2\right), -200 < x < 200. \tag{2.44}$$

Having periodic boundary conditions, the initial profile is advected for 16.67 dimensionless time units ($\frac{l}{\frac{\partial f}{\partial u}}$), where $l = 6$ is the characteristic width of the Gaussian distribution on a sequence of uniformly spaced grids.

Figure 2.14 shows comparison of the dispersion improved CABARET solution with that of the standard CABARET at a typical control time, 12.5 dimensionless time units on the grid resolution which corresponds to 4 cells per the characteristic Gaussian width (l). No flux correction is applied in either of the linear advection calculations and the CFL number is equal to 0.2. The analytical solution obtained at the same control time, which almost coincides with the dispersion-improved CABARET solution, is included on the same plot.

Tables 2.1 and 2.2 present the corresponding error convergence as the grid is systematically refined for each of the several CFL numbers considered. The error is defined in the standard L1-norm. While the standard CABARET shows the second-order rate of grid convergence in accordance with Karabasov and Goloviznin (2009), the dispersion improved CABARET solution confirms the

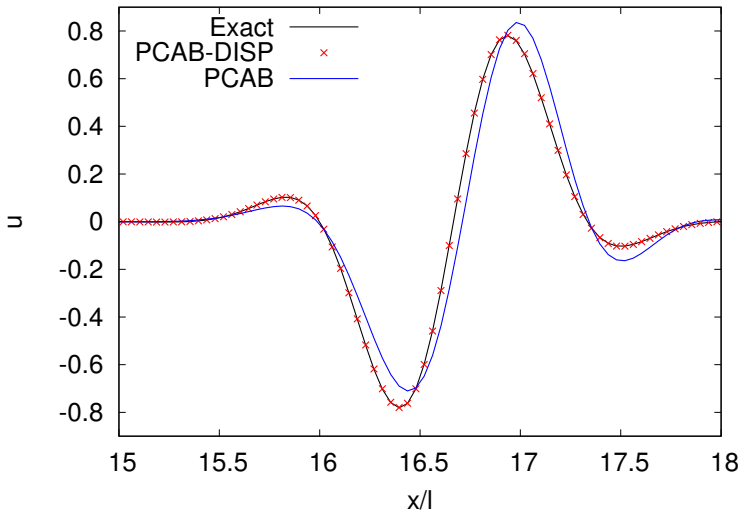

Figure 2.14: Advection of a Gaussian modulated wave profile: comparison of the dispersion improved CABARET solution (PCAB-DISP), the standard CABARET (PCAB), and the analytical solution for grid size of 1600 cells and CFL=0.2.

fourth-order of accuracy in accordance with the analysis of Section 2.2.

Grid points	L1 error CFL=0.2	OOA	L1 error CFL=0.4	OOA	L1 error CFL=0.6	OOA	L1 error CFL=0.8	OOA
6400	1.58e-04	2.00	3.94e-05	2.00	2.63e-05	2.00	3.94e-05	2.00
3200	6.31e-04	1.99	1.58e-04	2.00	1.05e-04	2.00	1.58e-04	2.00
1600	2.51e-03	1.92	6.31e-04	2.00	4.20e-04	1.99	6.33e-04	2.01
800	9.48e-03	1.38	2.52e-03	1.91	1.67e-03	1.96	2.55e-03	1.96
400	2.47e-02	0.91	9.48e-03	1.21	6.50e-03	1.47	9.94e-03	1.46
200	4.64e-02	-	2.20e-02	-	1.81e-02	-	2.73e-02	-

Table 2.1: Order of accuracy for P-CAB scheme for CASE J at CFL=0.2, 0.4, 0.6 and 0.8, respectively

Grid points	L1 error CFL=0.2	OOA	L1 error CFL=0.4	OOA	L1 error CFL=0.6	OOA	L1 error CFL=0.8	OOA
6400	1.08e-07	4.00	2.85e-08	4.00	8.41e-09	4.24	2.74e-08	4.00
3200	1.72e-06	3.99	4.55e-07	3.99	1.59e-07	4.65	4.38e-07	3.99
1600	2.74e-05	4.00	7.23e-06	3.98	4.00e-06	4.03	6.98e-06	4.00
800	4.38e-04	3.99	1.14e-04	3.88	6.51e-05	4.05	1.12e-04	3.97
400	6.94e-03	2.44	1.69e-03	3.19	1.08e-03	3.30	1.75e-03	3.45
200	3.78e-02	-	1.54e-02	-	1.06e-02	-	1.91e-02	-

Table 2.2: Order of accuracy for P-CAB scheme wih dispersion improvement for CASE J at CFL=0.2, 0.4, 0.6 and 0.8, respectively

2.3 Non-Linear CABARET schemes

The original CABARET scheme is second-order accurate in equations (2.11) to (2.4) (this is referred as P-CAB in short). Hence, according to the Godunov theorem, new extrema in the solution is allowed in the form of non-physical oscillations. To avoid this, a non-linear correction procedure based on the maximum principle (Karabasov and Goloviznin, 2009) is applied, to truncate the flux value computed at the extrapolation step (2.4). This correction (referred to as F-CAB) is applied at the extrapolation step for two possible cases of the sign as per the wave speed as

$$
\begin{aligned}
Case \quad \frac{df}{du} > 0: & \\
m^{+} &= min(u^{n}_{j-\frac{1}{2}}, u^{n}_{j}, u^{n}_{j+\frac{1}{2}}) \\
M^{+} &= max(u^{n}_{j-\frac{1}{2}}, u^{n}_{j}, u^{n}_{j+\frac{1}{2}}) \\
(u^{n+1}_{j+\frac{1}{2}})^{+} &= median(m^{+}, 2u^{n}_{j} - u^{n}_{j-\frac{1}{2}}, M^{+})
\end{aligned}
\tag{2.45}
$$

$$
\begin{aligned}
Case \quad \frac{df}{du} < 0: & \\
m^{-} &= min(u^{n}_{j+\frac{1}{2}}, u^{n}_{j+1}, u^{n}_{j+\frac{3}{2}}) \\
M^{-} &= max(u^{n}_{j+\frac{1}{2}}, u^{n}_{j+1}, u^{n}_{j+\frac{3}{2}}) \\
(u^{n+1}_{j+\frac{1}{2}})^{-} &= median(m^{-}, 2u^{n}_{j+1} - u^{n}_{j+\frac{3}{2}}, M^{-})
\end{aligned}
\tag{2.46}
$$

The plus (+) and minus (−) waves correspond to the positive and negative wave speeds, respectively. However, in general, the interface fluxes are obtained between these two states. The face values are reconstructed from the min and max values of the flux function which correspond to the solution variables ϕ_{min} and ϕ_{max}, respectively. The procedure depends on the sign of the conservative variable variation at mid-time-step as

$$u_{j+\frac{1}{2}}^{n+1} = \begin{cases} \phi_{max} & \text{if } u_j - u_{j-1} < 0, \\ \phi_{min} & \text{if } u_j - u_{j-1} \geq 0 \end{cases} \tag{2.47}$$

The above algorithm is robust for non-linear wave problems but leads to artificial dissipation when computing linear wave propagation at high frequencies, when the discrete maximum principle based on three solution points per computational cell is not very accurate. Furthermore, for small CFL numbers away from the optimum range for CABARET, this dissipation becomes even larger, since, in this case, the flux correction is most active to smear out effects of the growing numerical dispersion error.

The second flux-correction method (referred to as R-CAB) suggested in Karabasov and Goloviznin (2009) for high-frequency wave propagation corresponds to artificially extending the maximum (M) and minimum limits (m) as

$$\begin{aligned} m \rightarrow m &\equiv m(1 - \epsilon_{rx} sign(m)) \\ M \rightarrow M &\equiv M(1 + \epsilon_{rx} sign(M)) \end{aligned} \tag{2.48}$$

here $\epsilon_{rx} \geq 0$ is a small tunable parameter, the limiting cases of which correspond to the baseline flux correction or the linear CABARET scheme. It was later found out that the optimal value of this tunable parameter is very case dependent and is presented in chapter 4. Hence, instead of (2.48), a modified relaxed flux correction algorithm (referred to as MR-CAB) for CABARET based on the following modification of the maximum (M) and minimum limits (m) is presented as

$$
\begin{aligned}
m \longrightarrow m &\equiv m - \epsilon_{mrx}\delta_{rx} \\
M \longrightarrow M &\equiv M + \epsilon_{mrx}\delta_{rx} \\
\delta_{rx} &= \frac{1}{2}(M - m)
\end{aligned}
\tag{2.49}
$$

Again, the parameter $\epsilon_{mrx} \geq 0$ is a tunable parameter. This modification corresponds to a linear stretching of the solution variation as allowed by the discrete maximum principle with a constant factor so that $M - m \longrightarrow (1 + \epsilon_{mrx})(M - m)$. Compared to R-CAB algorithm in equation (2.48), the values of this parameter in equation (2.49) lying within the range of $0.2 \leq \epsilon_{mrx} \leq 0.4$ lead to acceptable results for both linear advection and gas dynamics problems as will be demonstrated in chapter 4.

For strongly non-linear problems, where even a small amount of numerical oscillations is unwanted, a further refined modified relaxed correction algorithm is proposed. This reduces to the baseline correction scheme (F-CAB, as shown in equations (2.45) and (2.46)) in the non-linear region of large wave amplitudes (e.g. shocks), while using the relaxation of the maximum and minimum limits in accordance with the equation (2.49) (MRCAB), when the wave amplitudes are small corresponding to a linear solution regime (e.g. acoustic wave propagation). The detection of the linear and the non-linear wave propagation regimes can be performed automatically by using the following limiter function (referred with a suffix LIM)

$$m \rightarrow m \equiv m - \epsilon_{mrx}\phi(\delta_{rx})\bar{m} \tag{2.50}$$

$$M \rightarrow M \equiv M + \epsilon_{mrx}\phi(\delta_{rx})\bar{m} \tag{2.51}$$

$$\bar{m} = 0.5(m+M) \tag{2.52}$$

$$\phi(\delta_{rx}) = \begin{cases} \frac{\delta_{rx}}{\bar{m}} & if \left|\frac{\delta_{rx}}{\bar{m}}\right| \ll 1 \\ 0 & else \end{cases} \tag{2.53}$$

Here, for practical purposes the threshold values of $|\frac{\delta}{\bar{m}}| < 0.001 - 0.01$ may be used.

To summarize, different non-linear correction procedures have been presented to handle the different flow scenarios. Also, the dispersion term correction also needs to be switched off in the regions of discontinuities, and the following section describes the limiter function developed for this purpose.

2.3.1 Dispersion term correction

In comparison to the standard CABARET scheme, the dispersion improved CABARET includes the third derivative as shown in equation (2.7), which is used to counteract the numerical dispersion for linear propagation. However, across a discontinuity such as a shock, the high-order derivative term becomes ill-posed (as the first-order differential is undefined), hence, defeats the original purpose of using the anti-dispersion term for improving the propagation properties of the CABARET algorithm. Therefore, for non-linear flow regimes a slope-detector can be defined as

$$\left|\frac{(f^n_{n+1} - f^n_j)}{\bar{f}^n_{j+\frac{1}{2}}}\right| \approx O(1) \qquad \bar{f}^n_{j+\frac{1}{2}} = 0.5(f^n_{j+1} + f^n_j) \tag{2.54}$$

And based on this an automatic procedure is suggested to deactivate the disper-

sion correction smoothly. In implementations, the following detecting condition of the non-linear wave region can be used

$$\left| \frac{(f^n_{n+1} - f^n_j)}{\bar{f}^n_{j+\frac{1}{2}}} \right| > 0.001 - 0.1 \tag{2.55}$$

The limiting of the dispersion term can be achieved by the following modification of the dispersion flux based on the evaluation of the solution slope ratio

$$r_j = \left(\frac{f^n_{j+1} - f^n_j}{\Delta x_{j+\frac{1}{2}}} \right) \left(\frac{f^n_j - f^n_{j-1}}{\Delta x_{j-\frac{1}{2}}} \right)^{-1} \tag{2.56}$$

$$case \quad |r_j| > 1, \quad \delta f^n_j = -\frac{\mu_j}{\Delta \bar{x}_j} \left(\frac{f^n_j - f^n_{j-1}}{\Delta x_{j-\frac{1}{2}}} \right) (\phi(r_j) - 1) \tag{2.57}$$

$$case \quad |r_j| \leq 1, \quad \delta f^n_j = -\frac{\mu_j}{\Delta \bar{x}_j} \left(\frac{f^n_j - f^n_{j-1}}{\Delta x_{j-\frac{1}{2}}} \right) \left(1 - \phi \left(\frac{1}{r_j} \right) \right) \tag{2.58}$$

$$\phi(x) = \begin{cases} x & |x| \leq \alpha \\ 1 & else \end{cases} \tag{2.59}$$

Threshold values in the region of $1 \leq \alpha \leq 2$ (note that $\alpha = 1$ reduces the dispersion-improved scheme to the standard CABARET) lead to quite acceptable results for the problems considered in the present work.

2.4 Boundary condition treatment

The boundary conditions are not altered in the dispersion correction scheme. The standard CABARET scheme should be used at all boundaries except the periodic boundary condition. At the periodic boundaries, the dispersion improvement is applied just as in the case of internal faces.

2.5 Euler equations

The extension of the dispersion-improved CABARET to the system of hyperbolic equations in one-dimension is presented in this section. The compressible Euler equations in conservation form are given by

$$\frac{\partial \mathrm{Q}}{\partial t} + \frac{\partial \mathrm{F}}{\partial x} = 0 \tag{2.60}$$

$$\mathrm{Q} = \begin{bmatrix} \rho \\ \rho u \\ \rho E \end{bmatrix}, \mathrm{F} = \begin{bmatrix} \rho u \\ \rho u^2 + p \\ (\rho E + p)u \end{bmatrix} \tag{2.61}$$

where Q is the vector of conservative variables, and F is the flux vector in the x-direction, respectively. Also, ρ is the density, p is the pressure, and $E = \frac{1}{\gamma - 1}\frac{p}{\rho} + \frac{|\vec{q}|^2}{2}$ is the total specific energy, $\vec{q} = [u]$ is the velocity vector, and, γ is the ratio of the specific heats at constant pressure and volume for the given fluid. Hence, the CABARET scheme can be written as in the predictor-corrector form. For the cell (j) with faces $j + \frac{1}{2}$ and $j - \frac{1}{2}$ and time-step $\Delta t^{n+\frac{1}{2}}$

$$\frac{\mathrm{Q}_j^{n+\frac{1}{2}} - \mathrm{Q}_j^n}{0.5\Delta t^{n+\frac{1}{2}}} + \frac{\mathrm{F}^n_{j+\frac{1}{2}} - \mathrm{F}^n_{j-\frac{1}{2}}}{h_x} = 0 \tag{2.62}$$

$$\frac{\mathrm{Q}_j^{n+1} - \mathrm{Q}_j^{n+\frac{1}{2}}}{0.5\Delta t^{n+\frac{1}{2}}} + \frac{\mathrm{F}^{n+1}_{j+\frac{1}{2}} - \mathrm{F}^{n+1}_{j-\frac{1}{2}}}{h_x} = 0 \tag{2.63}$$

here, h_x is the length of the cell in the x-direction. For this system of Euler equations (with say m variables) given by equation (2.60), the extrapolation step requires that the solution be decomposed into characteristic fields. The Euler equations can be cast into the characteristic form using a choice of left Eigen-matrix ($\mathrm{L}_{j=x,y,z}$, in three dimensions) which diagonalises (i.e.,$\mathrm{L}_j A \mathrm{L}_j = \Lambda_x = diag[\lambda_{1x}, ...\lambda_{mx}]$) the flux Jacobians in each direction i.e., $\mathrm{A} = \frac{d\mathrm{F}}{d\mathrm{U}}$. Let V be the

vector of primitive variables, given by $\mathrm{V} = (\rho, u, p)^T$, then the characteristic form can be written as

$$\frac{\mathrm{L_x}.\partial \mathrm{V}}{\partial t} + \Lambda_x \frac{\mathrm{L_x}.\partial \mathrm{V}}{\partial x} = \mathrm{g_x}, \quad \mathrm{g_x} = -\mathrm{L_x A}\frac{\partial \mathrm{V}}{\partial x} \tag{2.64}$$

Here, the right-hand source term is due to the partial derivatives in the tangential direction. The characteristic form is obtained away from regions away from discontinuities. The characteristic fields i.e., the local Riemann invariants (denoted by $d\mathrm{R} = \mathrm{L}.d\mathrm{V}$) are chosen from several choices of the left Eigen-matrix as presented in Karabasov and Goloviznin (2009) are

$$\mathrm{L_x} = \begin{pmatrix} 0 & 1 & \frac{1}{\sqrt{\gamma}} S^{\frac{1}{2\gamma}} p^{-\frac{\gamma+1}{\gamma}} \\ 0 & 1 & -\frac{1}{\sqrt{\gamma}} S^{\frac{1}{2\gamma}} p^{-\frac{\gamma+1}{\gamma}} \\ -\frac{\gamma}{p} & 0 & \frac{1}{p} \end{pmatrix}, \quad S = p\rho^{-\gamma} \tag{2.65}$$

$$\mathrm{R_x} = \left(u + ap^b, u - ap^b, ln(p\rho^{-\gamma})\right)^T, \quad a = \frac{2\sqrt{\gamma}}{\gamma - 1} S^{\frac{1}{2\gamma}}, \quad b = \frac{\gamma - 1}{2\gamma} \tag{2.66}$$

The primitive variables can then be obtained using the invariants as follows, the subscript indicating the component in the invariant vector

$$u = \frac{1}{2}((\mathrm{R_x})_1 + (\mathrm{R_x})_2) \tag{2.67}$$

$$p = \left(\frac{(\mathrm{R_x})_1 + (\mathrm{R_x})_2}{2a}\right)^{\frac{1}{b}} \tag{2.68}$$

$$\rho = \left(\frac{\exp(\mathrm{R_x})_3}{p}\right)^{\frac{-1}{\gamma}} \tag{2.69}$$

These are obtained for the ideal gas equation of state assuming cell-wise constant entropy (hence the entropy is evaluated at conservative variables), such that the local Riemann invariants become full invariants for isentropic flows. The Riemann invariants are reconstructed at cell centers and faces of cell as

$$\text{At cell center :} \qquad (R_x)_j^n, (R_x)_j^{n+\frac{1}{2}} \tag{2.70}$$

$$\text{At cell faces :} \qquad (R_x)_{j+\frac{1}{2}}^n, (R_x)_{j-\frac{1}{2}}^n \tag{2.71}$$

Now, the extrapolation step using the above invariants can be written in the x-direction as

$$(R_{m^+})_{j+\frac{1}{2}}^{n+1} = 2(R_{m^+})_j^{n+\frac{1}{2}} - (R_{m^+})_{j-\frac{1}{2}}^n \tag{2.72}$$

$$(R_{m^-})_{j-\frac{1}{2}}^{n+1} = 2(R_{m^-})_j^{n+\frac{1}{2}} - (R_{m^-})_{j+\frac{1}{2}}^n \tag{2.73}$$

Following the application of the maximum principle to scalar advection equation presented in section 2.3, the same is applied to the above characteristic form of the Euler equations. However, an additional constraint to the limit of the invariants coming from the right-hand-side term in equation (2.64) is considered. In the x-direction, this is written for time-step (Δt) as

$$(R_x)_{min} < R_x{}^{t=t_0+\Delta t} < (R_x)_{max} \tag{2.74}$$

$$(R_x)_{min/max} = min/max(R_x)_{t=t_0} + \int_{t_0}^{t_0+\Delta t} g_x dt \tag{2.75}$$

The extrapolation procedure is then performed for Riemann quasi-invariants R_{m^+} and R_{m^-} going in the positive and negative direction according to the characteristic wave speeds. The wave speeds are evaluated on cell-face at the mid time-level by attributing the positive wave speed (denoted by $\Lambda_{m^+} > 0$) and negative wave speeds (denoted by $\Lambda_{m^-} < 0$) to the positive and (denoted by R_{m^+}) negative (denoted by R_{m^-}) invariants respectively as

$$\Lambda = \Lambda_{m^+} + \Lambda_{m^-} \tag{2.76}$$

$$(\Lambda_{m^+})^{n+\frac{1}{2}}_{j+\frac{1}{2}} = \frac{1}{2}\left((\Lambda_{m^+})^{n+\frac{1}{2}}_{j} + (\Lambda_{m^+})^{n+\frac{1}{2}}_{j+1}\right) \tag{2.77}$$

$$(\Lambda_{m^-})^{n+\frac{1}{2}}_{j-\frac{1}{2}} = \frac{1}{2}\left((\Lambda_{m^-})^{n+\frac{1}{2}}_{j} + (\Lambda_{m^-})^{n+\frac{1}{2}}_{j-1}\right) \tag{2.78}$$

The non-linear correction is applied after the extrapolation step and the same variants of the CABARET schemes as presented in section 2.3. Additionally the evaluation of the extra source term (g) is needed. In the x-direction, the non-linear correction can be written following equation (2.74) as

$$min/max(\mathrm{R_x}) = min/max\left[(\mathrm{R_x})_{j-\frac{1}{2}}, (\mathrm{R_x})_{j}, (\mathrm{R_x})_{j+\frac{1}{2}}\right] + \Delta t^n (\mathrm{g_x})^{n+\frac{1}{2}}_{j} \tag{2.79}$$

This source term can be computed using the invariants staggered in space in time and for a cell, in the x-direction, this can be written as

$$(\mathrm{g_x})^{n+\frac{1}{2}}_{j} = -\left[\frac{(\mathrm{R_x})^{n+\frac{1}{2}}_{j} - (\mathrm{R_x})^{n}_{j}}{0.5\Delta t^{n+\frac{1}{2}\,n}} + (\Lambda_x)^{n+\frac{1}{2}}_{j} . \frac{(\mathrm{R_x})^{n}_{j+\frac{1}{2}} - (\mathrm{R_x})^{n}_{j-\frac{1}{2}}}{\Delta x_j}\right] \tag{2.80}$$

Finally, the computed two sets of local invariants for each cell face, i.e., $((R_{m^+})^{n+1}_{j+\frac{1}{2}}$ and $(R_{m^-})^{n+1}_{j+\frac{1}{2}})$, then undergo the selection procedure to obtain a single flux vector for internal and boundary faces following the procedure described.

2.5.1 Reconstruction of characteristic flux vector

The selection of appropriate Riemann invariants coming from the left and the right sides to a face (say $j-\frac{1}{2}$, as shown in Figure 2.15) from cells (j and $j-1$) are treated according to the signs of the averaged characteristic speeds i.e., Eigenvalues ($\Lambda^T = (u+c, u-c, u)$, c is the speed of sound) of the cells. Note that the subscript x has been dropped for legibility.

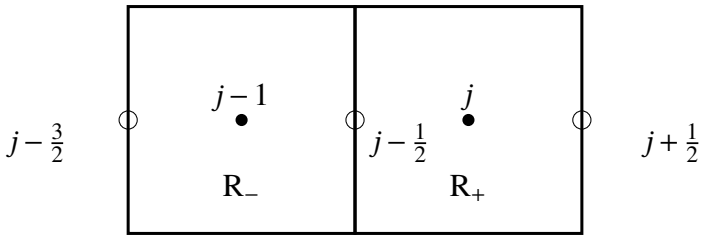

Figure 2.15: Figure showing the internal face $j-\frac{1}{2}$ with the invariants from face sharing cells.

The plus and minus components of the characteristic vector pertain to the waves arriving from cells j and $j-1$, respectively. The signs are defined as

$$sign(u+c) = sign((u+c)_j + (u+c)_{j-1}) \tag{2.81}$$

$$sign(u-c) = sign((u-c)_j + (u-c)_{j-1}) \tag{2.82}$$

$$sign(u) = sign(u_j + u_{j-1}) \tag{2.83}$$

2.5.1.1 Internal faces

The wave speeds are generally subsonic or supersonic, going to the left or right. The choice of the invariants at the cell face $((R_{j-\frac{1}{2}})^T)$ can then be described as follows for these possible flow conditions.

1. Subsonic flow to the right

   $sign(u+c) > 0, sign(u-c) < 0, sign(u) > 0$ corresponds to

   $(R_{j-\frac{1}{2}})^T = ((R_{1^+})_{j-\frac{1}{2}}, (R_{2^-})_{j-\frac{1}{2}}, (R_{3^+})_{j-\frac{1}{2}})$

2. Subsonic flow to the left

   $sign(u+c) > 0, sign(u-c) < 0, sign(u) < 0$ corresponds to

   $(R_{j-\frac{1}{2}})^T = ((R_{1^+})_{j-\frac{1}{2}}, (R_{2^-})_{j-\frac{1}{2}}, (R_{3^-})_{j-\frac{1}{2}})$

3. Supersonic flow to the right

   $sign(u+c) > 0, sign(u-c) > 0, sign(u) > 0$ corresponds to

   $(R_{j-\frac{1}{2}})^T = ((R_{1^+})_{j-\frac{1}{2}}, (R_{2^+})_{j-\frac{1}{2}}, (R_{3^+})_{j-\frac{1}{2}})$

4. Supersonic flow to the left

   $sign(u+c) < 0, sign(u-c) < 0, sign(u) < 0$ corresponds to

   $(\mathrm{R}_{\mathrm{j}-\frac{1}{2}})^T = ((\mathrm{R}_{1^-})_{\mathrm{j}-\frac{1}{2}}, (\mathrm{R}_{2^-})_{\mathrm{j}-\frac{1}{2}}, (\mathrm{R}_{3^-})_{\mathrm{j}-\frac{1}{2}})$

2.5.1.2 Boundary faces

The different types of the standard boundary conditions and their treatment are described below, considering the same face as the boundary face ($f = i - \frac{1}{2}$), and $i-1$ as the external cell, as shown in Figure 2.16.

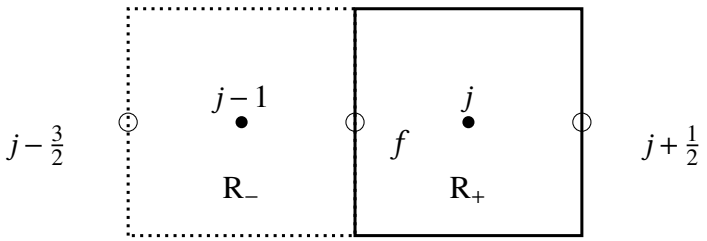

Figure 2.16: Figure showing the boundary face $f = j - \frac{1}{2}$ and external cell $j-1$.

1. Supersonic inflow: All inlet flow conditions are specified at infinity at the boundary face.

   $\rho_f = \rho_\infty, u_f = u_\infty, p_f = p_\infty$

2. Supersonic outflow: All flow conditions at the boundary face are prescribed from the interior cell.

   $(u_f + a_j(p_f)^b, u_f - a_j(p_f)^b, ln(p_f(\rho_f)^{-\gamma})) = ((\mathrm{R}_1)_f, (\mathrm{R}_2)_f, (\mathrm{R}_3)_f)$

3. Subsonic inflow: Two incoming local Riemann invariants are extrapolated from the infinity and one outgoing is calculated from the domain interior.

   $(u_f + a_{j-1}(p_f)^b, u_f - a_j(p_f)^b, ln(p_f(\rho_f)^{\gamma})) = ((\mathrm{R}_1)_{j-1}, (\mathrm{R}_2)_f, (\mathrm{R}_3)_{j-1})$

4. Subsonic outflow: One incoming invariant is extrapolated from the condition at infinity and the remaining local invariants are calculated from the interior.

   $(u_f + a_{j-1}(p_f)^b, u_j - a_j(p_f)^b, ln(p_f(\rho_f)^{\gamma})) = ((\mathrm{R}_1)_\infty, (\mathrm{R}_2)_f, (\mathrm{R}_3)_f)$

5. Inviscid wall: The incoming Riemann variable is obtained from the condition of satisfying zero velocity on the boundary and the entropy is updated according to the velocity sign in cell j.
   $(u_f + a_j(p_f)^b, u^{n+1}_{j+\frac{1}{2}} - a_j(p_f)^b, ln(p_f(\rho_f)^{-\gamma})) = (-(\mathrm{R}_2)_f, (\mathrm{R}_2)_f, (\mathrm{R}_3)_f)$ if $, u_j \leq 0$ and
   $(u_f + a_j(p_f)^b, u^{n+1}_{j+\frac{1}{2}} - a_j(p_f)^b, \rho_f) = (-(\mathrm{R}_2)_f, (\mathrm{R}_2)_f, \rho_j)$, if $u_j > 0$

6. Periodic boundary: The periodic boundary is treated as an internal face replacing the external cell with the mapped cell.

2.5.1.3 Special cases

Special flow scenarios like the centered expansion fan or a standing wave are seen as modifications to the internal face formulations. Some of them are presented as follows.

1. A sonic point $u \pm c = 0$ between the right (j) and the left ($j-1$) cells may be found due to the following possibilities.

   (a) Subsonic flow to the right in the left cell and supersonic flow to the right in the right cell.
   $(u+c)_{j-1} > 0$, $(u-c)_{j-1} < 0$, $u_{j-1} > 0$ and $(u+c)_j > 0$, $(u-c)_j > 0$, $u_j > 0$

   (b) Supersonic flow to the left in the left cell and subsonic flow to the left in the right cell.
   $(u+c)_{j-1} < 0$, $(u-c)_{j-1} < 0$, $u_{j-1} < 0$ and $(u+c)_j > 0$, $(u-c)_j < 0$, $u_j < 0$

   In this case the two characteristics approaching the face are readily evaluated, however, the velocity at the face $(j-\frac{1}{2})$ is missing and this is obtained from the second-order interpolation between the face-sharing cells as

$$u_{j-\frac{1}{2}} = 0.5c_j\left(\frac{u_j}{c_j} + \frac{u_{j-1}}{c_{j-1}}\right).\left(\frac{p_{j-\frac{1}{2}}}{p_j}\right)^b \tag{2.84}$$

2. The other special case is a centered expansion wave, which moves with supersonic speeds. $(u+c)_{j-1} < 0$, $(u-c)_{j-1} < 0$, $u_{j-1} < 0$ and $(u+c)_j > 0$, $(u-c)_j > 0$, $u_j > 0$

   In this case, instead of the standard extrapolation in equation (2.4), a simplified modified algorithm is used to introduce linear dissipation in the cell which contains a singular point. It can be written as

$$(\mathrm{R}_+)^{n+1}_{j+\frac{1}{2}} = \frac{2}{1+\epsilon_{mod}}(\mathrm{R})^{n+\frac{1}{2}}_j - \frac{1-\epsilon_{mod}}{1+\epsilon_{mod}}(\mathrm{R})^n_{j-\frac{1}{2}} \tag{2.85}$$

$$(\mathrm{R}_-)^{n+1}_{j-\frac{1}{2}} = \frac{2}{1+\epsilon_{mod}}(\mathrm{R})^{n+\frac{1}{2}}_j - \frac{1-\epsilon_{mod}}{1+\epsilon_{mod}}(\mathrm{R})^n_{j+\frac{1}{2}} \tag{2.86}$$

   where $0.5 < \epsilon_{mod} < 1$.

3. A standing alone case happens when the two characteristics ($\mathrm{R}_{+_{j-\frac{1}{2}}}$ and $\mathrm{R}_{-_{j-\frac{1}{2}}}$) coming to the cell face correspond to the same Eigen value i.e., speed (Λ_m). Hence, the choice of the local invariant can be chosen by the algorithm based on the minimal variation of the conservation variable as

$$(\mathrm{R})^{\mathrm{n+1}}_{\mathrm{j-\frac{1}{2}}} = \begin{cases} \phi_{max} & \text{if } (\mathrm{R})^{\mathrm{n+\frac{1}{2}}}_{\mathrm{j}} - (\mathrm{R})^{\mathrm{n+\frac{1}{2}}}_{\mathrm{j-1}} < 0, \\ \phi_{min} & \text{if } (\mathrm{R})^{\mathrm{n+\frac{1}{2}}}_{\mathrm{j}} - (\mathrm{R})^{\mathrm{n+\frac{1}{2}}}_{\mathrm{j-1}} \geq 0 \end{cases} \tag{2.87}$$

$$f(\phi_{min}) = min(\Lambda_{j-1}R_+, \Lambda_j R_-) \tag{2.88}$$

$$f(\phi_{max}) = max(\Lambda_{j-1}R_+, \Lambda_j R_-) \tag{2.89}$$

   With ϕ_{min} and ϕ_{max} being the solution variables at which we compute the min and max flux, respectively.

2.6 Extension to gas dynamics equations in three dimensions

To summarize, the general CABARET algorithm in three-dimensions and for hexa-hedral unstructured grids is presented. The Euler equations in three-dimensions can be written as

$$\frac{\partial \mathrm{Q}}{\partial t} + \frac{\partial \mathrm{F}}{\partial x} + \frac{\partial \mathrm{G}}{\partial y} + \frac{\partial \mathrm{H}}{\partial z} = 0 \tag{2.90}$$

Following the previous discussion, the fluxes in the y, z directions are denoted by G and H, with the Jacobians defined by $\mathrm{B} = \frac{d\mathrm{G}}{d\mathrm{U}}$ and $\mathrm{C} = \frac{d\mathrm{H}}{d\mathrm{U}}$ respectively. After applying the divergence theorem to integrate the fluxes over a set of faces (N_f) with surface vectors $dS_{k=1,\ldots,N_f}$ for a given cell (j) of volume (v_j). Figure 2.17 shows an example of a 2D orthogonal grid which shows the cell j and its face k. Also, this orthogonal grid is aligned to x and y directions.

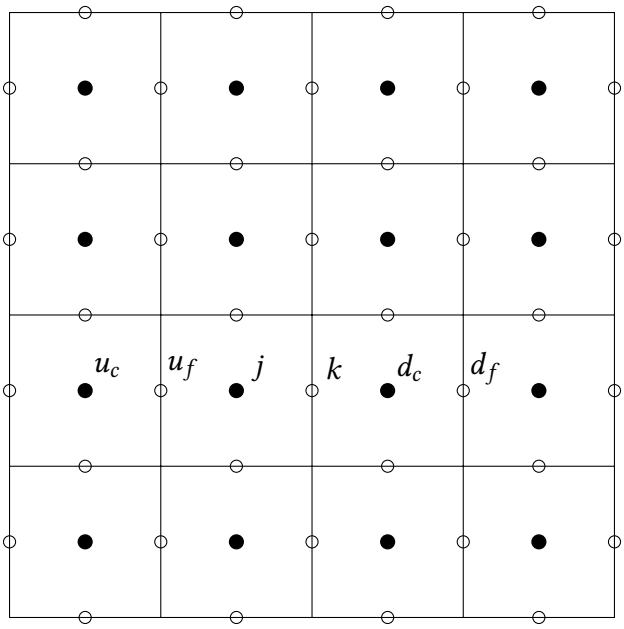

Figure 2.17: A 2D rectangular grid, the conservative variables are at solid circles and the flux variables at the open circles.

- Predictor step, the conservation variables defined at the cell centers at time step $n+\frac{1}{2}$ are computed as

$$v_j \frac{\mathrm{Q}_j^{n+\frac{1}{2}} - \mathrm{Q}_j^n}{0.5\Delta t^n} + \sum_{k=1}^{N_f} \mathrm{F}_k^n dS_{k,x} + \sum_{k=1}^{N_f} \mathrm{G}_k^n dS_{k,y} + \sum_{k=1}^{N_f} \mathrm{H}_k^n dS_{k,z} = 0 \tag{2.91}$$

- Extrapolation step, the characteristic flux variables are computed from the conservative variables $\mathrm{R}_m = \mathrm{L}_m \bigotimes \mathrm{V}$ for all faces of the cell, where m is the number of equations. The characteristic variables are updated using the upwind extrapolation as

$$\mathrm{R}_{m,l,k}^{n+1} = 2\mathrm{R}_{m,l,upstream-cell}^{n+\frac{1}{2}} - \mathrm{R}_{m,l,upstream-face}^{n}, l = 1, \ldots, m \tag{2.92}$$

  Here, the definition of the upstream cell center and the upstream face are defined based on the sign of the corresponding wave speed, i.e., Eigenvalue $\lambda_{l,k}^{n+1}$, evaluated using the face-sharing cell center variables. For example, in Figure 2.17, if the flow is assumed to be from left to right of the domain. Then for the positive Eigenvalue or wave speed the downstream face (d_f) and cell correspond the cell (d_c) next to face k, and the upstream face (u_f) and cell (u_c) are to the left of the cell j. On computing the invariants at the time step $n+1$, the maximum principle is applied depending on the choice of the scheme. Then the Riemann problem is solved using reconstruction procedure to obtain the conservative flux variables at the new time-step Q_j^{n+1}.

- Corrector step, the conservative variables at the new time step are computed using the reconstructed flux variables as

$$v_j \frac{\mathrm{Q}_j^{n+1} - \mathrm{Q}_j^{n+\frac{1}{2}}}{0.5\Delta t^n} + \sum_{k=1}^{N_f} \mathrm{F}_k^{n+1} dS_{k,x} + \sum_{k=1}^{N_f} \mathrm{G}_k^{n+1} dS_{k,y} + \sum_{k=1}^{N_f} \mathrm{H}_k^{n+1} dS_{k,z} = 0 \tag{2.93}$$

  The dispersion improved CABARET scheme is implemented at both the predictor and the corrector step while evaluating the flux vectors. In three-dimensions it is written as

$$(\mathrm{F},\mathrm{G},\mathrm{H})_k^n \rightarrow (\mathrm{F},\mathrm{G},\mathrm{H})_k^n = (\mathrm{F},\mathrm{G},\mathrm{H})(\mathrm{Q}_k^n) + \delta(\mathrm{F},\mathrm{G},\mathrm{H})_k^n \tag{2.94}$$

where the flux modification i.e., the anti-dispersion correction term is given by

$$\delta(\mathrm{F},\mathrm{G},\mathrm{H})_k^n = \frac{\mu_k}{\Delta\bar{h}_k}\left[\frac{(\mathrm{F},\mathrm{G},\mathrm{H})^n_{downstream-face} - (\mathrm{F},\mathrm{G},\mathrm{H})^n_k}{\Delta h_{downstream-cell}}\right] - \frac{\mu_k}{\Delta\bar{h}_k}\left[\frac{(\mathrm{F},\mathrm{G},\mathrm{H})^n_k - (\mathrm{F},\mathrm{G},\mathrm{H})^n_{upstream-face}}{\Delta h_{upstream-cell}}\right] \tag{2.95}$$

with $\Delta\bar{h}_k = 0.5(\Delta h_{downstream-cell} + \Delta h_{upstream-cell})$ and

$$\mu_k = \epsilon_d\left[\Delta h^2_{downstream-cell} - 3\mathrm{CFL}_k\Delta h_{downstream-cell}\Delta\bar{h}_k + 2\mathrm{CFL}_k^2\Delta h^2_{downstream-cell}\right] \tag{2.96}$$

In the above equation, $\Delta h_{downstream-cell}$ and $\Delta h_{upstream-cell}$ are distances between the centers of the opposite cell faces, downstream and upstream to the face k, respectively. The local CFL number is evaluated as

$$\mathrm{CFL}_k = \frac{max(|\Lambda_{k,m}|)\Delta t^n}{\Delta h_{downstream-cell}} \tag{2.97}$$

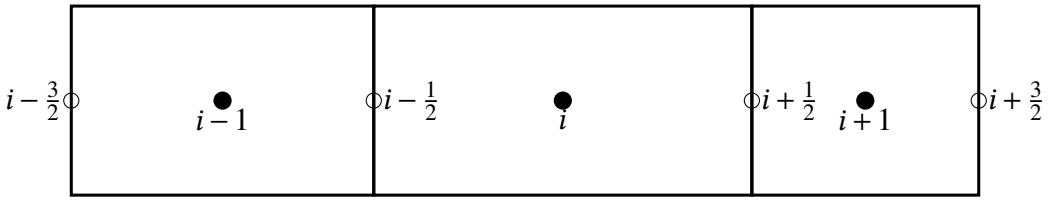

Figure 2.18: The 2D CABARET dispersion stencil, in the x-direction.

For a slow varying mean-flow field (i.e. the wave speeds or the Eigen values remain approximately constant, $\mathrm{A} = \frac{\partial \mathrm{F}}{\partial U} \approx const, \mathrm{B} = \frac{\partial \mathrm{G}}{\partial U} \approx const, \mathrm{C} = \frac{\partial \mathrm{H}}{\partial U} \approx const$), fast propagating acoustic waves, and for an orthogonal grid the

above three-dimensional equations can be treated analogous to the one-dimensional Euler equations. Let us consider the stencil for a 2D grid as shown in Figure 2.18, and the indices (i,j,k) correspond to the x, y, and z-directions. In the x-direction, equation (2.93) can be written for the cell i and dropping j,k indices corresponding to the y and z-directions, as

$$\frac{\mathrm{U}_i^{n+\frac{1}{2}} - \mathrm{U}_i^n}{0.5\Delta t^n} + \frac{\mathrm{F}(\mathrm{U}^n_{i+\frac{1}{2}}) - \mathrm{F}(\mathrm{U}^n_{i-\frac{1}{2}})}{\Delta x_i} = \frac{\mu_{i+\frac{1}{2}}}{\Delta \bar{x}_{i+\frac{1}{2}}}\left[\frac{\mathrm{F}(\mathrm{U}^n_{i+\frac{3}{2}}) - \mathrm{F}(\mathrm{U}^n_{i+\frac{1}{2}})}{\Delta x_{i+1}} - \frac{\mathrm{F}(\mathrm{U}^n_{i+\frac{1}{2}}) - \mathrm{F}(\mathrm{U}^n_{i-\frac{1}{2}})}{\Delta x_i}\right] - \frac{\mu_{i-\frac{1}{2}}}{\Delta \bar{x}_{i-\frac{1}{2}}}\left[\frac{\mathrm{F}(\mathrm{U}^n_{i+\frac{1}{2}}) - \mathrm{F}(\mathrm{U}^n_{i-\frac{1}{2}})}{\Delta x_i} - \frac{\mathrm{F}(\mathrm{U}^n_{i-\frac{1}{2}}) - \mathrm{F}(\mathrm{U}^n_{i-\frac{3}{2}})}{\Delta x_{i-1}}\right] + \mathrm{Q}_i \tag{2.98}$$

where

$$\mathrm{Q}_i = \frac{\mathrm{G}(\mathrm{U}^n_{j+\frac{1}{2}}) - \mathrm{G}(\mathrm{U}^n_{j-\frac{1}{2}})}{\Delta y_j} - \frac{\mathrm{H}(\mathrm{U}^n_{k+\frac{1}{2}}) - \mathrm{H}(\mathrm{U}^n_{k-\frac{1}{2}})}{\Delta z_k} \tag{2.99}$$

and CFL_i from equation (2.9) is given by

$$\mathrm{CFL}_i = \frac{max(|\lambda_{1,x}|, |\lambda_{2,x}|, ..., |\lambda_{m,x}|)\Delta t^n}{\Delta x_i} \tag{2.100}$$

By multiplying both sides of the equation (2.99) by the left Eigen matrix $\mathrm{L} \approx const$, the system decouples into m equations for each Riemann variant $p = 1, 2, ..., m$ in the x-direction with source term Q as

$$\frac{\mathrm{R}^{n+\frac{1}{2}}_{x,p,i} - \mathrm{R}^n_{x,p,i}}{0.5\Delta t^n} + \lambda_{x,p}\frac{\mathrm{R}^n_{x,p,i+\frac{1}{2}} - \mathrm{R}^n_{x,p,i-\frac{1}{2}}}{\Delta x_i} = \lambda_{x,p}\frac{\mu_{i+\frac{1}{2}}}{\Delta \bar{x}_{i+\frac{1}{2}}}\left[\frac{\mathrm{R}^n_{x,p,i+\frac{3}{2}} - \mathrm{R}^n_{x,p,i+\frac{1}{2}}}{\Delta x_{i+1}} - \frac{\mathrm{R}^n_{x,p,i+\frac{1}{2}} - \mathrm{R}^n_{x,p,i-\frac{1}{2}}}{\Delta x_i}\right] - \lambda_{x,p}\frac{\mu_{i-\frac{1}{2}}}{\Delta \bar{x}_{i-\frac{1}{2}}}\left[\frac{\mathrm{R}^n_{x,p,i+\frac{1}{2}} - \mathrm{R}^n_{x,p,i-\frac{1}{2}})}{\Delta x_i} - \frac{\mathrm{R}^n_{x,p,i-\frac{1}{2}} - \mathrm{R}^n_{x,p,i-\frac{3}{2}}}{\Delta x_{i-1}}\right] + \mathrm{Q}_{x,p,i} \tag{2.101}$$

here, $\mathrm{Q}_{x,p,i}$ is the corresponding component of the matrix $\mathrm{L}_x \bigotimes \mathrm{Q}_i$. And

the expression for $\mu_i + \frac{1}{2}$ becomes identical to (2.9) as

$$\mu_{i+\frac{1}{2}} = \epsilon_d \left(\Delta x^2_{i+\frac{1}{2}} - 3\mathrm{CFL}\Delta x_{i+\frac{1}{2}} \Delta \bar{x}_i + 2\mathrm{CFL}^2 \Delta x^2_{i+\frac{1}{2}} \right) \tag{2.102}$$

2.7 Summary

- This chapter presented the new dispersion improved CABARET scheme as a development to the CABARET method for the advection equation and the one-dimensional and three-dimensional Euler equations.
- Linear stability analysis demonstrated a significant reduction in the dispersion error while keeping the scheme non-dissipative. Additionally, the optimal anti-dispersion term was found to be $\frac{-1}{12}$.
- The non-linear CABARET schemes which are to be used along with the dispersion improvement CABARET have been proposed. Furthermore, a switch was also presented used to zero the anti-dispersion term in regions of strong gradients. The relevant Riemann solver used in the CABARET solver and the boundary conditions are also presented.
- The dispersion improved CABARET scheme has been implemented for various linear advection test cases and followed by, linear and non-linear isothermal gas dynamics problems, and Euler equation problem. These are all presented in Chapter 4.

The following Chapter presents the viscous modelling of the Navier-Stokes equations.

Chapter 3

Viscous modelling

The previous Chapter discussed the CABARET scheme and its variants applied to the Euler equations. The present chapter describes the modelling of viscous fluxes exclusively. The chapter is organised as follows. The Navier-Stokes (NS) equations are presented in section 3.1 along with the different viscous modelling methods used in the present work.

3.1 Navier-Stokes equations

The three-dimensional Navier-Stokes equations in conservative form can be written by including the diffusive fluxes (denoted by the subscript v) along with the convective fluxes as

$$\frac{\partial \mathrm{Q}}{\partial t} + \frac{\partial (\mathrm{F} - \mathrm{F}_v)}{\partial x} + \frac{\partial (\mathrm{G} - \mathrm{G}_v)}{\partial y} + \frac{\partial (\mathrm{H} - \mathrm{H}_v)}{\partial z} = 0 \tag{3.1}$$

$$\mathrm{Q} = \begin{bmatrix} \rho \\ \rho u \\ \rho v \\ \rho w \\ \rho E \end{bmatrix}, \tag{3.2}$$

$$\mathrm{F} = \begin{bmatrix} \rho u \\ \rho u^2 + p \\ \rho uv \\ \rho uw \\ (\rho E + p)u \end{bmatrix}, \quad \mathrm{F}_v = \begin{bmatrix} 0 \\ \tau_{xx} \\ \tau_{yx} \\ \tau_{zx} \\ \tau_{xx}u + \tau_{yy}v + \tau_{xz}w - q_x \end{bmatrix}, \tag{3.3}$$

$$\mathrm{G} = \begin{bmatrix} \rho v \\ \rho vu \\ \rho v^2 + p \\ \rho vw \\ (\rho E + p)v \end{bmatrix}, \quad \mathrm{G}_v = \begin{bmatrix} 0 \\ \tau_{xy} \\ \tau_{yy} \\ \tau_{zy} \\ \tau_{yx}u + \tau_{yy}v + \tau_{yz}w - q_y \end{bmatrix}, \tag{3.4}$$

$$\mathrm{H} = \begin{bmatrix} \rho w \\ \rho wu \\ \rho wv \\ \rho w^2 + p \\ (\rho E + p)w \end{bmatrix}, \quad \mathrm{H}_v = \begin{bmatrix} 0 \\ \tau_{xz} \\ \tau_{yz} \\ \tau_{zz} \\ \tau_{zx}u + \tau_{zy}v + \tau_{zz}w - q_z \end{bmatrix} \tag{3.5}$$

The viscous stress terms τ and the thermal stress q are given by

$$\tau_{xx} = 2\mu_f \frac{\partial u}{\partial x} + \lambda_f \left(\frac{\partial u}{\partial x} + \frac{\partial v}{\partial y} + \frac{\partial w}{\partial z} \right) \tag{3.6}$$

$$\tau_{yy} = 2\mu_f \frac{\partial v}{\partial y} + \lambda_f \left(\frac{\partial u}{\partial x} + \frac{\partial v}{\partial y} + \frac{\partial w}{\partial z} \right) \tag{3.7}$$

$$\tau_{zz} = 2\mu_f \frac{\partial w}{\partial z} + \lambda_f \left(\frac{\partial u}{\partial x} + \frac{\partial v}{\partial y} + \frac{\partial w}{\partial z} \right) \tag{3.8}$$

$$\tau_{xy} = \tau_{yx} = \mu_f \left(\frac{\partial u}{\partial y} + \frac{\partial v}{\partial x} \right) \tag{3.9}$$

$$\tau_{xz} = \tau_{zx} = \mu_f \left(\frac{\partial u}{\partial z} + \frac{\partial w}{\partial x} \right) \tag{3.10}$$

$$\tau_{yz} = \tau_{zy} = \mu_f \left(\frac{\partial v}{\partial z} + \frac{\partial w}{\partial y} \right) \tag{3.11}$$

$$q_x = -k_f \frac{\partial T}{\partial x} \tag{3.12}$$

$$q_y = -k_f \frac{\partial T}{\partial y} \tag{3.13}$$

$$q_z = -k_f \frac{\partial T}{\partial z} \tag{3.14}$$

In addition to the notation used in section 2.5, the coefficient of dynamic viscosity (denoted by μ_f) of the fluid, the second viscosity coefficient (denoted by λ_f) of the fluid, and the coefficient of thermal conductivity (denoted by k_f) of the fluid. The temperature is denoted by T and the system is closed by the equation of state $p = \rho R_{gas} T$, where R_{gas} is the specific gas constant. Also, the coefficient of thermal conductivity and coefficient of dynamic viscosity are related by the Prandtl number (Pr) as

$$k_f = \frac{\mu_f C_p}{Pr}, \quad C_p = \frac{\gamma R_{gas}}{\gamma - 1} \tag{3.15}$$

Here, C_p is the specific heat coefficient of the gas at constant pressure, γ is ratio of specific heats of the gas. Also, the coefficient of dynamic viscosity varies with temperature according to Sutherland's law and for air, it is given in metric system (Kelvin for temperature) by

$$\mu_f(T) = \mu_{f,\infty} \left(\frac{T}{T_\infty} \right)^{1.5} \frac{T_\infty + T_s}{T + T_s} \tag{3.16}$$

where, $T_s = 110.4K$ is the Sutherland's constant, $T_\infty = 273.15K$ is the reference temperature and $\mu_{f,\infty} = 1.715 \times 10^{-5} \frac{Kg}{ms}$ is the reference dynamic viscosity of air. Also, for the working fluid air the $R_{gas} = 287.14 \frac{J}{KgK}$, $C_p = 1005 \frac{J}{KgK}$, $\gamma = 1.4$, $k_f = 0.0242 \frac{W}{mK}$ and $Pr = 0.72$. It is to be noted that the second viscosity coefficient λ_f is evaluated using the coefficient of bulk viscosity $\mu_{B,f}$, either using the Stokes hypothesis which implies $\mu_{B,f} = 0$ for a monoatomic gas, or as $\mu_{B,f} = \lambda_f + \frac{2}{3}\mu_f$.

The viscous fluxes are separately evaluated at the predictor and the corrector steps using the conservative variables. To obtain the conservative variables at the faces, different averaging procedures may be used. Here, two methods are considered. Namely, the Vertex method and the collocated method, and they are described below. Also, it can be seen that the computation of the viscous fluxes mainly involves the averaging procedure to obtain the face variable and the evaluation of the velocity ($\frac{\partial \vec{q}}{\partial x}, \frac{\partial \vec{q}}{\partial y}, \frac{\partial \vec{q}}{\partial z}$, where $\vec{q} = [u, v, w]$) and temperature derivatives ($\frac{\partial T}{\partial x}, \frac{\partial T}{\partial y}, \frac{\partial T}{\partial z}$). It is to be noted that the present methods are suggested given the in-house unstructured CABARET solver.

Unstructured grids depend on the mapping information to define the grid topology. A typical 3D grid has sets of nodes, faces and cells. Associated with these sets are the mappings from faces to nodes (such as a quad-face having a list of 4 nodes) and cells to faces (such as cells adjacent to a face), and data on sets such as residual on the cells, face normal of the faces, co-ordinates of the nodes. An 2D example unstructured grid is shown in Figure 3.1 with the sets, mapping and datasets.

The grid consists of nodes, edges and cells. Consider the node list each with its own co-ordinates as shown:

$n_1 = (x_1, y_1)$

$n_2 = (x_2, y_2)$

$n_3 = (x_3, y_3)$

$n_4 = (x_4, y_4)$

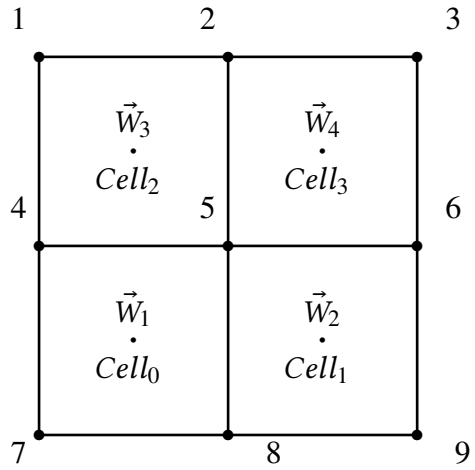

Figure 3.1: An example of 2D mesh, with Cells 0,1,2,3 and Nodes from 1 to 9.

$n_5 = (x_5, y_5)$

$n_6 = (x_6, y_6)$

$n_7 = (x_7, y_7)$

$n_8 = (x_8, y_8)$

$n_9 = (x_9, y_9)$

the subscript of each line in the list represents the node number. Using these node numbers the edge list is built, which connects 2 nodes:

$e_1 -> (n_1, n_2)$

$e_2 -> (n_2, n_3)$

$e_3 -> (n_3, n_6)$

$e_4 -> (n_6, n_9)$

$e_5 -> (n_9, n_8)$

$e_6 -> (n_8, n_7)$

$e_7 -> (n_7, n_4)$

$e_8 -> (n_4, n_1)$

$e_9 -> (n_4, n_5)$

$e_{10} -> (n_5, n_6)$

$e_{11} -> (n_5, n_2)$

$e_{12} -> (n_8, n_5)$

where the number of the line in this list represents the edge number. The mapping from cells to edges is built by using the right hand rule such that an edge e_{11} consisting of nodes n_5 and n_2 will have cells c_3 and c_2 on its left and right side, respectively.

3.1.1 Vertex method

The vertex approach is currently used in in-house three-dimensional CABARET code (CFOAM) as described in Faranosov et al. (2013b). Consider the example grid shown in Figure 3.2 where numbers and alphabets, respectively name the indices on the horizontal axis (x-axis) and the vertical axis (y-axis).

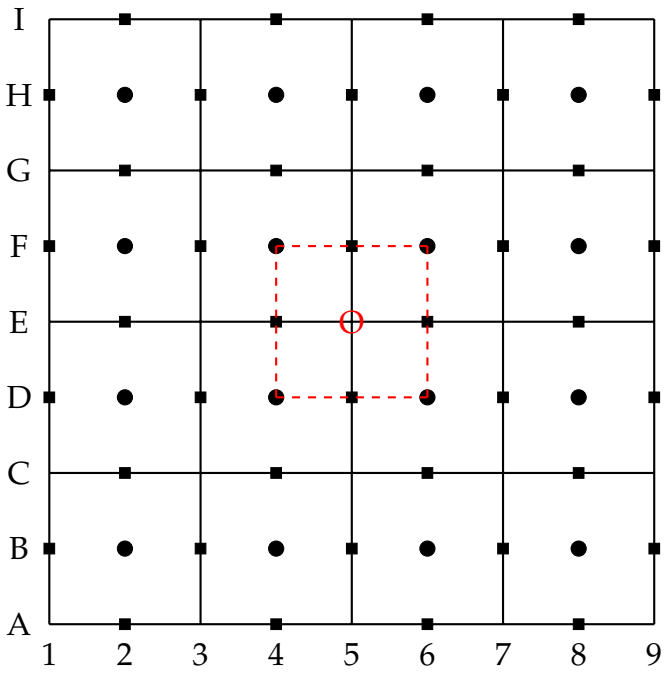

Figure 3.2: A typical 2D mesh with dots representing the cell centers, boxes representing face centers and vertex with 'O'

In the vertex method, the cell-vertex value of a scalar ϕ at the vertex O shown in Figure 3.2 is obtained by volume (denoted by Ω) averaging using the neighbouring cells.

$$\phi_O = \frac{\sum_{i=1,..nc} \Omega_i \phi_i}{\sum_{i=1,..nc} \Omega_i} \tag{3.17}$$

where nc is the number of cells that include the vertex O. From the example grid, the vertex 'O' at E5 can be seen a fictitious cell with centre E5 with vertices D4, D6, F4, and F6.

In the next step, the cell-center gradients are obtained by averaging the vertex values. Hence, the gradient in the x-direction at face center E6 is written as

$$\left(\frac{\partial \phi}{\partial x}\right)_{E6} = \frac{\phi_{E7} - \phi_{E5}}{l_{E5E7}} \tag{3.18}$$

This method requires the cell neighbours sharing the vertices resulting in a larger stencil than the face-sharing neighbours. Also, additional storage of flow variables at the vertex points and mapping between the faces and vertices are needed. However, it can be readily parallelised as there are no race conditions in the reduction operation at equation (3.17), and the method is second-order accurate for smooth grids and first-order accurate for arbitrarily stretched meshes (Crumpton et al., 1993).

3.1.2 Collocated method

The collocated approach uses the cell-face stencil used in the computation of the convective fluxes. In the first step, the Green-Gauss theorem is used to compute the cell center gradient from the scalar value at the faces of that cell. The gradient at the cell-center, say at cell center $D6$, can be computed using the divergence theorem as

$$\nabla \phi_{D4} = \frac{1}{\Omega_{D4}} \sum_{i=1}^{N_f} \phi_i \vec{S}_i \tag{3.19}$$

Here, $\vec{S}$ is the face normal of the face and N_f is the number of faces of the cell. The face value ϕ (say at $D5$) is obtained by averaging the face sharing cells values as $\phi_{D5} = 0.5(\phi_{D4} + \phi_{D6})$.

Furthermore, the gradients on the cell-face can be computed using the obtained cell-gradients and edge weights as

$$\nabla\phi_{(D5)} = \omega_{(D5)}\nabla\phi_{(D4)} + \left[1 - \omega_{(D5)}\right]\nabla\phi_{(D6)} \tag{3.20}$$

here, ω (Karabasov, 2015) is the interpolation parameter based on the distance between face-sharing cell centers. It is evaluated as

$$\omega_{(D5)} = 0.5\left(1 + \frac{l_{D5D6}}{l_{D4D6}} - \frac{l_{D4D5}}{l_{D4D6}}\right) \tag{3.21}$$

with l_{D5D6} being the distance between points $D5$ and $D6$.

This method may result in the decoupling of the cell value $D4$ from the gradient (Crumpton et al., 1993; Blazek, 2005), when the interpolation parameter ω is close to 0.5 i.e. for equi-distant cells. This is the checker board problem encountered in central schemes. And this is mitigated by correcting the face gradient using the directional derivative or a simple central-difference $\frac{\partial\phi}{\partial l}$

$$\nabla\tilde{\phi}_{(D5)} = \nabla\phi_{(D5)} + \left[\frac{\partial\phi}{\partial l} - \nabla\phi_{(D5)}.\vec{k}\right]\vec{k} \tag{3.22}$$

where, $\nabla\tilde{\phi}$ is the corrected face-gradient, $\vec{k}$ is the unit vector from cell centers $D4$ and $D6$. And the directional derivative is given by

$$\frac{\partial\phi}{\partial l} = \frac{\phi_{(D6)} - \phi_{(D4)}}{l_{D4D6}}, \tag{3.23}$$

Hence, the collocated method results in two steps, first, consisting of cell gradient computation and secondly, computing and correcting the face-gradient.

This method results in a stencil containing a cell and its immediate face-sharing neighbours, resulting in a 5 cell stencil for a 2D mesh with quadrilateral cells and a 7 cell stencil for a 3D mesh with hexahedral cells. Due to the use of already existing variables, this method uses less memory and uses a smaller stencil. Although, due to the race condition in the update operation in equation (3.19), it is not straight-forward to parallelise. In the present work, the vertex approach was replaced with the more efficient collocated approach, due to the cell-centred stencil already in use in the in-house solver.

3.1.3 Gradient on boundary

In the CABARET solver, the gradients on the boundary faces are evaluated depending on the type of the boundary. For a typical boundary face k, shown in Figure 3.3, with owner cell i and opposing face m, the gradient on the boundary face can be directly computed using parabolic interpolation for accurate second-order gradient or a simple linear interpolation. Both these approaches are used in the CABARET solver.

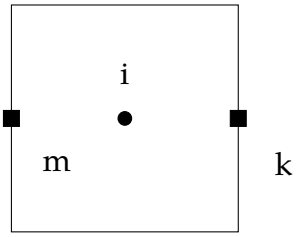

Figure 3.3: A boundary face (k) with its owner cell (i) and opposing face (m).

Let 'h' be the distance between the points k and m. Then the gradient of a scalar ϕ can be written in terms of the unit face normal ($\vec{n}_k$) of face k pointing out of the domain. The velocity gradient on face k is presented for different boundary types in Table 3.1. Note that a linear interpolation has been used for pressure boundaries. The subsequent section describes the turbulence model that is also added to the in-house solver.

Boundary type	$\nabla\vec{q}$
Viscous wall	$\frac{1}{h}(4\vec{q}_i - \vec{q}_m)\vec{n}_k$
Symmetry and Inviscid wall	$\frac{1}{h}(4\vec{q}_i - \vec{q}_m + 3\vec{q}_k)\vec{n}_k$
Pressure boundaries	$\frac{1}{h}(2\vec{q}_i - \vec{q}_k)\vec{n}_k$

Table 3.1: Boundary face gradients of velocity using parabolic interpolation.

3.2 Summary

- This chapter presented the modelling of the viscous fluxes in the Navier-Stokes equations using two different approaches, i.e., the vertex approach and the collocated approach. The vertex approach needs a larger stencil which involves the vertex neighbours, whereas, the collocated approach needs only the neighbours of the cell.

- The vertex approach in the in-house CABARET solver was updated to the collocated approach and is expected to be faster than the vertex approach. The corresponding results are presented in Chapter 4.

The following chapter presents the numerical results for the various improvements to the in-house CABARET solver thus far.

Chapter 4

Numerical results

The CABARET schemes presented in the earlier chapters are demonstrated in the present chapter for different test cases. Firstly, section 4.1 the linear advection equation using the CABARET variants with the dispersion improvement are applied to different initial profiles. Secondly, in section 4.2 the CABARET variants are applied to the pressure wave propagation in one-, two-, and three-dimensions, followed by the non-linear wave propagation. Thirdly, in section 4.4 the validation of the efficient viscous modelling is presented.

Briefly, the CABARET schemes are summarised as follows. The CABARET scheme without any flux correction (denoted by P-CAB), the CABARET scheme with non-linear flux correction (denoted by F-CAB), followed by the relaxed correction CABARET scheme (denoted by R-CAB), the modified relaxation CABARET scheme (denoted by MR-CAB), and finally, the addition of the limiter to the MR-CAB scheme (denoted by MR-CAB-LIM). The suffix DISP denotes the dispersion improvement. It is to be noted that the improved dispersion properties are notably observed for small CFL and high wave numbers as shown from the stability analysis.

4.1 1D Linear Advection

The different CABARET relaxation variants described in section 2.3 with and without the anti-dispersion term have been applied to convect various initial test functions.

The purpose of the present section was to find the tunable relaxation parameter (here we use ϵ and drop the subscript for ease of reading) for both the

R-CAB (ϵ_{rx}) and the MR-CAB (ϵ_{mrx}) schemes. A trail and error approach was used to find the effect and range of ϵ value to advect different initial profiles. Notably, the test cases involving a rectangular shape and a rectangular shape with a superimposed cosine wave are used to find a suitable value of ϵ. And this value of ϵ is used for linear wave propagation and gas dynamics problems.

The first test case consists of a Gaussian modulated cosine wave given by equation (4.1), the parameter β is varied to control the modulation. In the present work the values of 10, 25, and 5, for β resulting in test cases A, B, and C, respectively.

A rectangular pulse of amplitude 1.0 is the second test case given by equation (4.2) referred to as Case R. The next test case consists of a triangular pulse of amplitude 1.0 is the final test case given by equation (4.3) referred to as Case T. The next test case Y corresponds to a high-frequency, low amplitude travelling wave solution, given by equation (4.4).

Finally, the test case Z is a combination of the rectangular test case appended by a cosine wave. The amplitude of the travelling wave was taken to be 2% of the height of the rectangular wave. The initial profile is an attenuation of a high-frequency cosine and low amplitude wave on the rectangular wave, given by equation (4.6). This test case is reflective of acoustic waves in the presence of hydrodynamic waves.

The initial conditions for the test cases A,B,C,R,T, Y and Z are shown in Figures 4.1a, 4.1b, 4.1c, 4.2a, 4.2b 4.2c, and 4.3 respectively.

Mainly, the test case R and test case Z, which represent a strong gradient and also a high-frequency wave attenuation, are then tested for the sensitivity with the tunable parameter. Finally, the optimal CABARET schemes are compared to the fourth-order accurate Dispersion Relation Preserving (DRP) scheme of Tam and Webb (1993b).

All test cases are performed on a periodic domain of length [-200,200], for

100 time steps with a constant wave speed of 1.0. Also, subsequent finer meshes were obtained by halving the grid spacing. The order of accuracy (OOA) has been evaluated using the standard L1 norm of the absolute error ($\frac{\sum|u_{exact}-u_{scheme}|}{N_{points}}$).

The order of accuracy tables are shown in Appendix A for the above test cases. The MR-CAB-DISP is presented in section A.1.3, followed by the DRP scheme in section A.1.1, the F-CAB scheme in section A.1.2 and the P-CAB is presented in section A.1.4.

$$u(x,t=0) = \left(2+cos\left(\frac{3\pi x}{10}\right)\right) exp\left(-log(2)\left(\frac{x}{\beta}\right)^2\right) \tag{4.1}$$

$$u(x,t=0) = \begin{cases} 1.0, -25 \leq x \leq 25 \\ 0, \text{otherwise} \end{cases} \tag{4.2}$$

$$u(x,t=0) = \begin{cases} \frac{x}{25}, 0 \leq x \leq 25 \\ 2-\frac{x}{25}, 25 \leq x \leq 50 \\ 0, \text{otherwise} \end{cases} \tag{4.3}$$

$$u(x,t=0) = 0.01cos(\frac{\pi x}{10}), 200 \leq x \leq -200 \tag{4.4}$$

$$u(x,t=0) = \begin{cases} 1+0.01cos\left(\frac{\pi x}{5}\right), -20\pi \leq x \leq 20\pi \\ 0.01cos(\frac{\pi x}{5}), \text{otherwise} \end{cases} \tag{4.5}$$

$$u(x,t=0) = \begin{cases} 1.0, -25 \leq x \leq 25 \\ 1.0+\frac{1}{20}cos\left(\frac{\pi x}{4}\right), 30 \leq x \leq -30 \end{cases} \tag{4.6}$$

The test case A previously mentioned is a Gaussian modulated cosine wave. The OOA of the scheme was observed to in the range of 1.85 to 2.0 for all variants of schemes (see tables A.5, A.30, and A.14, respectively). As shown in Figures 4.4 to 4.7, the dispersion variant of the R-CAB and the MR-CAB preserved the peak.

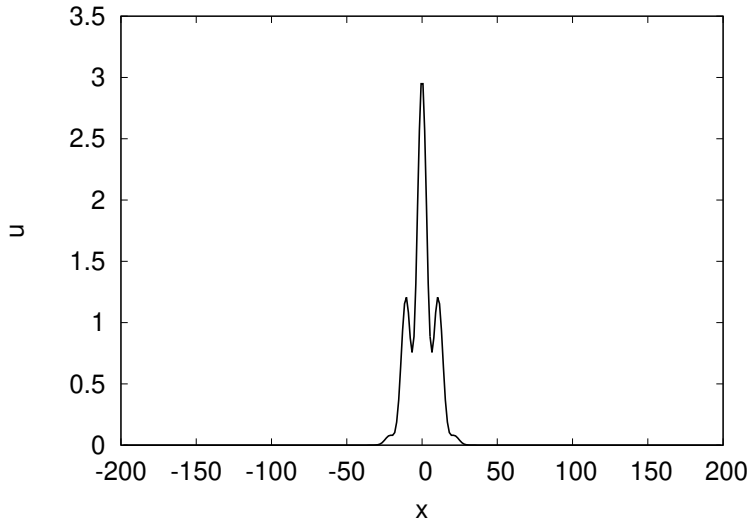

(a) Test case A

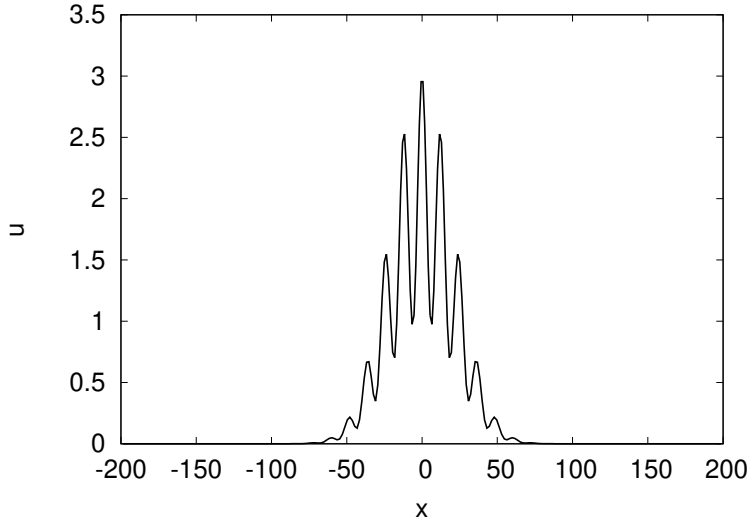

(b) Test case B

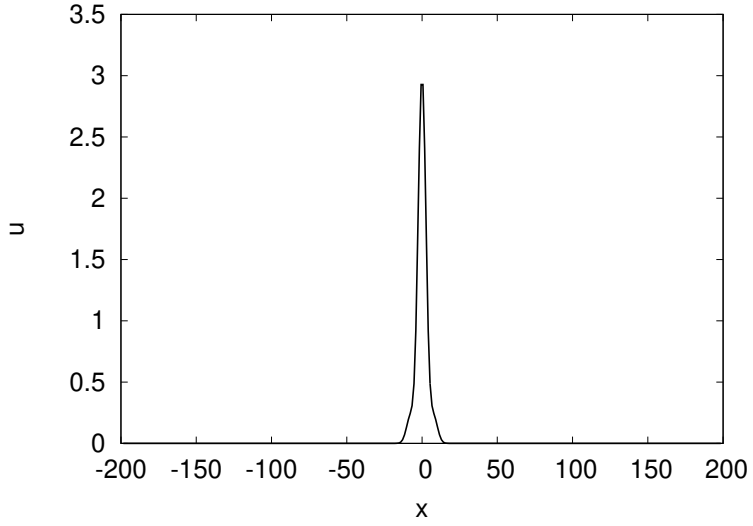

(c) Test case C

Figure 4.1: 1D convection test case initial conditions for profiles A, B, and C

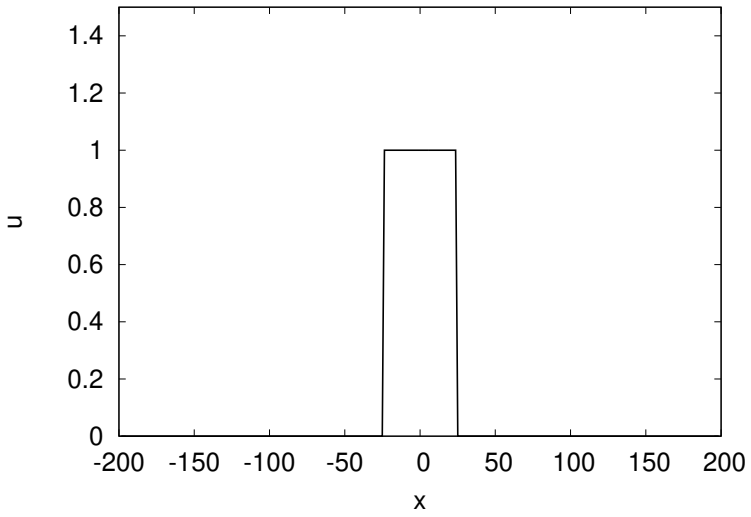

(a) Test case R

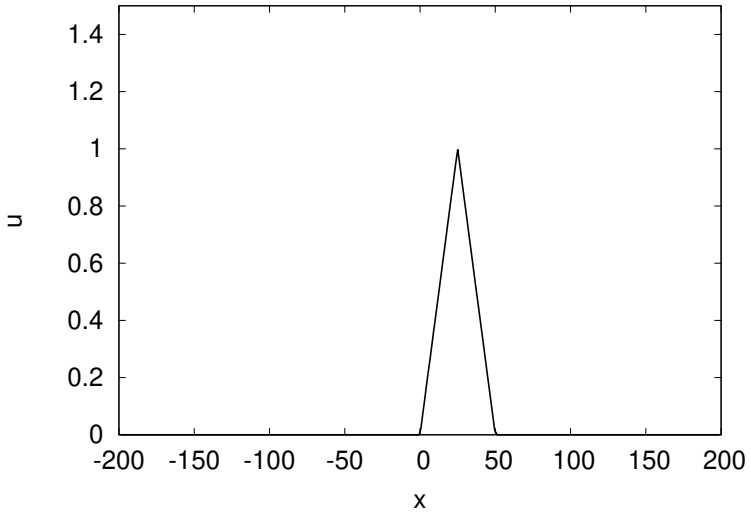

(b) Test case T

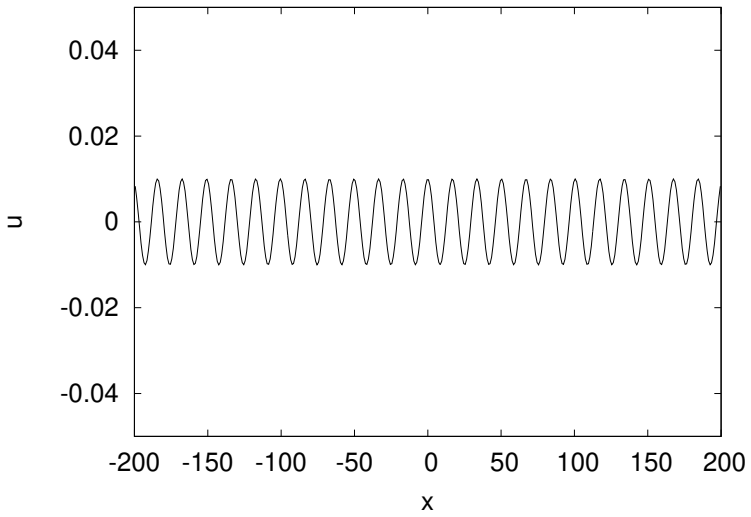

(c) Test case Y

Figure 4.2: 1D convection test case initial conditions for profiles R, T and Y

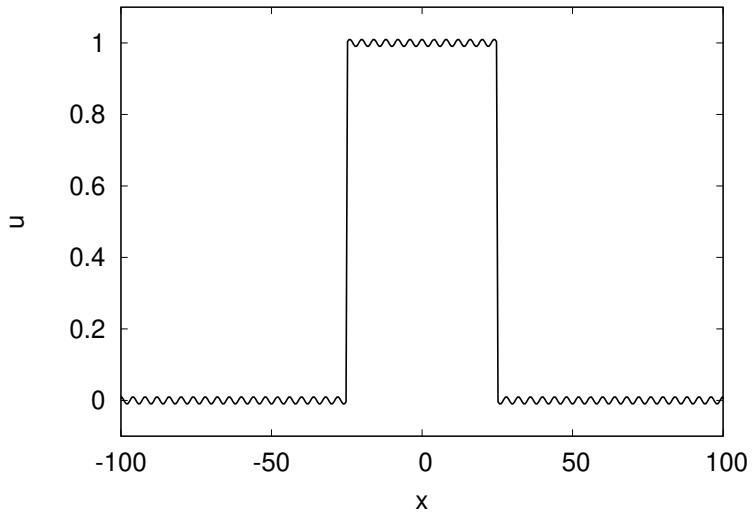

Figure 4.3: Test case Z, showing domain from -100 to 100

However, the MR-CAB-DISP scheme particularly preserved well both the peak of the profile as well as the corners of the wave. It can also be seen the addition of the anti-dispersion term has significant improvement to the MR-CAB scheme.

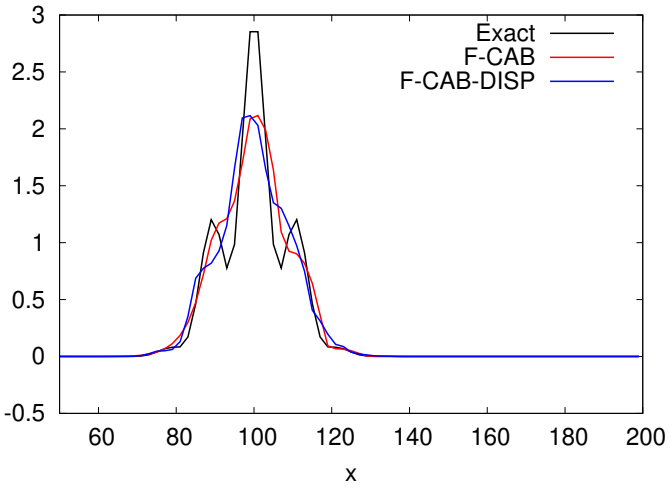

Figure 4.4: Test Case A : Comparison of F-CAB and F-CAB-DISP schemes

For the test case B, the observed OOA was also close to 2.0 (see tables A.6 for F-CAB, A.15 for MR-CAB-DISP, and A.24 for P-CAB convergence rates) and the dispersion variants of the MR-CAB scheme and the R-CAB scheme captured the sharp features of the wave. The results are shown in Figures 4.8 to 4.11.

The OOA for the test case C was observed to be in the range of 1.5 to 2.0 (see tables A.7 for F-CAB, A.16 for MR-CAB-DISP, and A.25 for P-CAB convergence

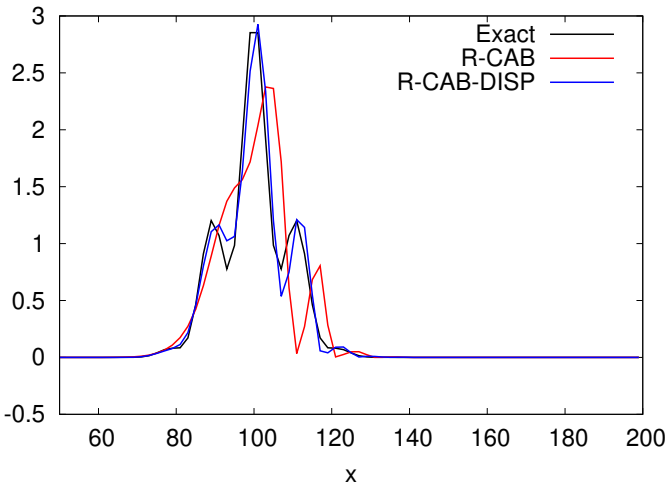

Figure 4.5: Test Case A : Comparison of R-CAB and R-CAB-DISP schemes

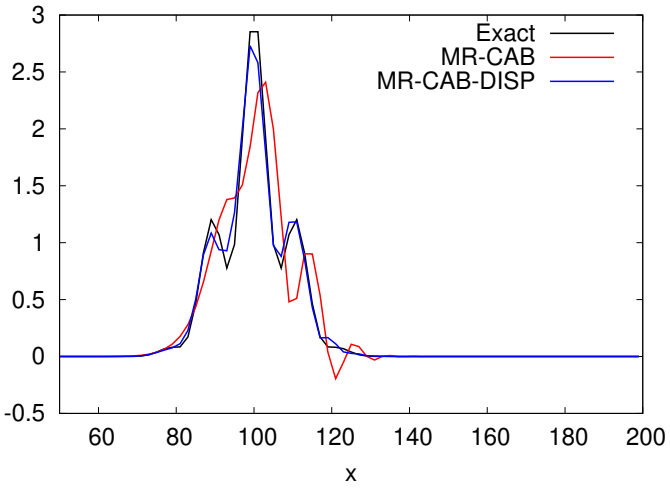

Figure 4.6: Test Case A : Comparison of MR-CAB and MR-CAB-DISP schemes

rates). As shown in Figures 4.12 to 4.15. It can be seen that the dispersion variant of the R-CAB scheme captures the peak closely but introduces oscillations at the base of the pulse. On the other hand, the dispersion variant of the MR-CAB scheme moderately captures the peak while preserving the base of the pulse.

The test case R resembles shock-like features. The F-CAB scheme designed to capture such waves captures the wave very well. On the other hand, only the dispersion variant of the MR-CAB preserved the sharp features reasonably well and close to the F-CAB scheme. It is to be noted that the R-CAB scheme introduces oscillations. The results are presented in Figures 4.16 to 4.19. The OOA for this test case was observed to be close to 0.5 (see tables A.8 for F-CAB,

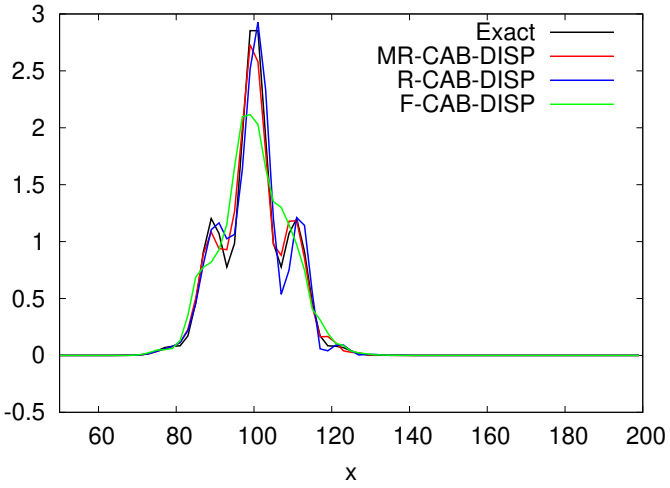

Figure 4.7: Test Case A : Comparison of F-CAB-DISP, R-CAB-DISP and MR-CAB-DISP schemes

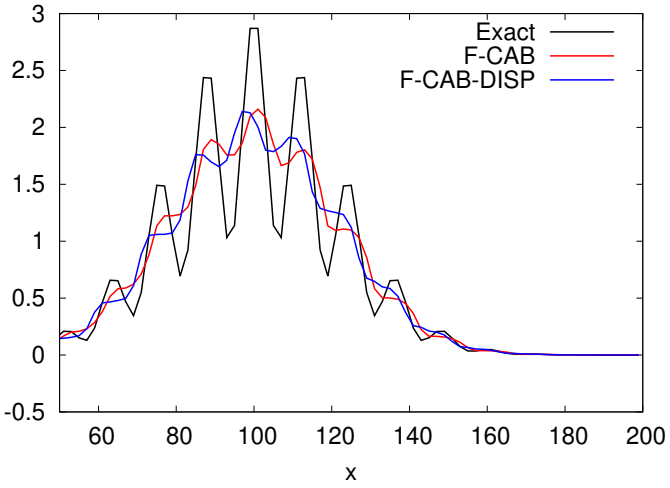

Figure 4.8: Test Case B : Comparison of F-CAB and F-CAB-DISP schemes

A.17 for MR-CAB-DISP, and A.26 for P-CAB convergence rates).

The test case T is similar to the test case C, apart from a sharp peak, the wave is otherwise smooth everywhere else. As shown in Figures 4.20 to 4.23, all variants of the CABARET scheme capture the wave well. Particularly, the dispersion variants of R-CAB and MR-CAB capture the peak better than the F-CAB scheme. The OOA was observed to be in the 1.25 (see tables A.9 for F-CAB, A.18 for MR-CAB-DISP, and A.27 for P-CAB convergence rates).

The test case Y is a cosine wave of high frequency and low amplitude propagated in the domain. The results are presented in Figures 4.24 to 4.27. It is

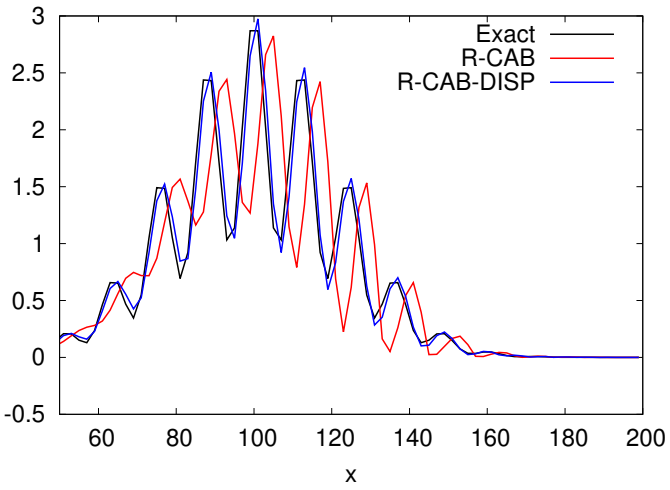

Figure 4.9: Test Case B : Comparison of R-CAB and R-CAB-DISP schemes

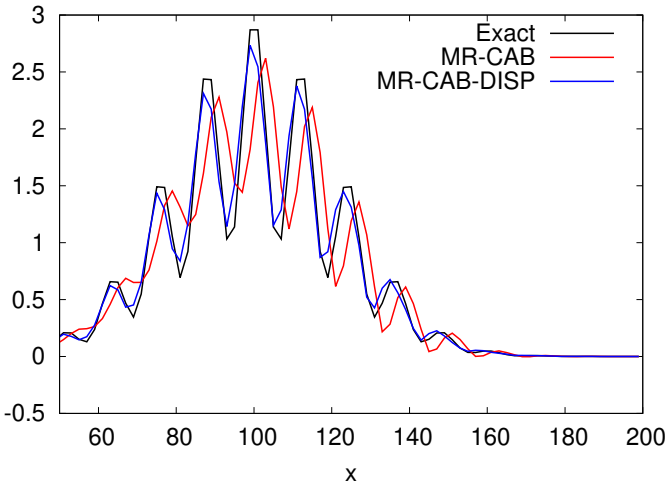

Figure 4.10: Test Case B : Comparison of MR-CAB and MR-CAB-DISP schemes

observed that the F-CAB and its dispersion variant fail to capture the amplitude of the wave, whereas, both the R-CAB and MR-CAB capture the wave very well. However, the dispersion variants of the R-CAB scheme captures the peaks slightly better than the MR-CAB dispersion variant. The OOA for this test case was close to 2.0 (see tables A.10 for F-CAB, A.19 for MR-CAB-DISP, and A.28 for P-CAB convergence rates).

The final test case consists of multiple waves with distinct features as discussed. The results are presented in Figures 4.28 to 4.31. It is seen that as expected from the previous test cases R and Y, that the dispersion variant of the MR-CAB scheme captures both the rectangle and the smaller amplitude wave.

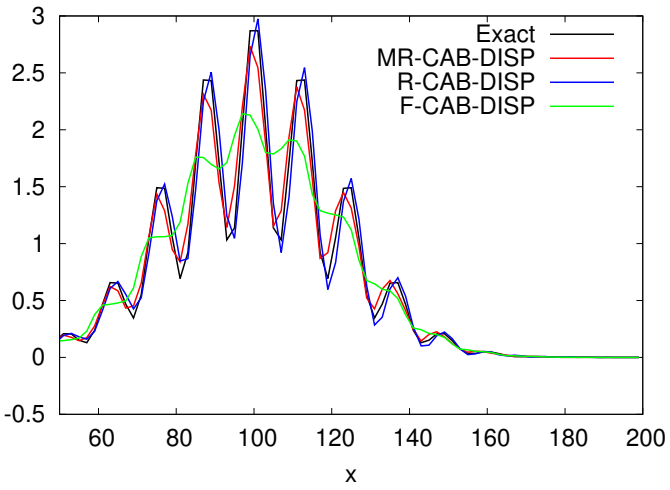

Figure 4.11: Test Case B : Comparison of F-CAB-DISP, R-CAB-DISP and MR-CAB-DISP schemes

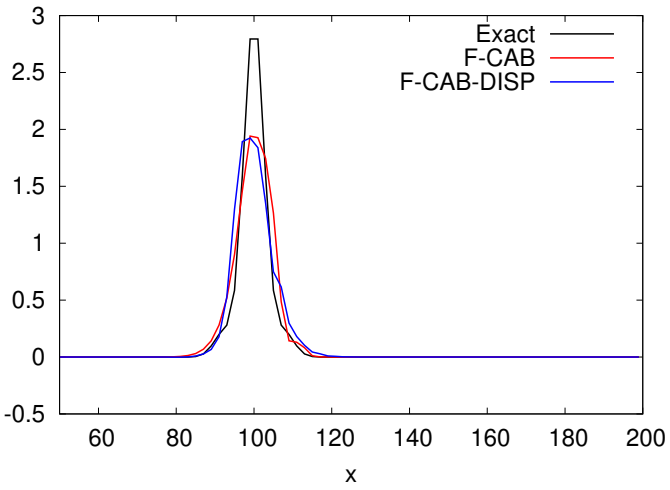

Figure 4.12: Test Case C : Comparison of F-CAB and F-CAB-DISP schemes

In Figures 4.32 to 4.35 the floor of wave is shown. It is seen that the smaller waves are captured well by the dispersion variants of R-CAB and MR-CAB schemes as observed in test case Y. Also, shown in Figures 4.36 to 4.39 the top of the rectangular wave, the desirable features of preserving both the rectangular wave and the high-frequency wave was achieved by the dispersion variant of the MR-CAB scheme. The convergence rates for the MR-CAB-DISP scheme and the F-CAB was close to 0.7, and the P-CAB scheme was observed to have a an OOA of 0.47 (see tables A.11 for F-CAB, A.20 for MR-CAB-DISP, and A.29 for P-CAB convergence rates).

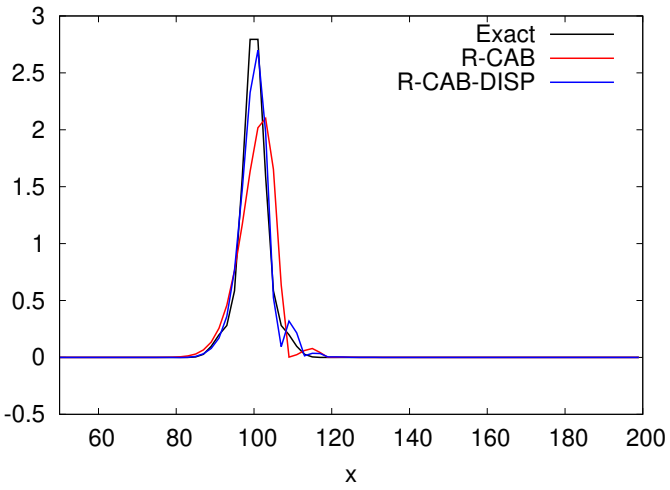

Figure 4.13: Test Case C : Comparison of R-CAB and R-CAB-DISP schemes

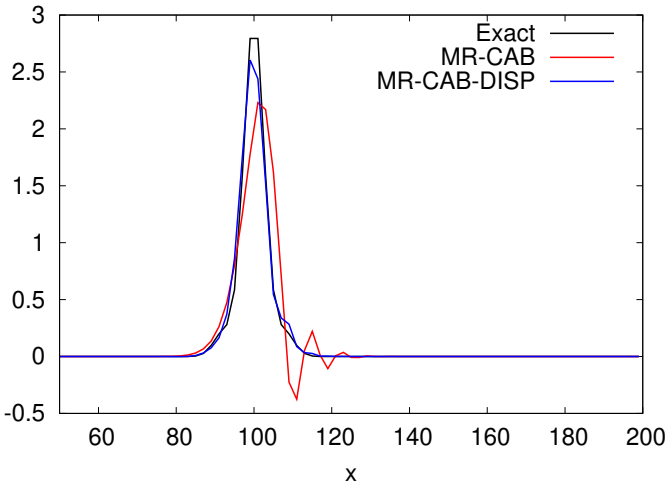

Figure 4.14: Test Case C : Comparison of MR-CAB and MR-CAB-DISP schemes

4.1.1 Choice of the relaxation parameter (ϵ)

This section presents the behaviour of the dispersion improved F-CAB, R-CAB and the MR-CAB schemes with the parameter ϵ. The test case R and Z are considered to retain the wave features. The parameter ϵ is first varied in the range of 0.1 to 0.4 and then in the range of 10^{-4} to 10^{-1}. Both the test cases are presented for CFL of 0.2 and grid sizes of 200 and 400 for test cases R and Z, respectively.

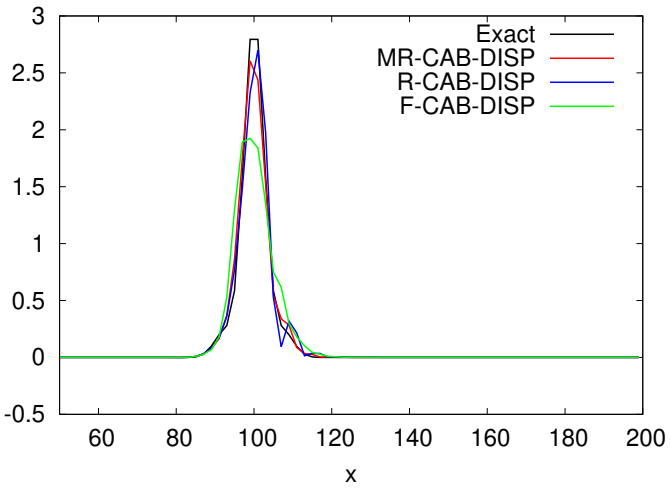

Figure 4.15: Test Case C : Comparison of F-CAB-DISP, R-CAB-DISP and MR-CAB-DISP schemes

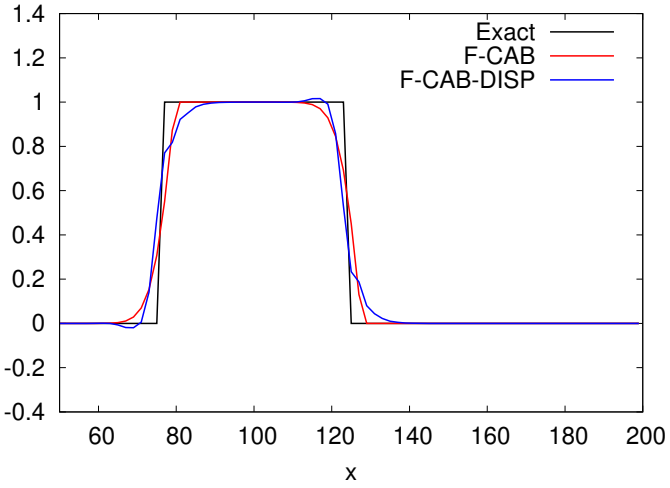

Figure 4.16: Test Case R : Comparison of F-CAB and F-CAB-DISP schemes

4.1.1.1 Test case R

The dispersion improved variants of R-CAB and MR-CAB for the test case R for varying ϵ are presented. Firstly, ϵ was varied from 0.1 to 0.4, and the Figures from 4.40a to 4.40d are presented. It can be seen that R-CAB is unaffected by varying ϵ. On the other hand, MR-CAB tends to P-CAB like behaviour for ϵ greater than 0.2.

Furthermore, ϵ is for values less than 0.1. The results are presented in Figures 4.41a to 4.41d. As expected the MR-CAB scheme reduces to F-CAB scheme

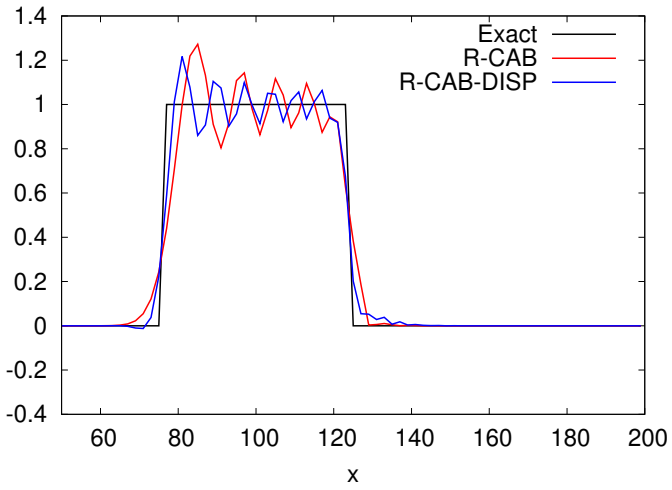

Figure 4.17: Test Case R : Comparison of R-CAB and R-CAB-DISP schemes

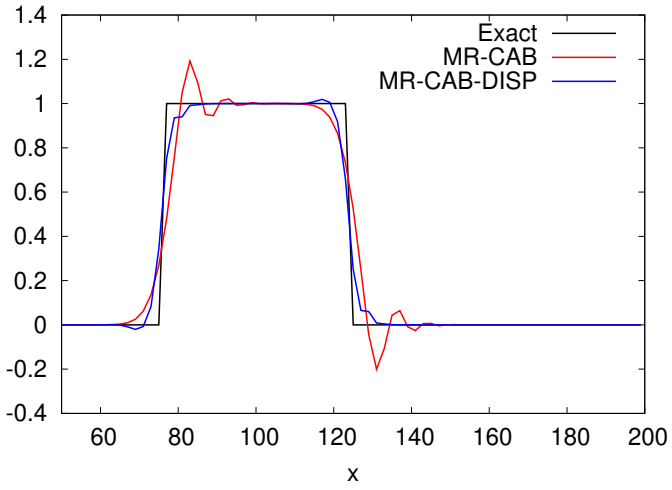

Figure 4.18: Test Case R : Comparison of MR-CAB and MR-CAB-DISP schemes

with decreasing ϵ. On the other hand, the R-CAB scheme still preserved the unwanted oscillations. As shown in Figures 4.43a to 4.43d dispersion improved R-CAB completely removes any relaxation when ϵ is 1e-3 and less (As shown in Figures 4.42a to 4.42d is the variation of ϵ from 0.05 to 0.08). Hence, to preserve the hat profile the relaxation parameter should be around 1e-3 for the dispersion improved R-CAB and 0.2 for the dispersion improved MR-CAB.

4.1.1.2 Test case Z

The dispersion improved variants of R-CAB and MR-CAB for the test case Z for varying ϵ are presented. The optimal values of ϵ to capture the hat profile for

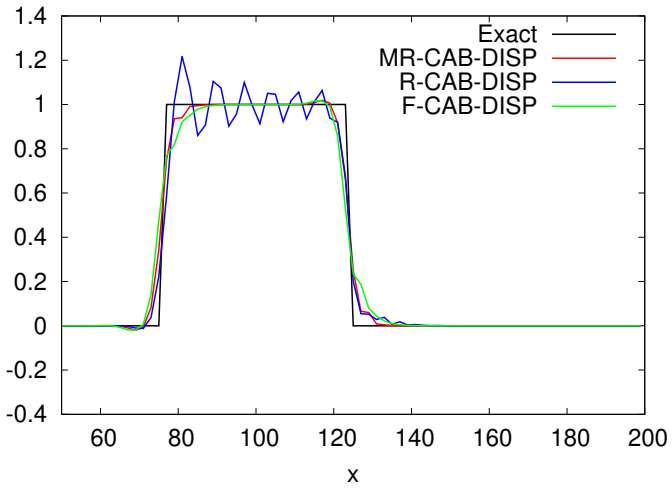

Figure 4.19: Test Case R : Comparison of F-CAB-DISP, R-CAB-DISP and MR-CAB-DISP schemes

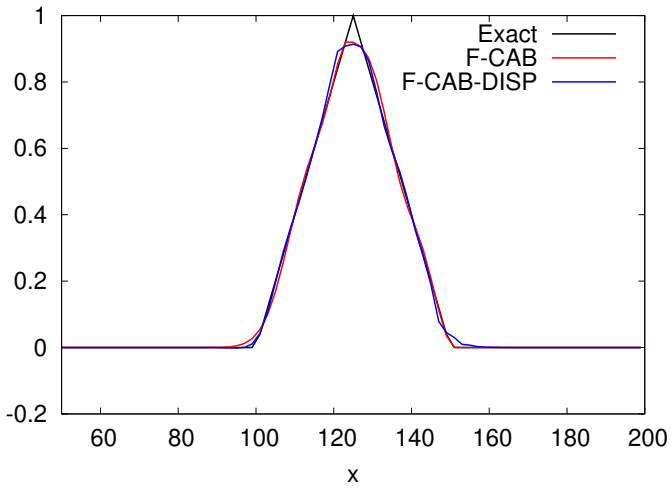

Figure 4.20: Test Case T : Comparison of F-CAB and F-CAB-DISP schemes

both the schemes is known from the test case R.

As test case Z has a hat profile superimposed by a high-frequency wave. Firstly, the high-frequency wave is shown for both the top and the bottom floor of the wave for the optimal values of ϵ for dispersion improved R-CAB (ϵ=1e-3) and MR-CAB (ϵ=0.2) schemes. They are shown in Figures 4.44a and 4.44b, for the dispersion improved R-CAB and MR-CAB scheme, respectively.

As known at these optimal values of ϵ the hat profile has been satisfactorily captured for both the schemes. Furthermore, the bottom floor of the test case is shown in Figures 4.45a and 4.45b, respectively. It is seen that the R-CAB

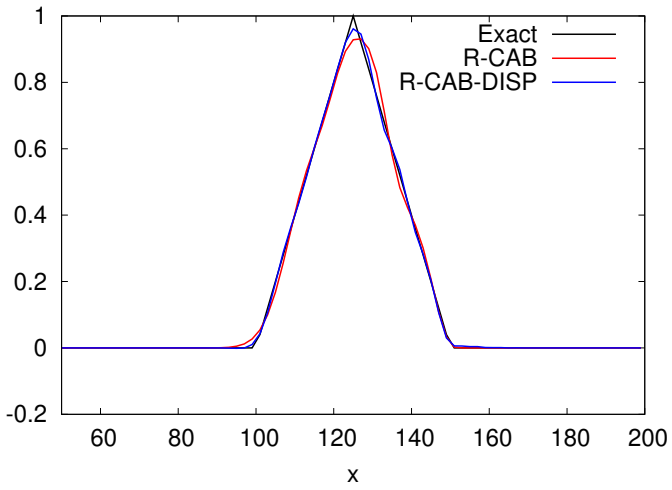

Figure 4.21: Test Case T : Comparison of R-CAB and R-CAB-DISP schemes

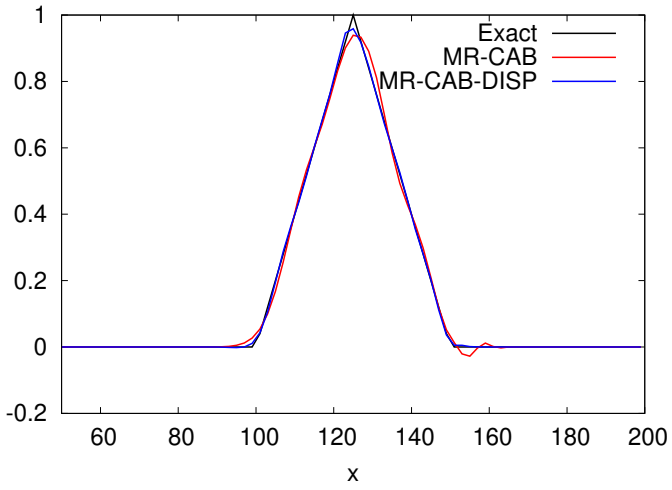

Figure 4.22: Test Case T : Comparison of MR-CAB and MR-CAB-DISP schemes

scheme fails to preserve the high-frequency wave for its optimal ϵ. However, the MR-CAB scheme captures the high-frequency wave for its optimal ϵ. It is to be noted that the R-CAB scheme captures the peaks of the high-frequency wave slightly better than MR-CAB for ϵ of 0.2. Also, the F-CAB scheme truncates the amplitude of the high-frequency wave.

From Figures 4.46a and 4.46b, also the high-frequency wave is better captured by MR-CAB scheme when compared to both the F-CAB and the R-CAB scheme.

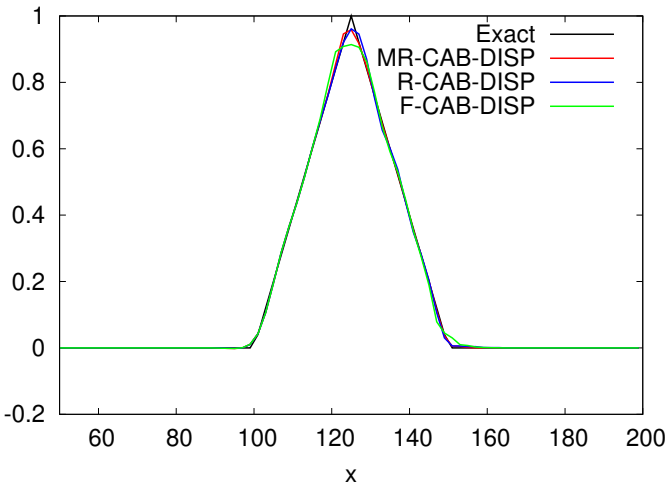

Figure 4.23: Test Case T : Comparison of F-CAB-DISP, R-CAB-DISP and MR-CAB-DISP schemes

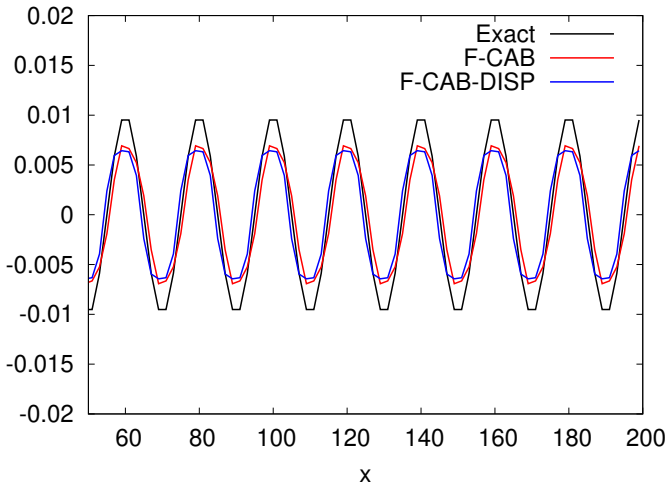

Figure 4.24: Test Case Y : Comparison of F-CAB and F-CAB-DISP schemes

4.1.2 Effect of the relaxation parameter ϵ for different amplitudes

The optimal values of ϵ obtained in the previous section for the dispersion improved R-CAB, and MR-CAB schemes are now applied to the test case Z variants. The variants are obtained by varying the amplitude of the superimposed cosine wave. The amplitude considered are 0.05 and 0.1, corresponding to 5% and 10% of the hat profile amplitude.

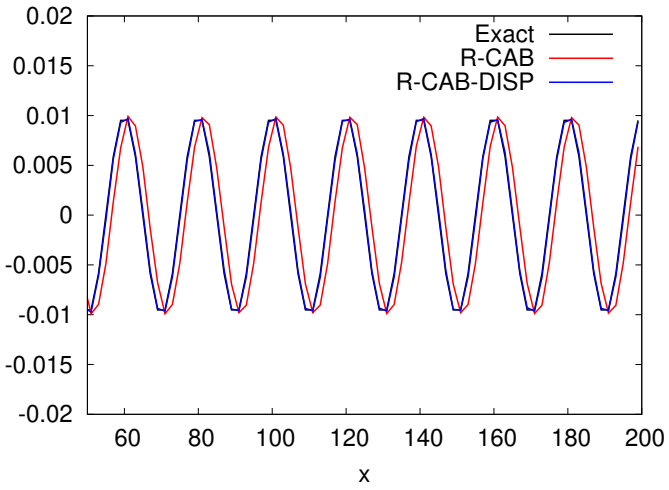

Figure 4.25: Test Case Y : Comparison of R-CAB and R-CAB-DISP schemes

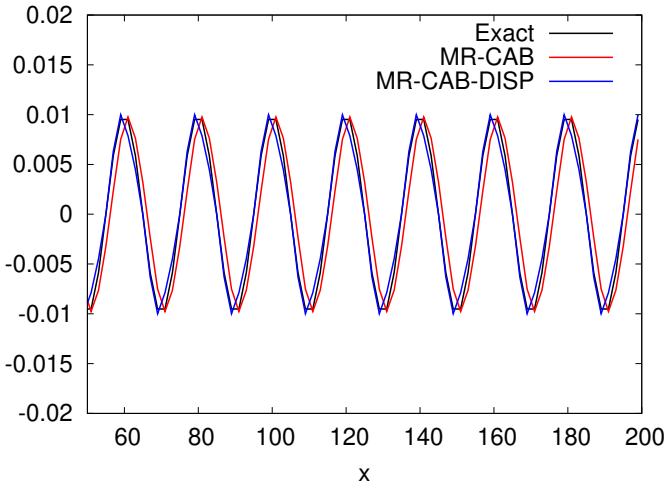

Figure 4.26: Test Case Y : Comparison of MR-CAB and MR-CAB-DISP schemes

4.1.2.1 Ampltiude 5%

The test case Z with a 5% amplitude of the high-frequency wave has been convected using the dispersion improved variants of R-CAB and MR-CAB at their respective optimal ϵ values. The results for the R-CAB with ϵ=1e-3 is shown in Figures 4.47a to 4.47c. It is seen that the R-CAB scheme is able to preserve the high-frequency wave on the top of the hat profile, whereas as expected the high-frequency wave on the bottom floor was not captured well.

However, coming to the MR-CAB scheme with its optimal ϵ value of 0.2, the Figures shown from 4.48a to 4.48c, indicate that the MR-CAB is able to capture

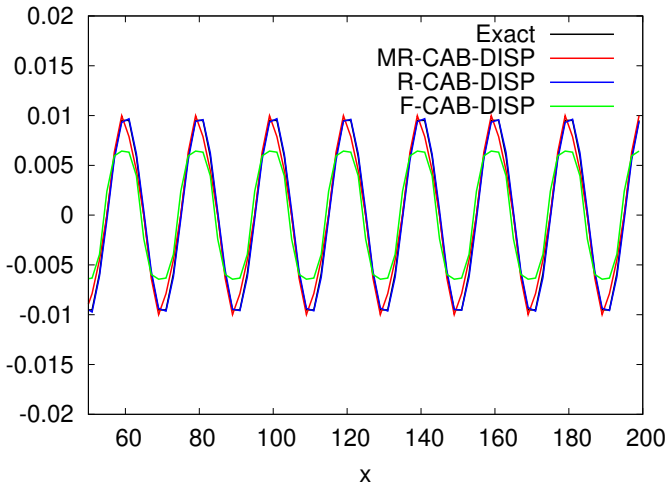

Figure 4.27: Test Case Y : Comparison of F-CAB-DISP, R-CAB-DISP and MR-CAB-DISP schemes

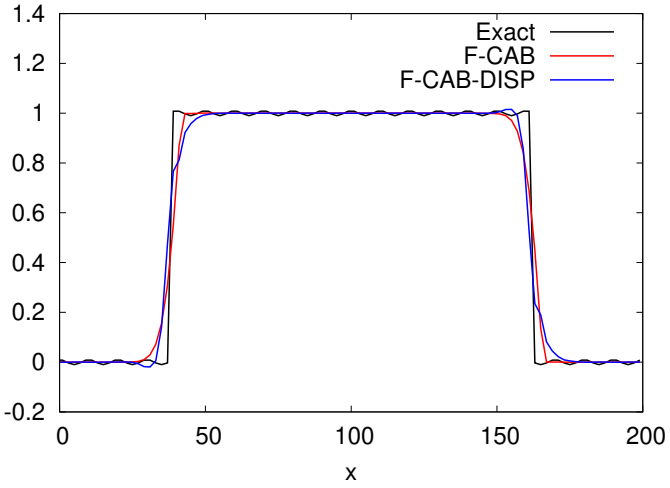

Figure 4.28: Test Case Z : Comparison of F-CAB and F-CAB-DISP schemes

well the high-frequency wave on both the top and the bottom floor.

4.1.2.2 Ampltiude 10%

The test case Z with a 10% amplitude of the high-frequency wave has been convected using the dispersion improved variants of R-CAB and MR-CAB at their respective optimal ϵ values. The results for the R-CAB with ϵ=1e-3 is shown in Figures 4.49a to 4.49c. It is seen that the R-CAB scheme is able to preserve the high-frequency wave on the top of the hat profile, whereas as expected the high-frequency wave on the bottom floor was not captured well.

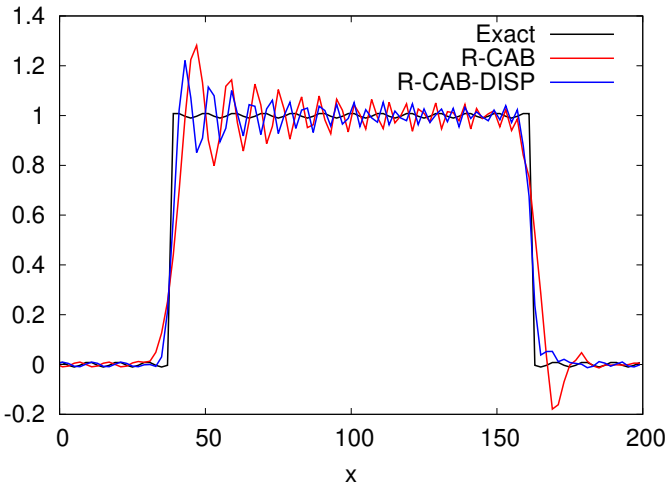

Figure 4.29: Test Case Z : Comparison of R-CAB and R-CAB-DISP schemes

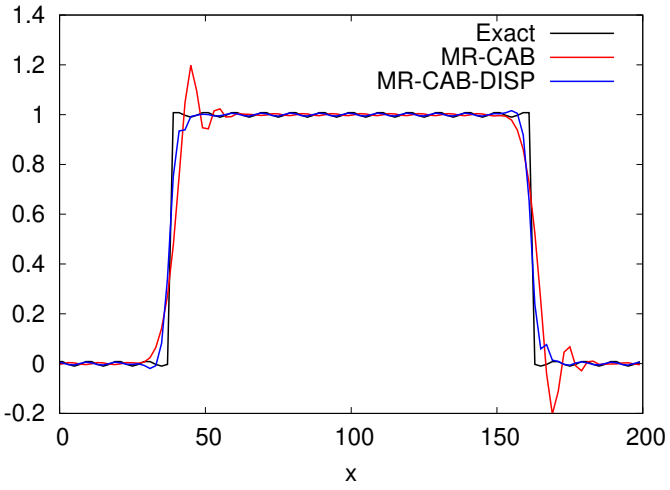

Figure 4.30: Test Case Z : Comparison of MR-CAB and MR-CAB-DISP schemes

However, coming to the MR-CAB scheme with its optimal ϵ value equal to 0.2, the Figures shown from 4.50a to 4.50c, indicate that the MR-CAB is able to capture well the high-frequency wave on both the top and the bottom floor.

4.1.3 Optimal choice of ϵ

Following the previous discussion, the optimal relaxation parameter for the modified relaxation CABARET scheme (MR-CAB) with dispersion improvement was found to be equal to 0.2. Using this two more test cases are used

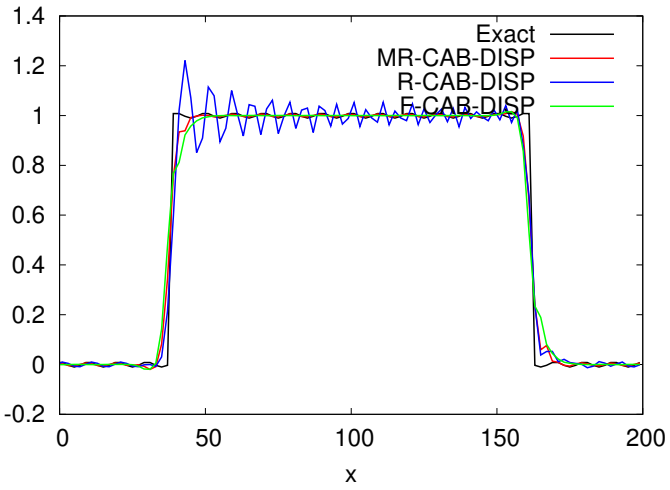

Figure 4.31: Test Case Z : Comparison of F-CAB-DISP, R-CAB-DISP and MR-CAB-DISP schemes

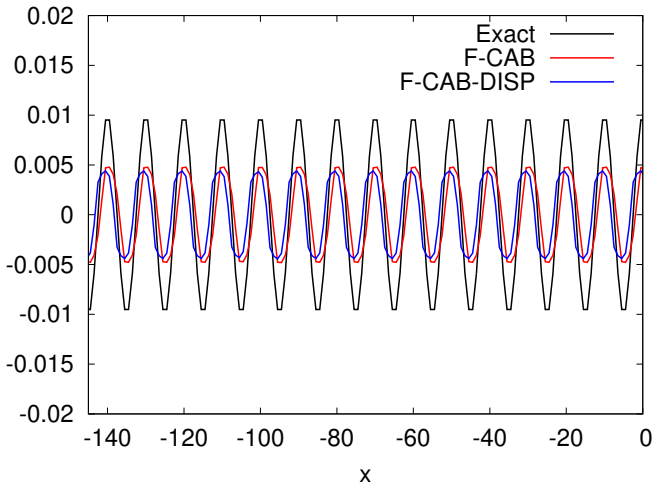

Figure 4.32: Test Case Z near floor: Comparison of F-CAB and F-CAB-DISP schemes

to compare the P-CAB, the F-CAB, the MR-CAB-DISP scheme with the DRP scheme of Tam and Webb (1993b), to demonstrate the improvement in the solution.

The first test case (denoted by BB) given by equation (4.7) is a wave packet consisting of a sine wave modulated by a Gaussian profile (Bogey and Bailly, 2004). The periodic boundary conditions are applied at the boundaries of the domain from 0 to 2 units in space, as shown in Figure 4.51a, and the control time was taken to be 100. The second test case (denoted by JS) given by equation (4.8), is a multi-shape profile of Jiang and Shu (1996) consisting of a Gaussian, a square

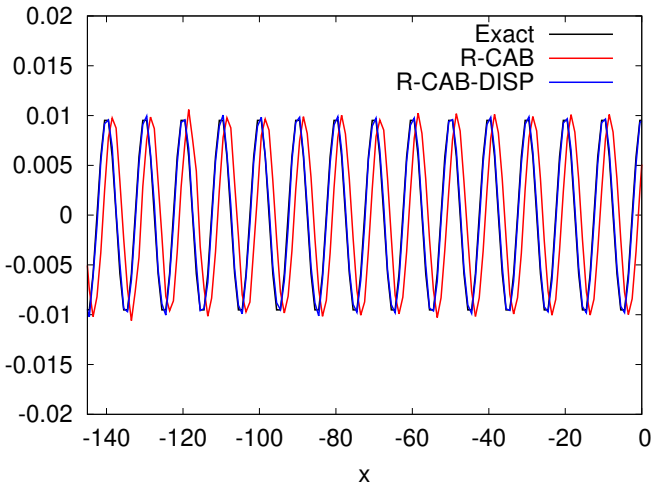

Figure 4.33: Test Case Z near floor: Comparison of R-CAB and R-CAB-DISP schemes

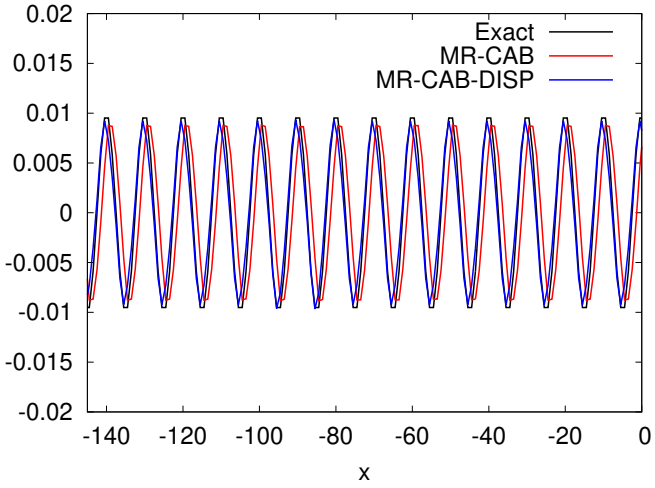

Figure 4.34: Test Case Z near floor: Comparison of MR-CAB and MR-CAB-DISP schemes

wave, a triangle wave, and a half-ellipse, respectively in equal intervals on the grid as shown in Figure 4.51b. Also, the domain for this test case was chosen to be -1 to 1 and the profile was convected for 8 times the length of the profile.

$$u(x,t=0) = \begin{cases} sin\left(48\pi(\frac{x}{L}-\frac{1}{4})\right) e^{-log(2)(\frac{32}{3}(\frac{x}{L}-\frac{1}{4}))^2} & 0 \le x \le \frac{L}{2} \\ 0 & \frac{L}{2} \le x \le L \end{cases} \tag{4.7}$$

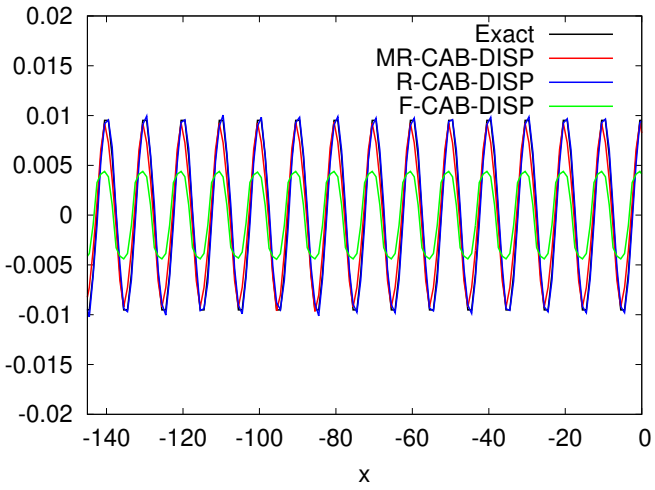

Figure 4.35: Test Case Z near floor: Comparison of F-CAB-DISP, R-CAB-DISP and MR-CAB-DISP schemes

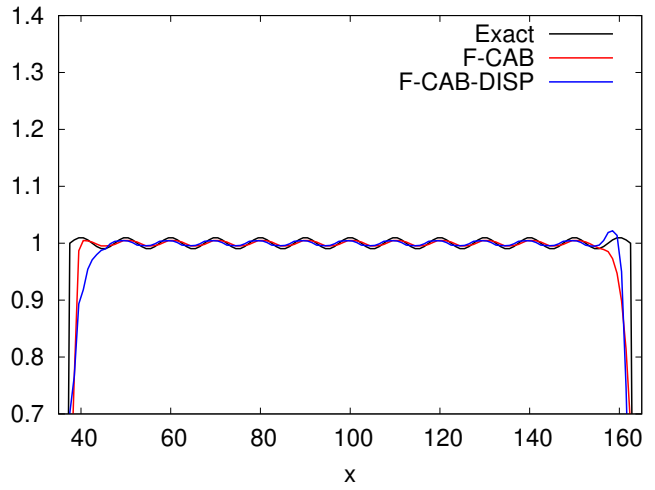

Figure 4.36: Test Case Z at top: Comparison of F-CAB and F-CAB-DISP schemes

$$u(x,t=0)=\begin{cases}\frac{1}{6}\left(e^{-\beta(x/L+0.695)}+e^{-\beta(x/L+0.705)}+4e^{-\beta(x/L+0.7)}\right) & -0.8\le x\le -0.6\\ 1 & -0.4\le x\le -0.2\\ 1-|10(x/L-0.1)| & 0\le x\le 0.2\\ \frac{1}{6}\left(\psi(x/L,0.495)+\psi(x/L,0.505)+4\psi(x/L,0.5)\right) & 0.4\le x\le 0.6\\ 0 & \text{otherwise}\end{cases} \tag{4.8}$$

with

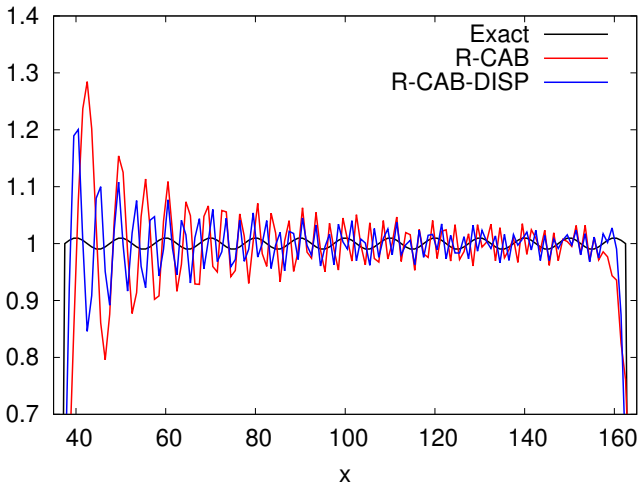

Figure 4.37: Test Case Z at top: Comparison of R-CAB and R-CAB-DISP schemes

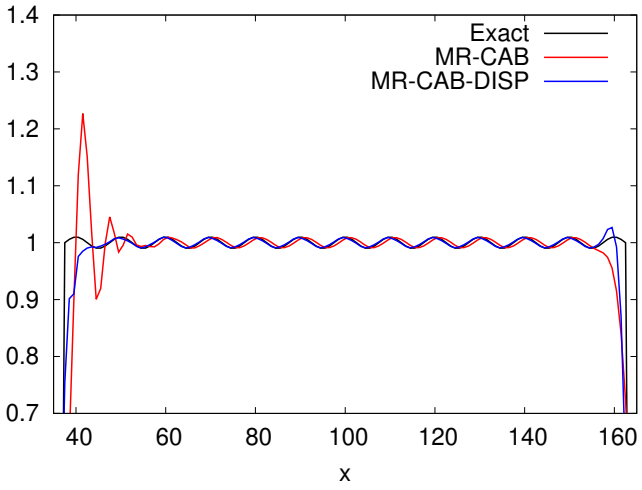

Figure 4.38: Test Case Z at top: Comparison of MR-CAB and MR-CAB-DISP schemes

$$\beta = \frac{log(2)}{9\times 10^{-4}}, \quad \psi(x/L, x_0/L) = \sqrt{max(1-100(x/L-x_0/L)^2, 0)} \tag{4.9}$$

For the test case BB, the solution was obtained for a mesh of 200 cells corresponding to 8 PPW for the sine wave and a CFL number of 0.2. Firstly, in Figure 4.52a the convected profiles for the MR-CAB-DISP scheme (for $\epsilon = 0.2$), the F-CAB scheme, and the P-CAB scheme are shown. It can be seen that the MR-CAB-DISP recovers both the amplitude and the correct phase satisfactorily compared to the exact solution, particularly for the Gaussian profile. As expected the non-monotone P-CAB scheme resulted in oscillations in the solution.

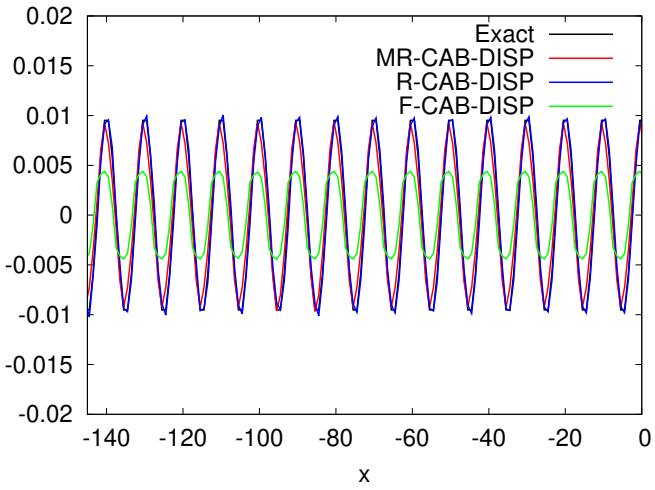

Figure 4.39: Test Case Z at top: Comparison of F-CAB-DISP, R-CAB-DISP and MR-CAB-DISP schemes

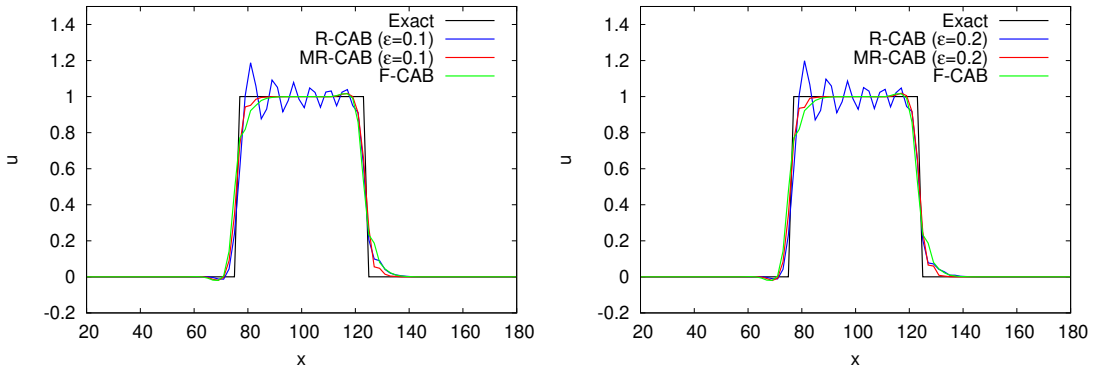

(a) $\epsilon = 0.1$

(b) $\epsilon = 0.2$

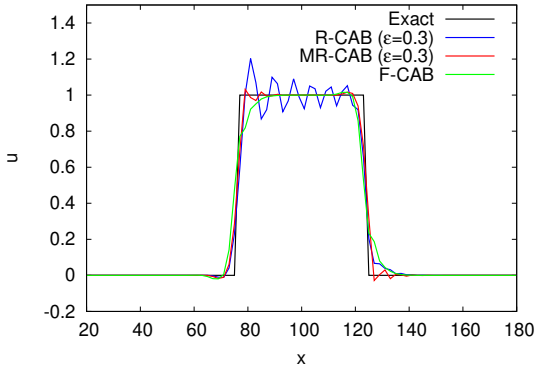

(c) $\epsilon = 0.3$

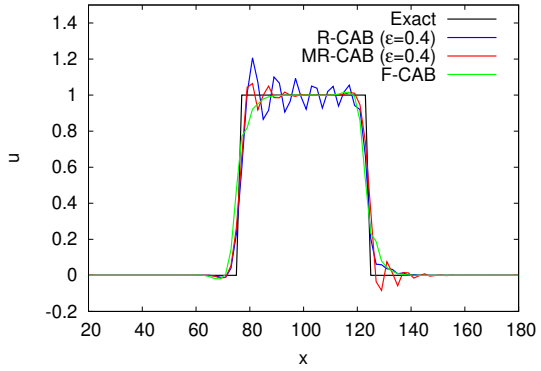

(d) $\epsilon = 0.4$

Figure 4.40: Effect of ϵ variation on the dispersion improved F-CAB, R-CAB and MR-CAB schemes for test case R

Also, the MR-CAB-DISP scheme preserved the sharp peaks of the Gaussian and the triangular profiles. Secondly, the best CABARET variant MR-CAB scheme

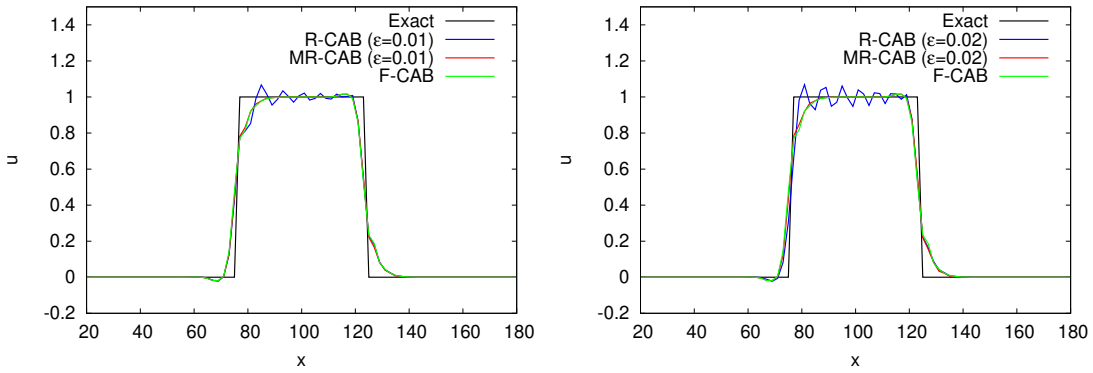

(a) $\epsilon = 0.01$

(b) $\epsilon = 0.02$

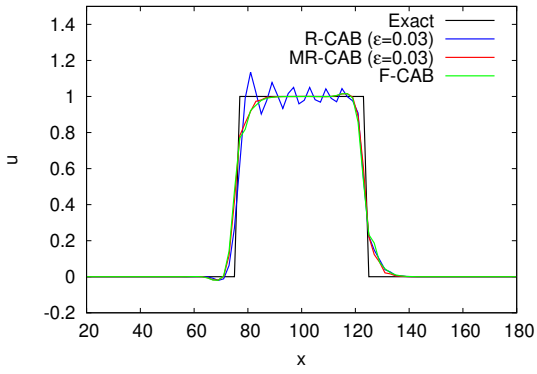

(c) $\epsilon = 0.03$

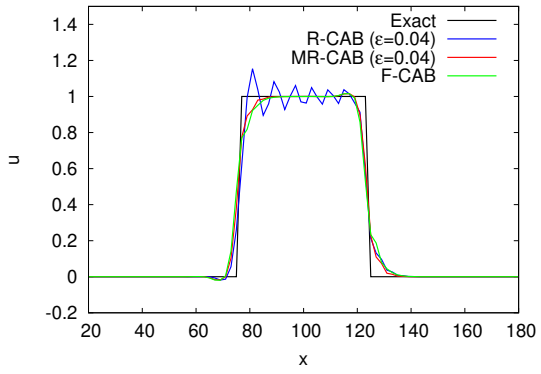

(d) $\epsilon = 0.04$

Figure 4.41: Effect of ϵ variation on the dispersion improved F-CAB, R-CAB and MR-CAB schemes for test case R

is compared to the DRP scheme and shows an impressive recovery of the phase and amplitude of the wave packet, as shown in Figure 4.52b.

For the test case JS, the solution is shown for the same 200 cells for all schemes, and the CFL number was taken to be 0.2. First, among the CABARET variants shown in Figures 4.53a, we see that the P-CAB scheme fails to capture the non-linearities in the wave, whereas, MR-CAB-DISP retains the important flow features compared to the F-CAB scheme. Secondly, in Figure 4.53b the MR-CAB-DISP scheme was observed to be superior to the DRP scheme which produced oscillations in the domain apart from failing to recover the phase.

For the test case BB impressively the MR-CAB-DISP (see table A.12) reaches the formal OOA of 2, compared to the DRP scheme (see table A.1) reaching for an accuracy of 2.3. Also, the F-CAB (see table A.3) records an OOA of 1.86 and

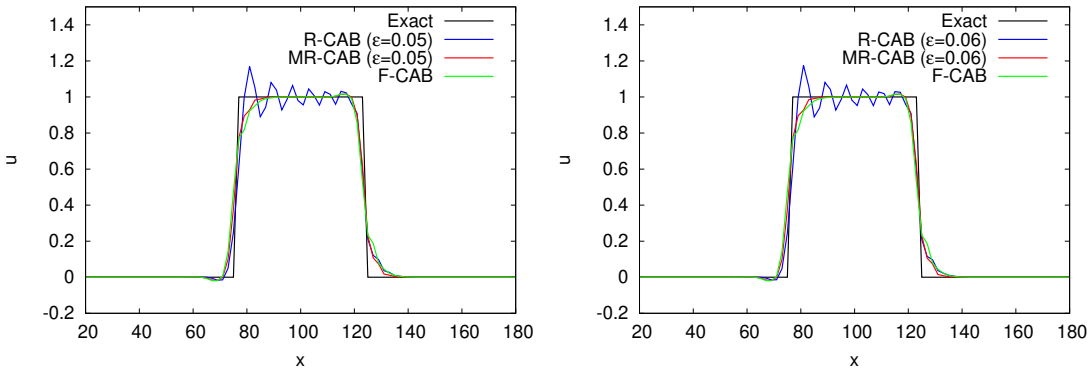

(a) $\epsilon = 0.05$

(b) $\epsilon = 0.06$

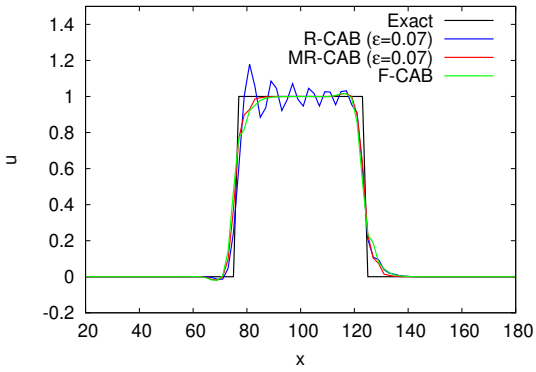

(c) $\epsilon = 0.07$

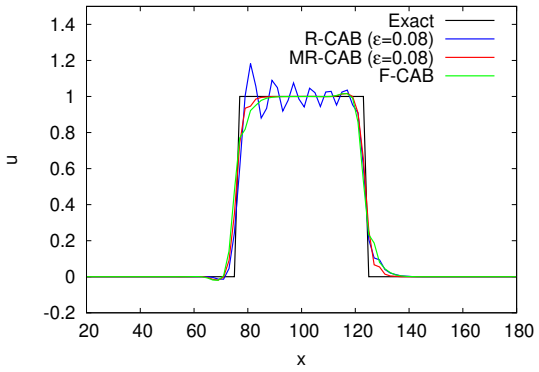

(d) $\epsilon = 0.08$

Figure 4.42: Effect of ϵ variation on the dispersion improved F-CAB, R-CAB and MR-CAB schemes for test case R

P-CAB (see table A.21) retains the formal OOA of 2.0.

For the test case JS the DRP scheme (see table A.2) due to the oscillations in the solution has not notable reduction in error whereas, the MR-CAB-DISP scheme (see table A.13) has an OOA of 0.8. And F-CAB scheme (see table A.4) has an accuracy of 0.77, with the P-CAB (see table A.22) reaching an accuracy of approximately 0.5. This shows that the MR-CAB-DISP scheme is able to maintain the convergence rates for the different initial profiles, better than other CABARET variants.

In summary, the second-order accurate MR-CAB-DISP was shown to be effective than the currently existing CABARET variants and the high-order DRP scheme. Both the recovery of the amplitude and phase for the profiles were shown to be significantly improved.

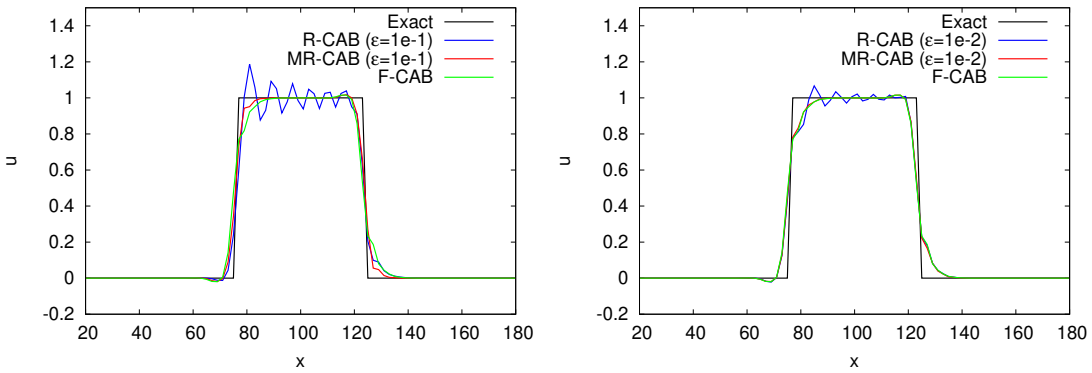

(a) ϵ = 1e-1

(b) ϵ = 1e-2

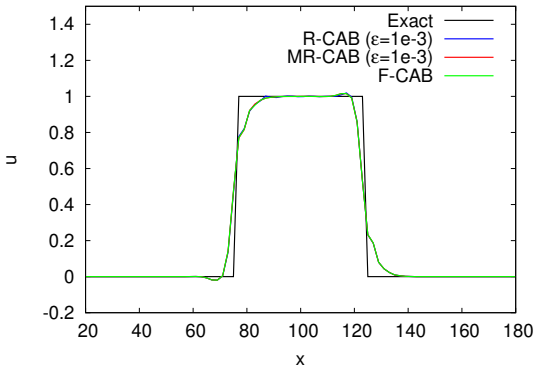

(c) ϵ = 1e-3

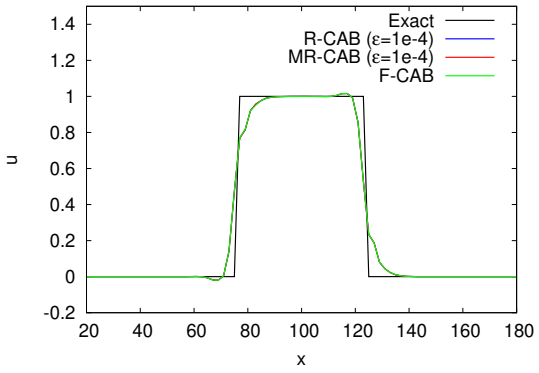

(d) ϵ = 1e-4

Figure 4.43: Effect of ϵ variation on the dispersion improved F-CAB, R-CAB and MR-CAB schemes for test case R

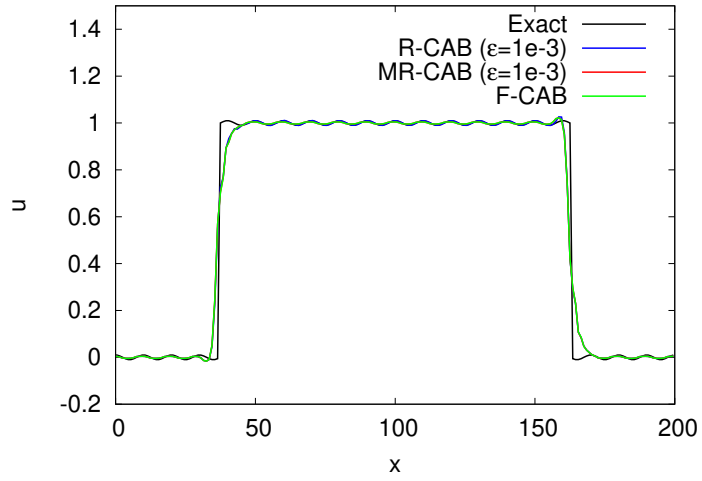

(a) Dispersion improved R-CAB scheme ϵ = 1e-3

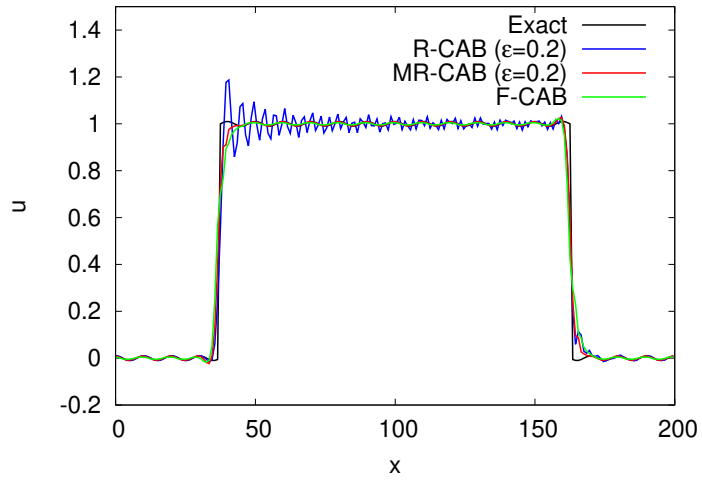

(b) Dispersion improved MR-CAB scheme ϵ = 0.2

Figure 4.44: Effect of ϵ variation on the dispersion improved F-CAB, R-CAB and MR-CAB schemes for test case Z

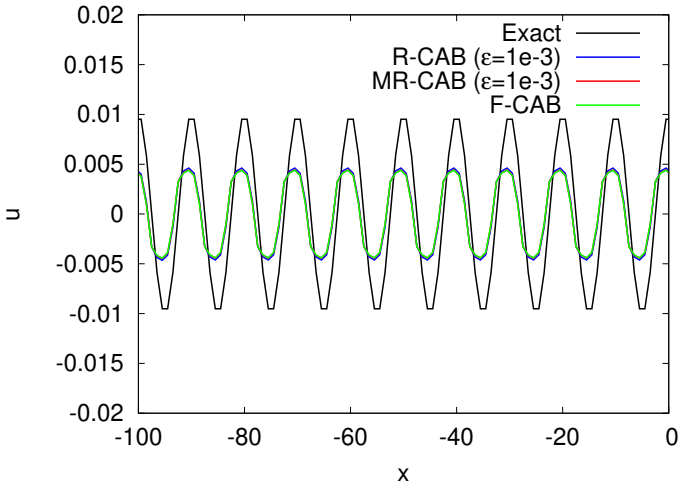

(a) Dispersion improved R-CAB scheme ϵ = 1e-3

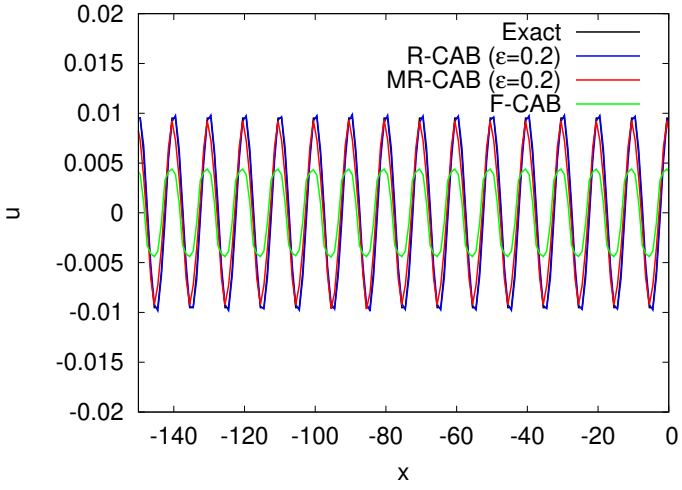

(b) Dispersion improved MR-CAB scheme ϵ = 0.2

Figure 4.45: Effect of ϵ variation on the dispersion improved F-CAB, R-CAB and MR-CAB schemes for test case Z at the bottom floor

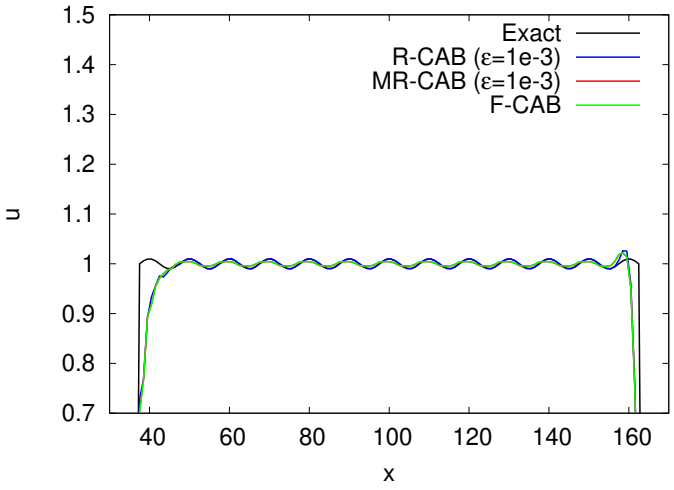

(a) Dispersion improved R-CAB scheme ϵ = 1e-3

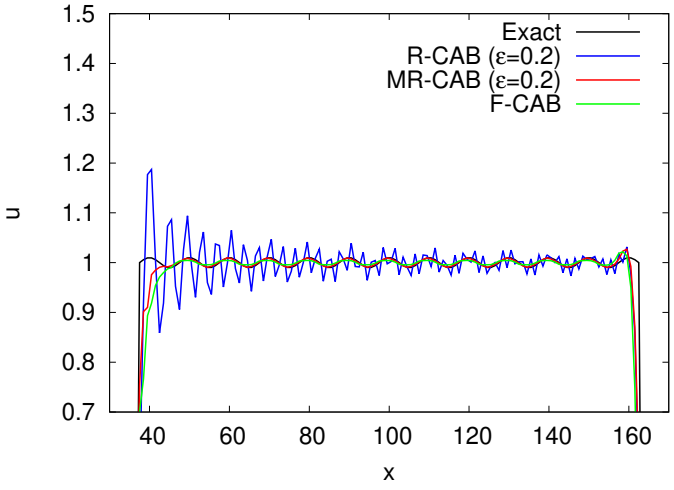

(b) Dispersion improved MR-CAB scheme ϵ = 0.2

Figure 4.46: Effect of ϵ variation on the dispersion improved F-CAB, R-CAB and MR-CAB schemes for test case Z on the top floor

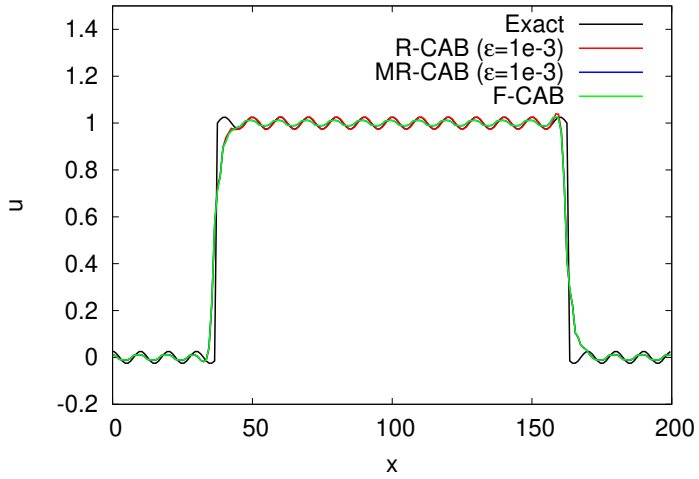

(a) Full view of the test case Z

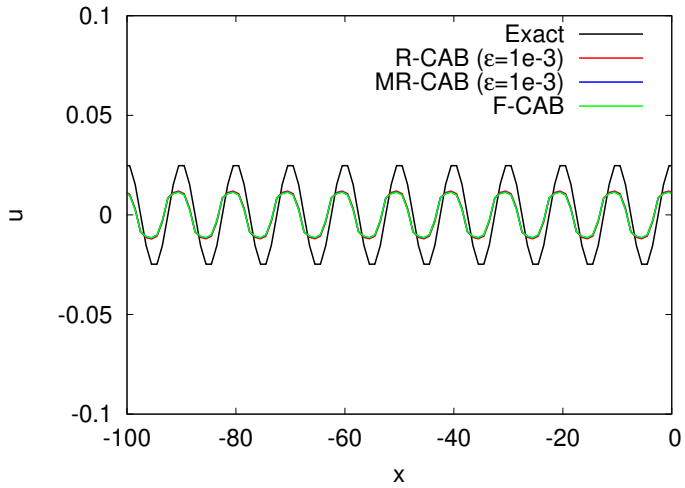

(b) Bottom floor of the test case Z

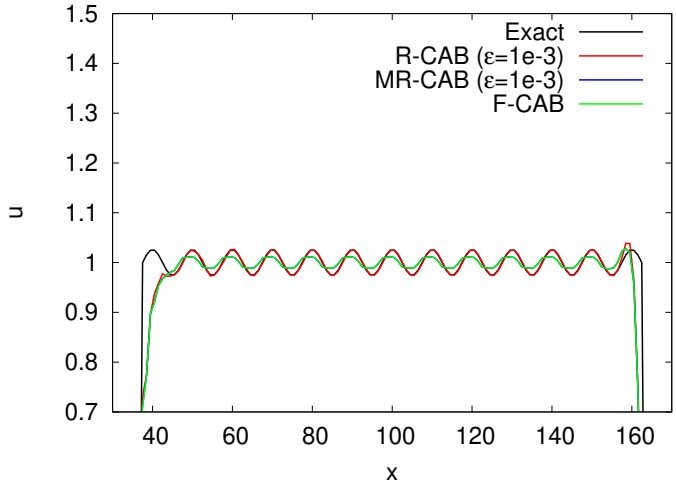

(c) Top floor of the test case Z

Figure 4.47: Dispersion improved F-CAB, R-CAB and MR-CAB schemes for Z at 5% amplitude and at optimal ϵ=1e-3 of R-CAB

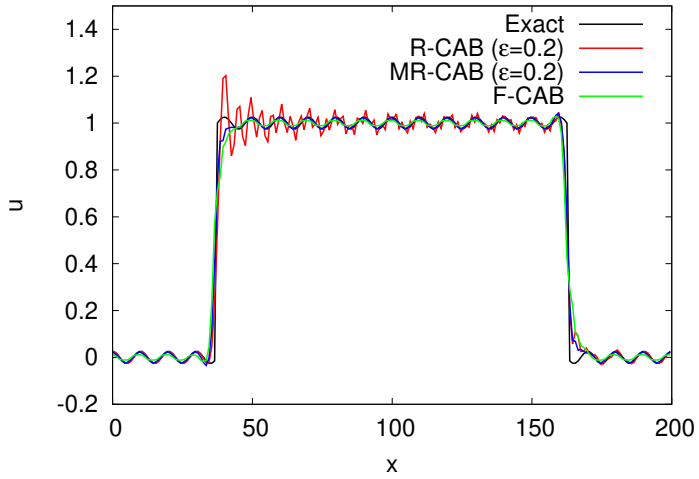

(a) Full view of the test case Z

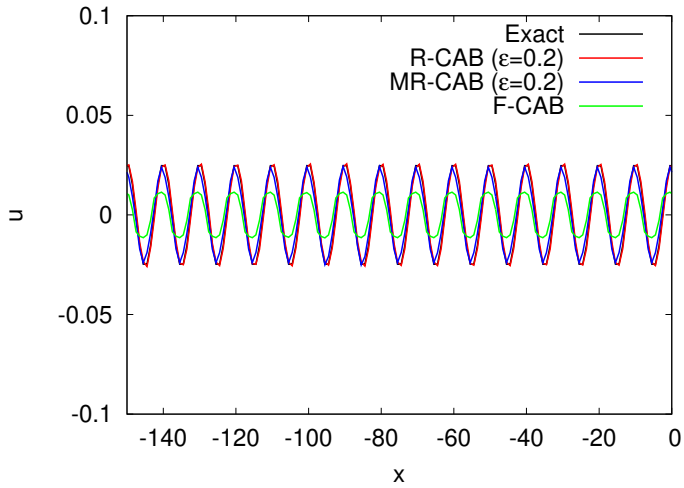

(b) Bottom floor of the test case Z

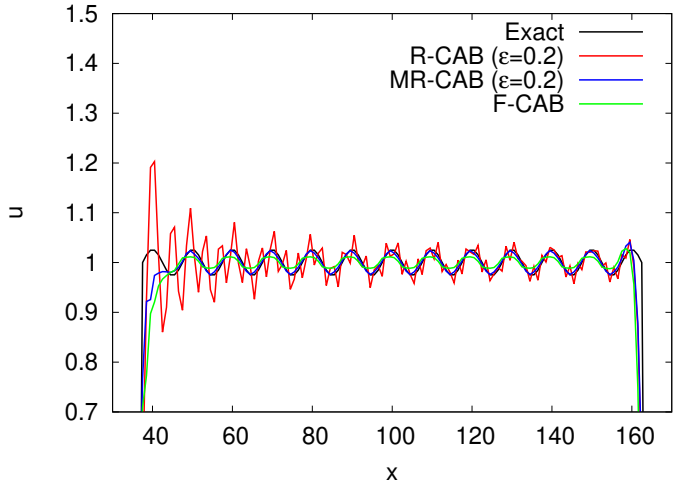

(c) Top floor of the test case Z

Figure 4.48: Dispersion improved F-CAB, R-CAB and MR-CAB schemes for Z at 5% amplitude and at optimal ϵ=0.2 of MR-CAB

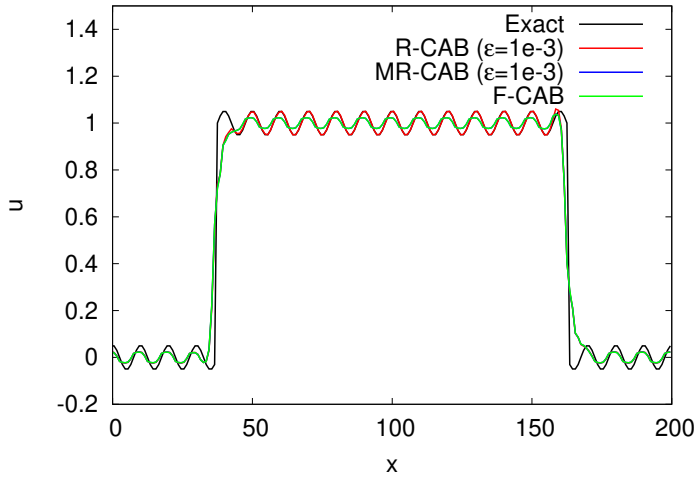

(a) Full view of the test case Z

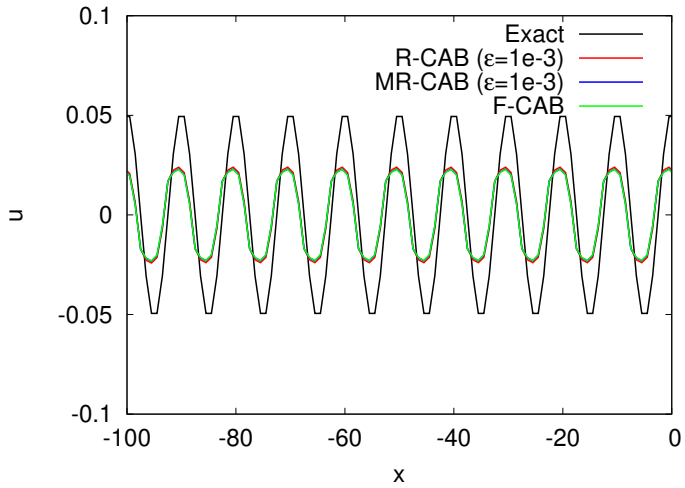

(b) Bottom floor of the test case Z

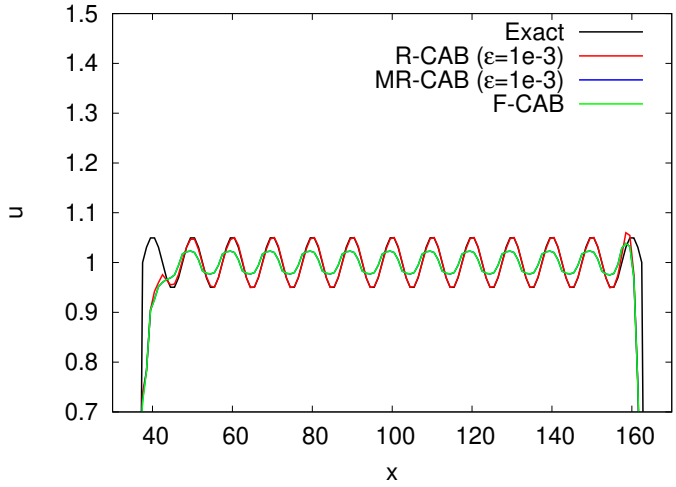

(c) Top floor of the test case Z

Figure 4.49: Dispersion improved F-CAB, R-CAB and MR-CAB schemes for Z at 10% amplitude and at optimal ϵ=1e-3 of R-CAB

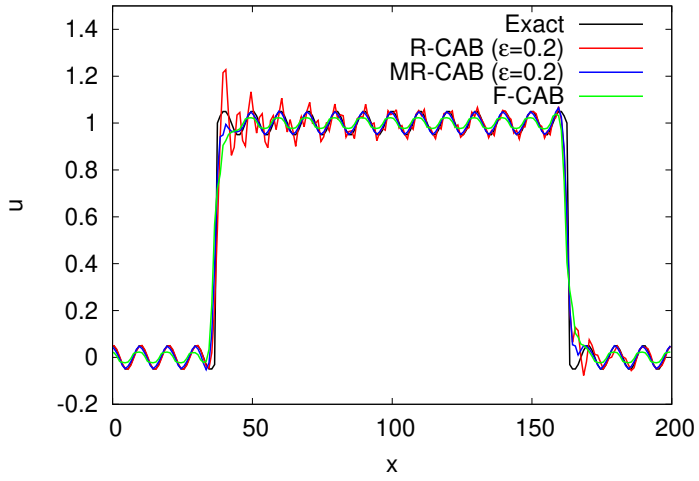

(a) Full view of the test case Z

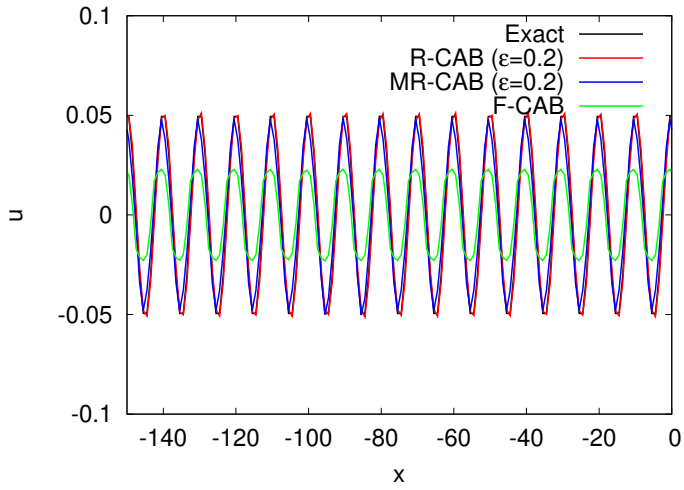

(b) Bottom floor of the test case Z

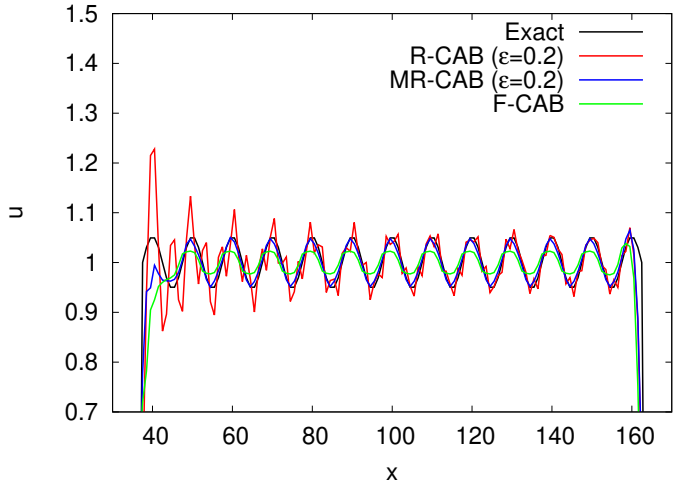

(c) Top floor of the test case Z

Figure 4.50: Dispersion improved F-CAB, R-CAB and MR-CAB schemes for Z at 10% amplitude and at optimal ϵ=0.2 of MR-CAB

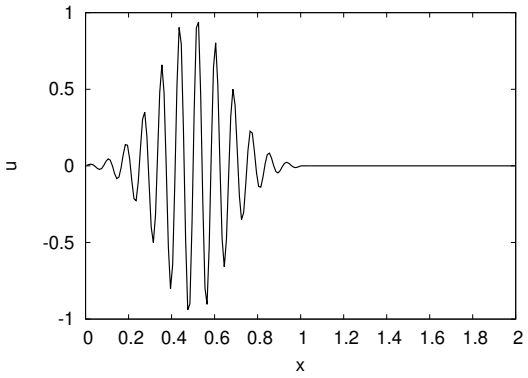

(a) Initial profile of test case BB

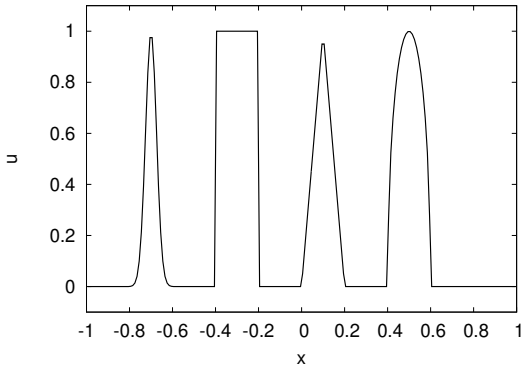

(b) Initial profile of test case JS

Figure 4.51: 1D convection test case initial conditions

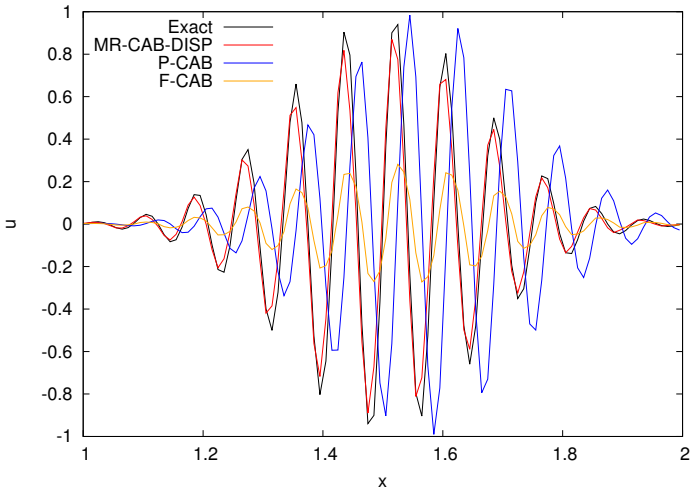

(a) Comparison of the CABARET variants

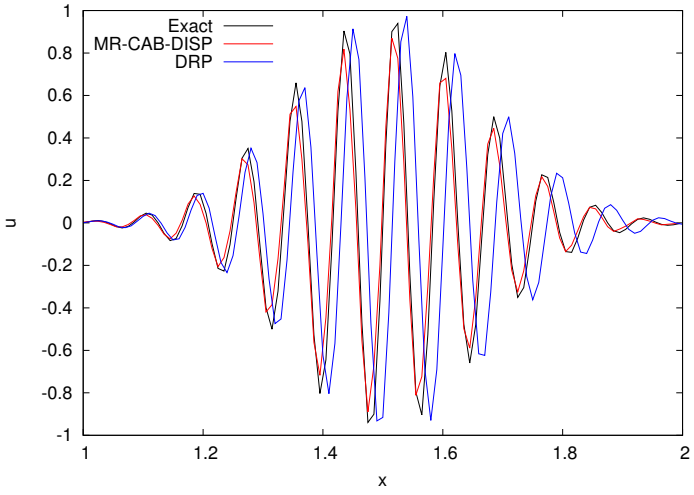

(b) Comparison of MR-CAB-DISP and DRP schemes

Figure 4.52: Comparison of the MR-CAB-DISP scheme with other CABARET variants and the DRP scheme for test case BB

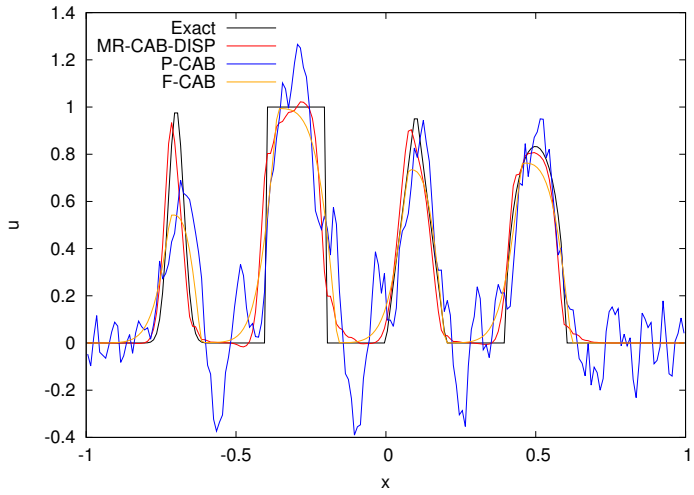

(a) Comparison of the CABARET variants

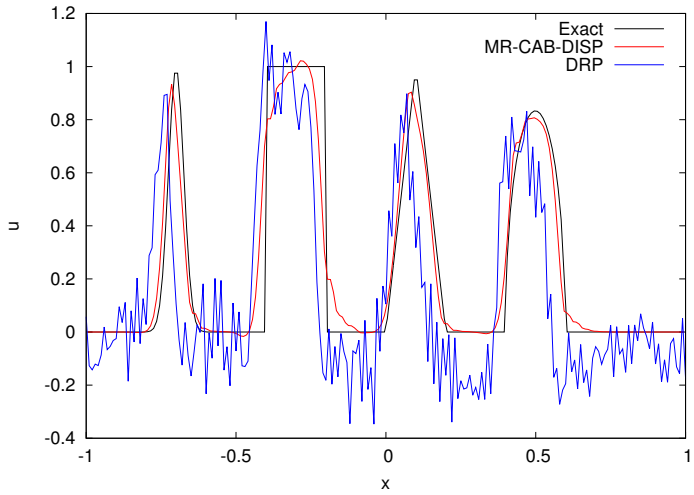

(b) Comparison of MR-CAB-DISP and DRP schemes

Figure 4.53: Comparison of the MR-CAB-DISP scheme with other CABARET variants and the DRP scheme for test case JS

4.2 Isothermal Gas Dynamics

The three-dimensional Euler equations given by equations (2.90) can be linearised to obtain the acoustic wave equation in three-dimensions (Rienstra and Hirschberg, 2004). Let us consider a linearisation based on a mean flow (denoted by subscript 0) and its corresponding fluctuating components (denoted by prime) as

$$(\rho, u, v, w, p) = (\rho_0 + \rho', u_0 + u', v', w', p_0 + p') \tag{4.10}$$

resulting in the acoustic wave equation

$$\left(\frac{\partial}{\partial t} + u_0 \frac{\partial}{\partial x}\right)^2 \rho' - c_0^2 \left(\frac{\partial^2 \rho'}{\partial x^2} + \frac{\partial^2 \rho'}{\partial y^2} + \frac{\partial^2 \rho'}{\partial z^2}\right) = 0 \tag{4.11}$$

where $c_0 = \sqrt{\frac{\gamma p_0}{\rho_0}}$ is the speed of sound and the rest of the variables retain the same definitions as described for the Euler equations. The equation (4.11) is now applied to a box domain of length L_x, L_y and L_z in the x, y, and z-directions, respectively. In the x-direction one of the faces is chosen to be inlet corresponding to an incoming pressure wave, and the other as outlet corresponding to a characteristic non-reflecting boundary. And the domain is taken to be periodic in the rest of the directions by adjusting the dimensions of the domain as $L_y = \frac{2\pi}{k_y}$ and $L_z = \frac{2\pi}{k_z}$. The incoming wave from the inlet is propagated at a speed of 0.5 Mach, with ($M = \frac{u_0}{c_0}$). The equation (4.11) allows periodic wave solutions in the form of

$$\rho' = \epsilon_0 \rho_0 e^{i(\omega t - k_x x - k_y y - k_z z)} \tag{4.12}$$

where, ϵ_0 is the amplitude of the perturbation such that $0 < \epsilon_0 \ll 1$,and ω is the specified wave frequency and k_x, k_y, k_z denote the wave numbers in x,y, and z-directions, respectively. Also, the wave angle between the front normal (y)

and the flow direction (x) is given by $\theta = arctan\left(\frac{k_y}{k_x}\right)$. The flow angle between the y and z directions can be seen as a collective wave number $k_{yz} = k_y\hat{e_y} + k_z\hat{e_z}$, whose magnitude is $k_{yz}^2 = k_y^2 + k_z^2$ and the angle between the components is given by $\alpha = arctan\left(\frac{k_z}{k_y}\right)$.

On substituting the wave solution from equation (4.12) into the acoustic wave equation given by equation (4.11), the dispersion relation is obtained as

$$\omega^2 - 2k_x u_0 \omega + k_x^2 u_0^2 - c_0^2(k_x^2 + k_y^2 + k_z^2) = 0 \tag{4.13}$$

which can be simplified to a quadratic equation in k_x as

$$k_x^2 - \frac{2M}{M^2-1}\frac{\omega}{c_0} + \frac{\left(\frac{\omega}{c_0}\right)^2 - k_y^2 - k_z^2}{M^2-1} = 0 \tag{4.14}$$

Solving for the wave numbers we obtain

$$k_x = \frac{\omega}{c_0}\frac{\left(\sqrt{1-\eta} - M\right)}{1-M^2}, \quad k_y = \frac{\omega}{c_0}\frac{\sqrt{\eta}}{\sqrt{1-M^2}}, \quad k_z = \frac{\omega}{c_0}\frac{\sqrt{\eta}}{\sqrt{1-M^2}} \tag{4.15}$$

where $\eta = tan(\theta)$. With this the expressions for the flow variables can be sought as follows. Since, the fluctuating pressure and the fluctuating density are related by $p' = c_0^2\rho'$ and the mean pressure to the mean density as $c_0^2 = \frac{\gamma p_0}{\rho_0}$, one can find pressure p as

$$p = p_0 + p' = p_0 + c_0^2 p' = \frac{c_0^2\rho_0}{\gamma} + c_0^2\rho_0\epsilon_0 e^{i\left(\omega t - k_x x - k_y y - k_z z\right)} \tag{4.16}$$

resulting in

$$p = \frac{c_0^2\rho_0}{\gamma}\left[1 + \gamma\epsilon_0 e^{i\left(\omega t - k_x x - k_y y - k_z z\right)}\right] \tag{4.17}$$

To find the expression for u, the x-momentum equation given by and the

expression for p'

$$\frac{\partial u'}{\partial t} + u_0 \frac{\partial u'}{\partial x} = -\frac{1}{\rho_0} \frac{\partial p'}{\partial x} \tag{4.18}$$

which gives the final expression for u as

$$u = u_0 \left[1 + \frac{k_x c_0^2 \epsilon_0}{u_0(\omega - k_x u_0)} e^{i(\omega t - k_x x - k_y y - k_z z)} \right] \tag{4.19}$$

Similarly, the expression for v can be obtained by using the y-momentum equation as

$$\frac{\partial v'}{\partial t} = -\frac{1}{\rho_0} \frac{\partial p'}{\partial y} \tag{4.20}$$

and on simplification gives

$$v = \frac{k_y c_0^2 \epsilon_0}{\omega} e^{i(\omega t - k_x x - k_y y - k_z z)} \tag{4.21}$$

The expression for w can be found similar to v as

$$w = \frac{k_z c_0^2 \epsilon_0}{\omega} e^{i(\omega t - k_x x - k_y y - k_z z)} \tag{4.22}$$

The following sections describe the performance of different CABARET variants for the one-, two- and three-dimensional solutions for the acoustic wave equation.

4.2.1 Linear wave propagation

The general three-dimensional solution obtained in equations (4.17), (4.19), (4.21), and (4.22) for the incoming pressure wave in equation (4.12) are cus-

tomised to obtain the relevant solutions in one-, two- and three-dimensions. The linear wave propagation is achieved by using a small amplitude of $\epsilon_0 = 10^{-5}$ for the incoming wave and is evaluated for different wave angles θ and α on both uniform and non-uniform grids. The non-uniform grid is generated as a function of the square of the cell thickness and the distance from the centre of the domain.

4.2.1.1 1D Inlet wave

The first problem considered is an incoming planar wave propagating parallel to the mean flow, i.e., in the x-direction. Hence, implying zero wave angles, both $\theta = 0$ and $\alpha = 0$. The solutions are obtained on a uniform grid and non-uniform grids for 200 cells and CFL of 0.1 and CFL of 0.8, respectively. For the non-uniform grids, the PPW varies 40 at the centre of the domain to 6 near the outlet and inlet boundaries. The MR-CAB scheme with and without dispersion improvement and the standard CABARET (F-CAB) are compared. The relaxation parameter was taken as 0.2 for these test cases.

Figures 4.54 to 4.56 show the perturbation density captured by CABARET variants on uniform grids for CFL of 0.1. Firstly, the F-CAB scheme dissipates the wave while losing the phase of the incoming wave as seen in Figure 4.54. Secondly, the modified relaxation CABARET (MR-CAB) preserves the amplitude of the wave it maintains similar phase error as the F-CAB scheme, as shown in Figure 4.55. Finally, the MR-CAB with dispersion improvement (MR-CAB-DISP) preserves well both the amplitude and phase of the perturbation. This is seen for even non-uniform grids with approximately same CFL for varying PPW for the F-CAB, MR-CAB and the MR-CAB-DISP schemes in Figures 4.57, 4.58 and 4.59, respectively.

For higher CFL numbers the standard CABARET scheme is less dispersive, and this is shown in Figure 4.60 for the same parameters as the smaller CFL test case. Both the F-CAB and MR-CAB is shown in Figures 4.60 and 4.61, preserve

well the amplitude, but a small error in the phase of the wave can be observed. The MR-CAB-DISP scheme preserves even the phase of the wave very well as shown in Figure 4.62. For non-uniform grids, the dispersion error crops up due to the low PPW near the boundaries for the F-CAB scheme, and a loss in amplitude is seen in Figure 4.63. The MR-CAB scheme recovers the amplitude as shown in Figure 4.64, while losing the phase of the wave. As in the case of uniform grids for lower CFL, the MR-CAB-DISP scheme preserves both the amplitude and the phase on a non-uniform grid for CFL of 0.8 satisfactorily, as shown in Figure 4.65.

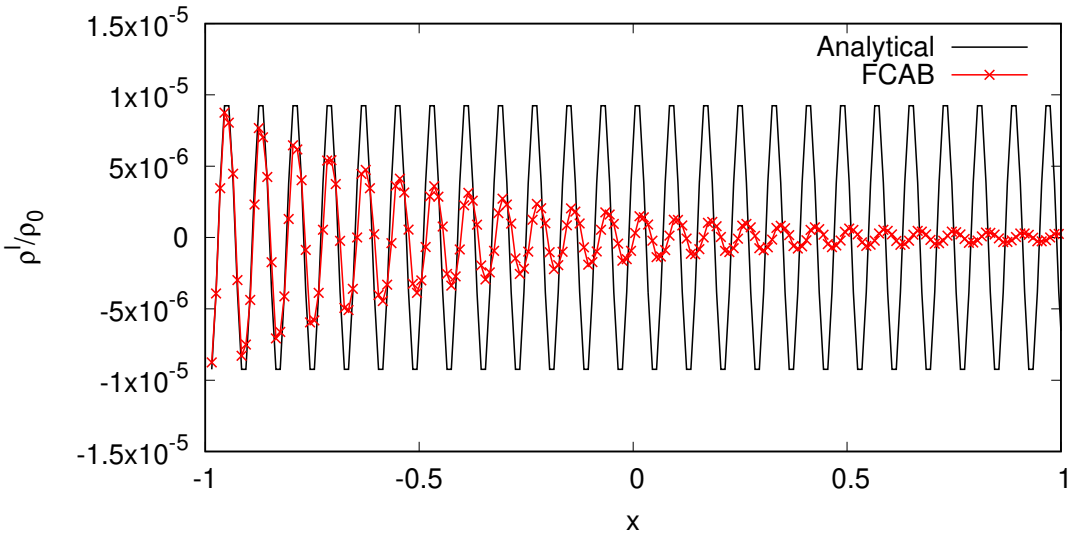

Figure 4.54: 1D planar wave propagation using F-CAB at CFL=0.1 on a uniform grid

4.2.1.2 2D Inlet wave

The second problem, considered is an oblique wave propagating at $\theta = 58^0$ to the mean flow, which approaches the wave cut-off range ($\theta = 90^0$). Also, α is set to zero due to the absence of the wave in the z-direction. The amplitude of the wave is the same as the planar wave ($\epsilon_0 = 10^{-5}$). A rectangular domain of

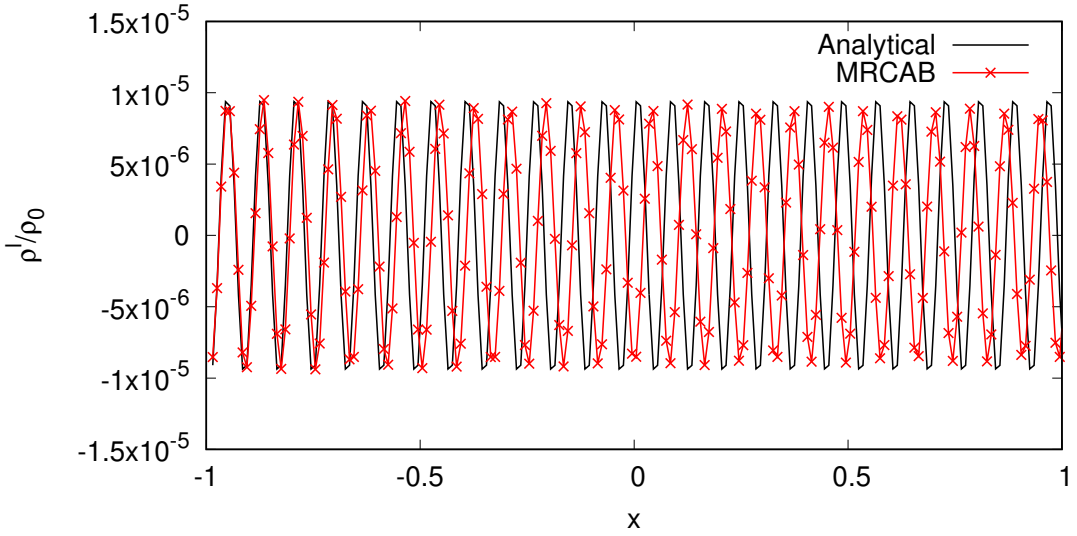

Figure 4.55: 1D planar wave propagation using MR-CAB at CFL=0.1 on a uniform grid

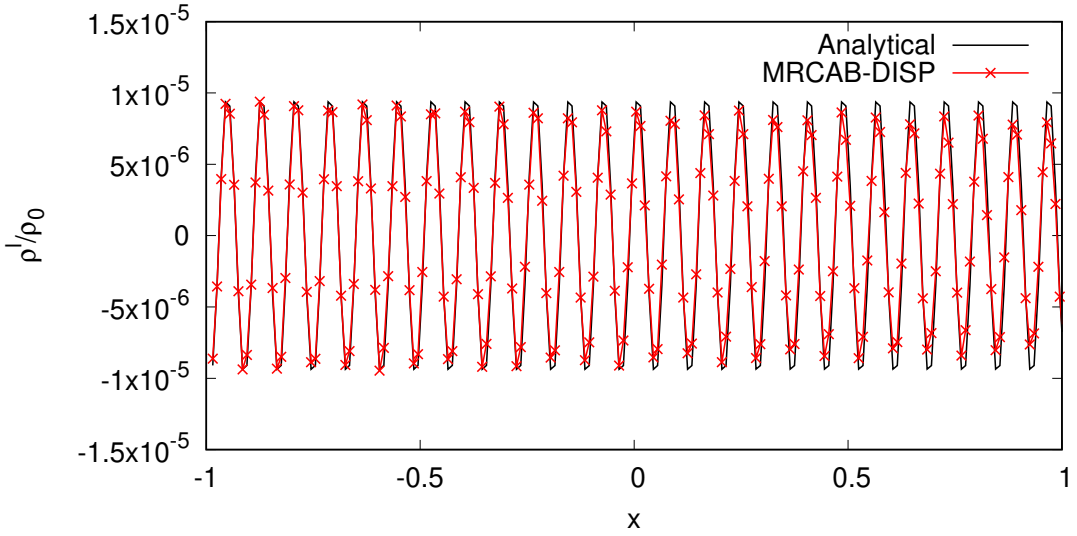

Figure 4.56: 1D planar wave propagation using MR-CAB-DISP at CFL=0.1 on a uniform grid

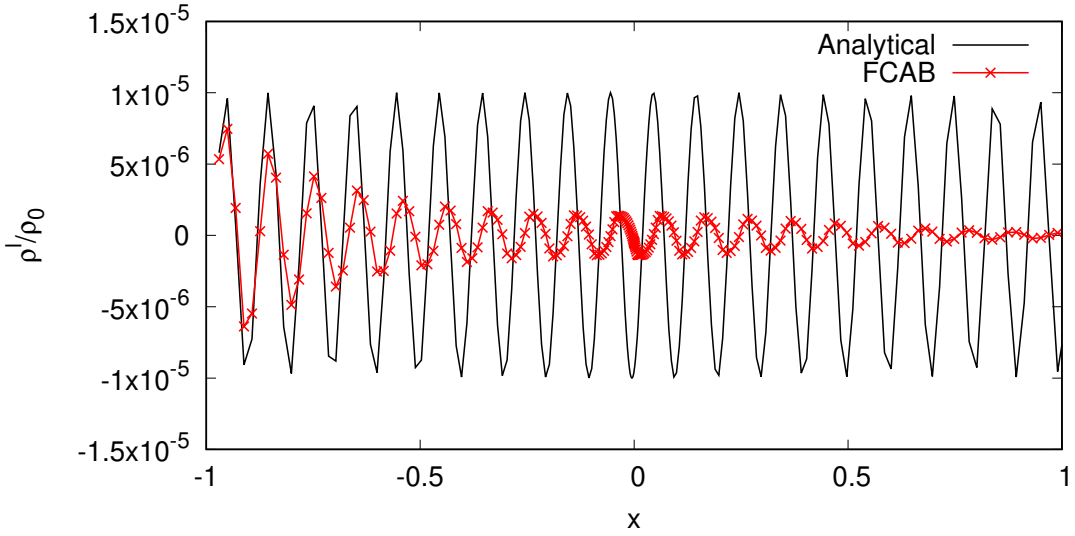

Figure 4.57: 1D planar wave propagation using F-CAB at CFL=0.1 on a non-uniform grid

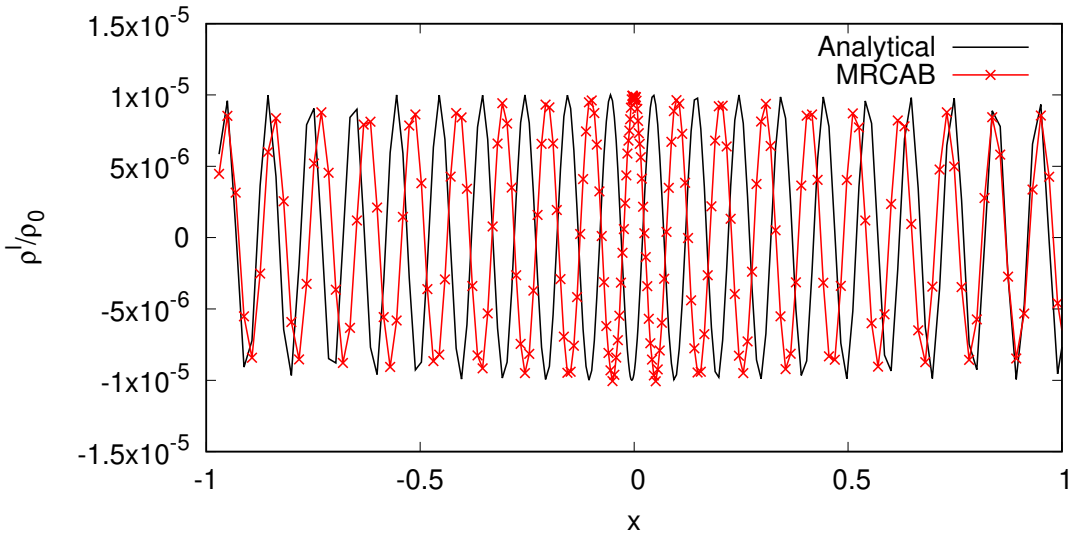

Figure 4.58: 1D planar wave propagation using MR-CAB at CFL=0.1 on a non-uniform grid

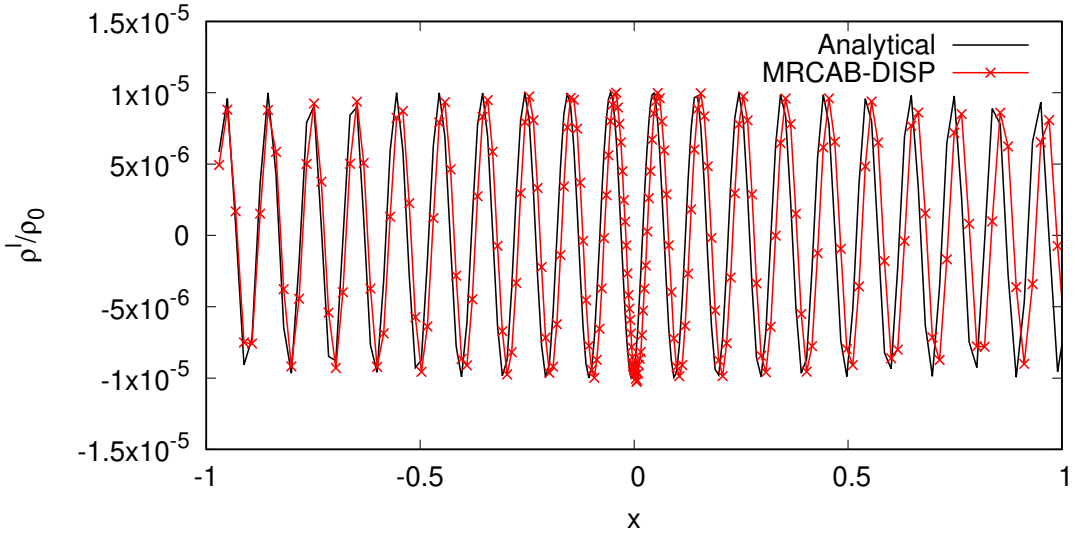

Figure 4.59: 1D planar wave propagation using MR-CAB-DISP at CFL=0.1 on non-uniform grid

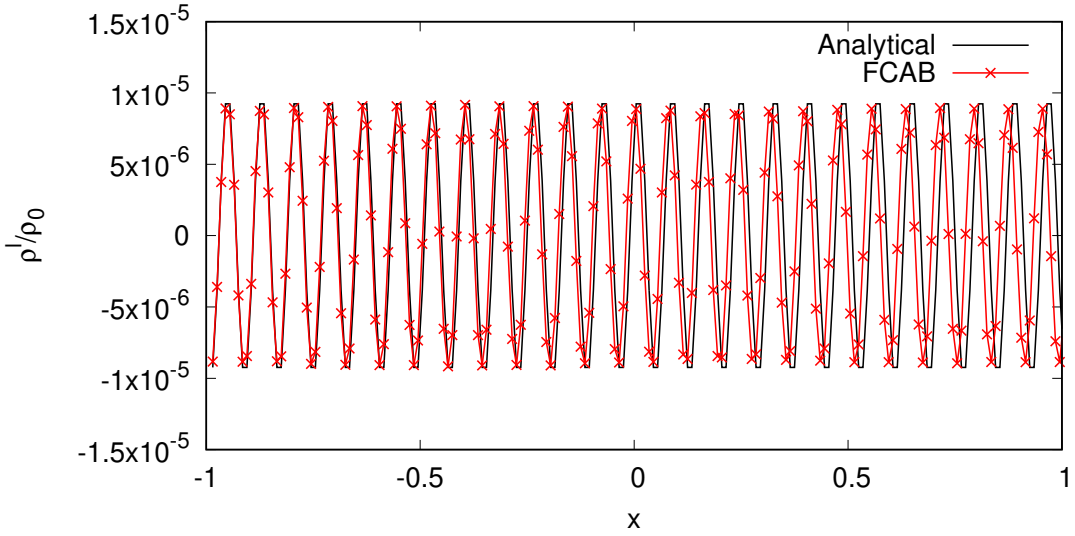

Figure 4.60: 1D planar wave propagation using F-CAB at CFL=0.8 on a uniform grid

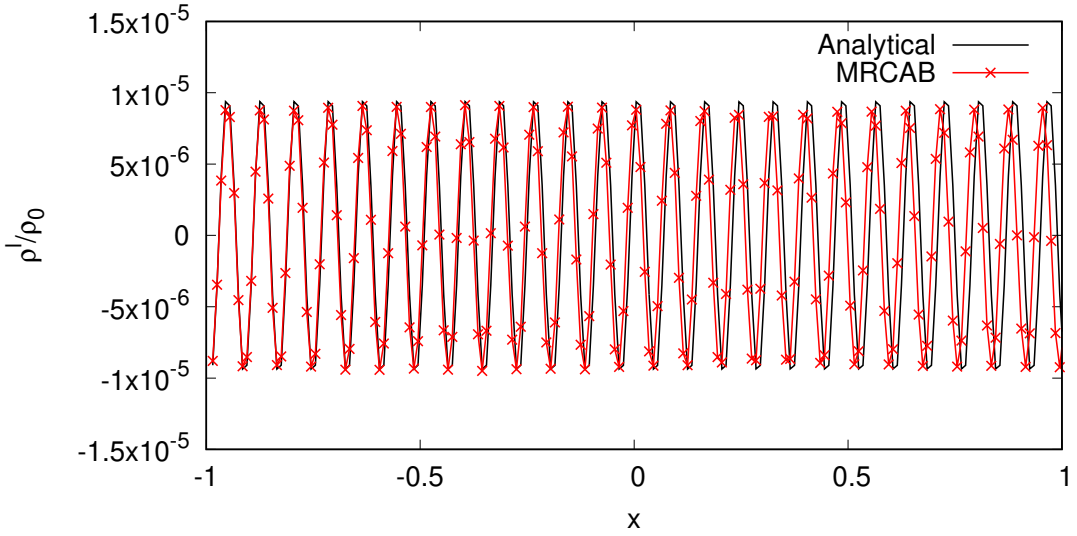

Figure 4.61: 1D planar wave propagation using MR-CAB at CFL=0.8 on a uniform grid

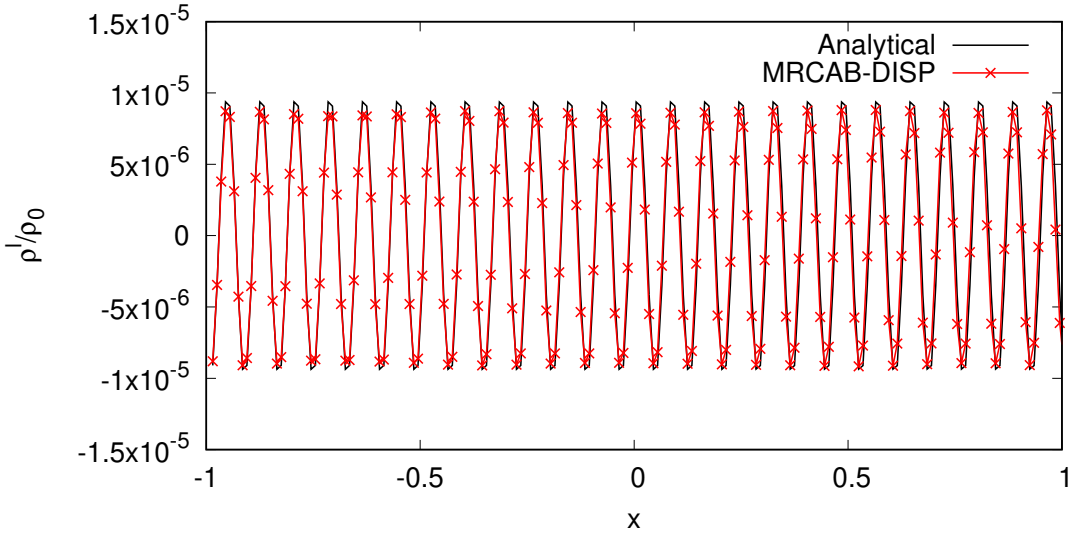

Figure 4.62: 1D planar wave propagation using MR-CAB-DISP at CFL=0.8 on a uniform grid

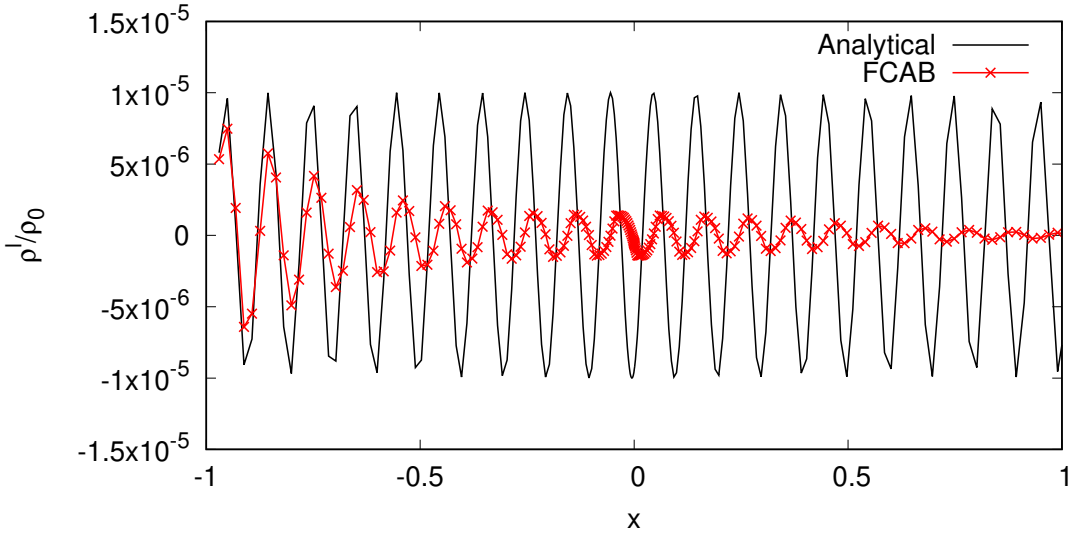

Figure 4.63: 1D planar wave propagation using F-CAB at CFL=0.8 on a non-uniform grid

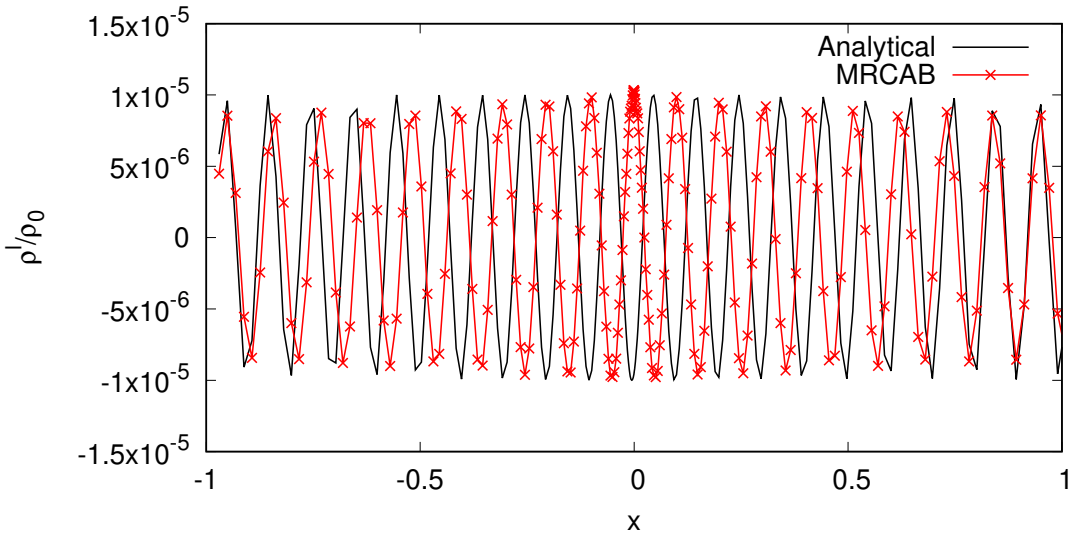

Figure 4.64: 1D planar wave propagation using MR-CAB at CFL=0.8 on a non-uniform grid

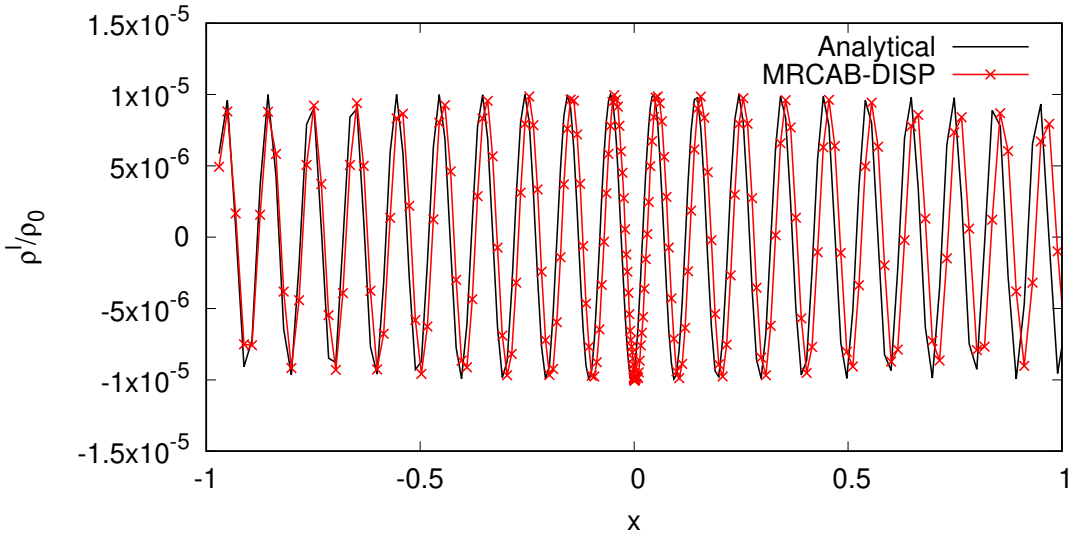

Figure 4.65: 1D planar wave propagation using MR-CAB-DISP at CFL=0.8 on non-uniform grid

200 points in the x-direction corresponding to a PPW of 15 and 9 points in the y-direction corresponding to a PPW of 9 is used. The CFL number is taken as 0.1 pertaining to the x-direction. The same inlet and outlet boundaries are used in the x-axis bounds, and the periodic boundary condition is applied in the y-direction. The relaxation parameter was chosen as the maximum value of 0.4 for this test case.

The results for the oblique wave are analogous to the planar wave. For CFL of 0.1 on uniform grids, the solution of F-CAB resulted in a loss of amplitude and phase of the incoming wave, as shown in Figure 4.66. The amplitude was recovered by the MR-CAB, as shown in Figure 4.67 and the phase was recovered by the MR-CAB-DISP scheme, as shown in Figure 4.67. The same behaviour was observed on non-uniform grids for the F-CAB, MR-CAB and the MR-CAB-DISP schemes are shown in Figures 4.69, 4.70 and 4.71, respectively.

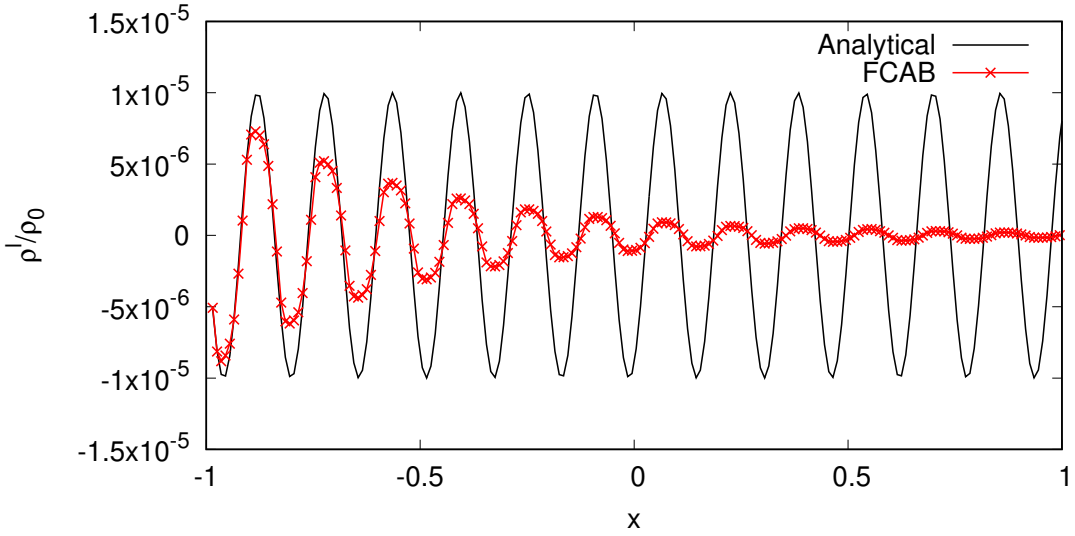

Figure 4.66: Oblique wave propagation using F-CAB at CFL=0.1 on a uniform grid

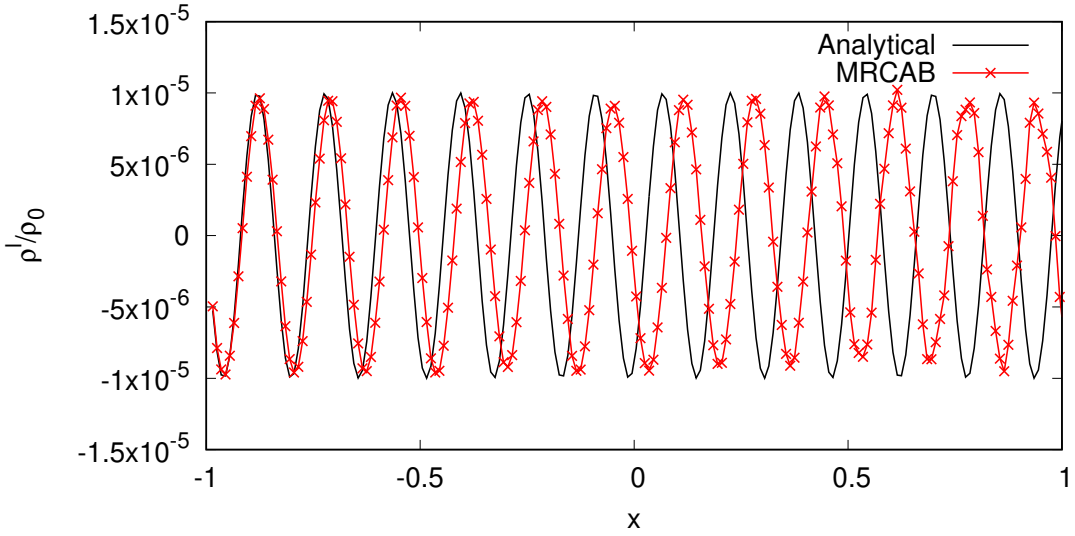

Figure 4.67: Oblique wave propagation using MR-CAB at CFL=0.1 on a uniform grid

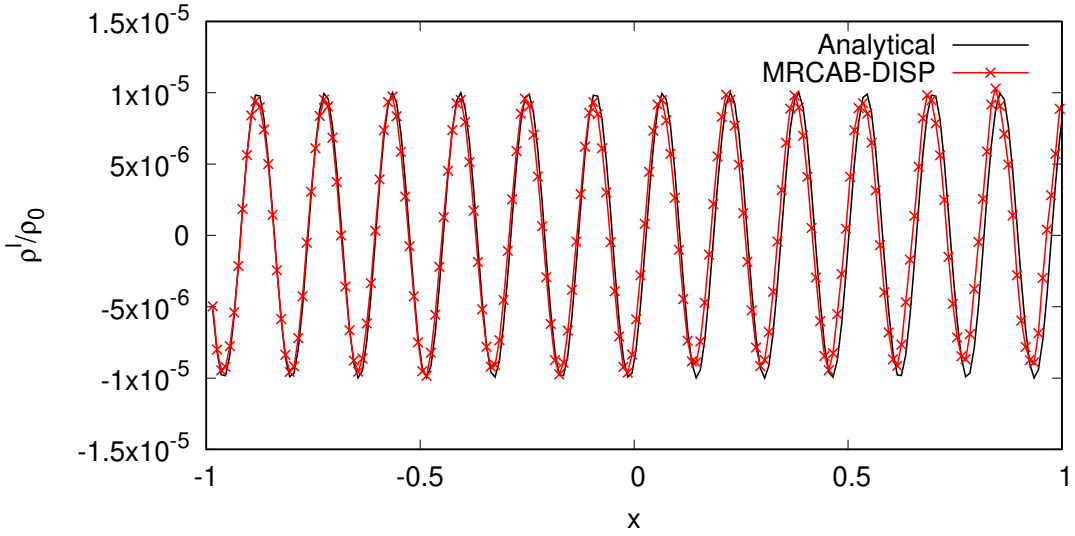

Figure 4.68: Oblique wave propagation using MR-CAB-DISP at CFL=0.1 on a uniform grid

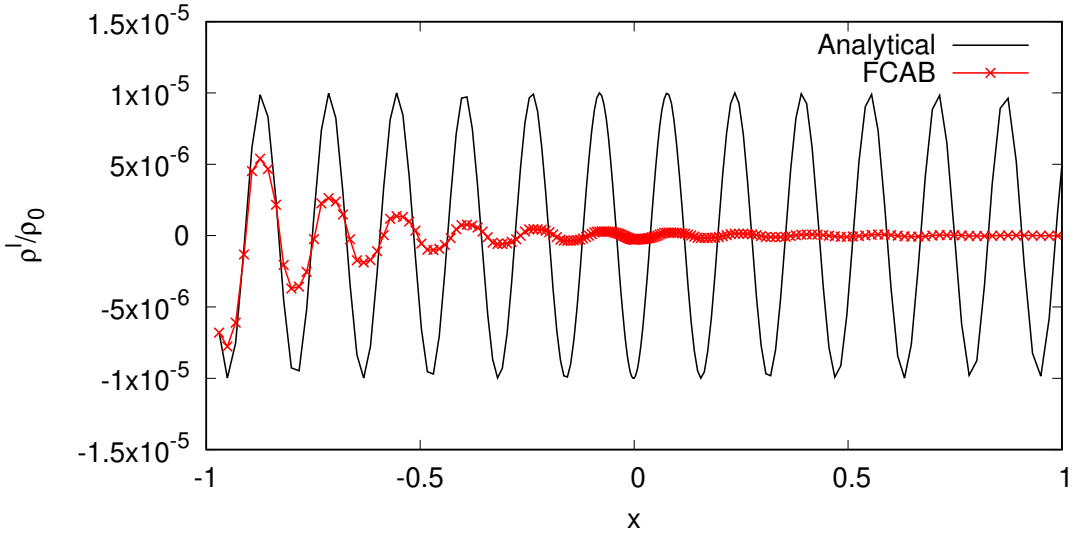

Figure 4.69: Oblique wave propagation using F-CAB at CFL=0.1 on a non-uniform grid

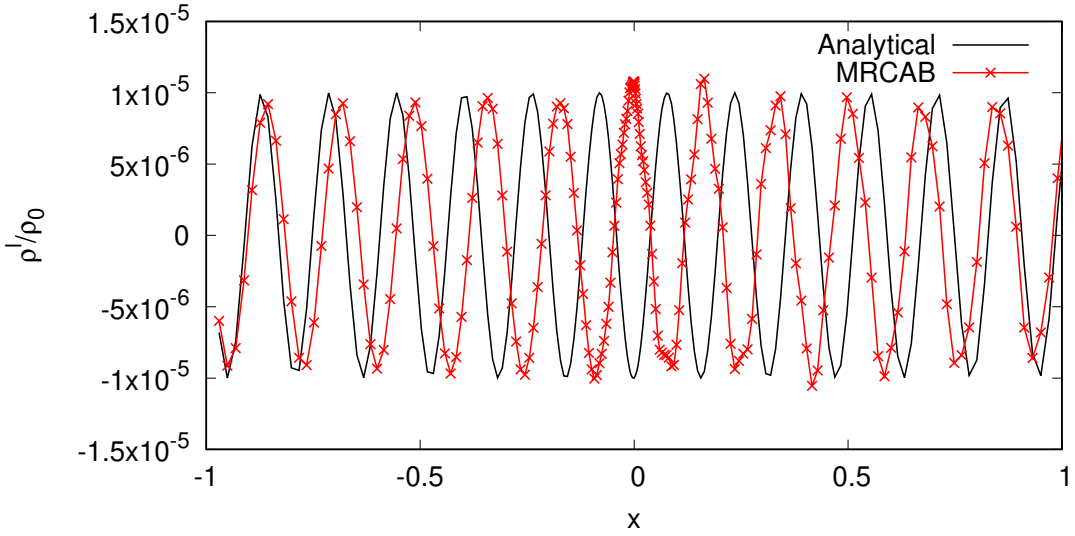

Figure 4.70: Oblique wave propagation using MR-CAB at CFL=0.1 on a non-uniform grid

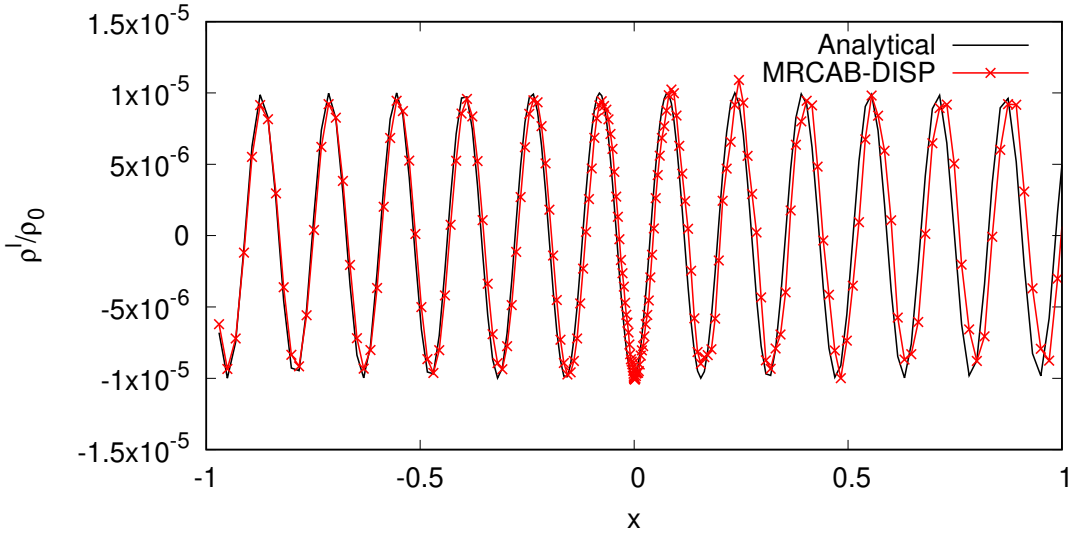

Figure 4.71: Oblique wave propagation using MR-CAB-DISP at CFL=0.1 on non-uniform grid

4.2.1.3 3D Inlet wave

The third problem, considered is the three-dimensional incoming pressure wave. The two wave angles θ and α are taken as 58^0 and 45^0, respectively. The PPW in the x-,y-, and z-direction are taken as 15, 9 and 9, respectively, on a domain of 200 cells in the x-direction and 9 cells each in the y and z-direction. The same schemes are considered as in the oblique wave test case for a CFL of 0.1. The three-dimensional wave is shown in Figure 4.72 with its components in x,y, and z-directions, respectively.

The plots are shown for the density perturbation in the xy plane at a cross-section pertaining to the centre of the domain in the direction. Similarly, plots are shown for yz plane at the centre of the domain corresponding to z=0. As expected, similar behaviour of all the three CABARET variants considered is observed, just as in the oblique wave test case. However, the propagation is symmetrical in both y and z-directions, and is shown in Figures 4.73 for the F-CAB scheme, Figures 4.74 for the F-CAB scheme and Figures 4.75 for the F-CAB scheme, respectively. This demonstrates the superiority of the new dispersion improved MR-CAB scheme over the standard CABARET scheme.

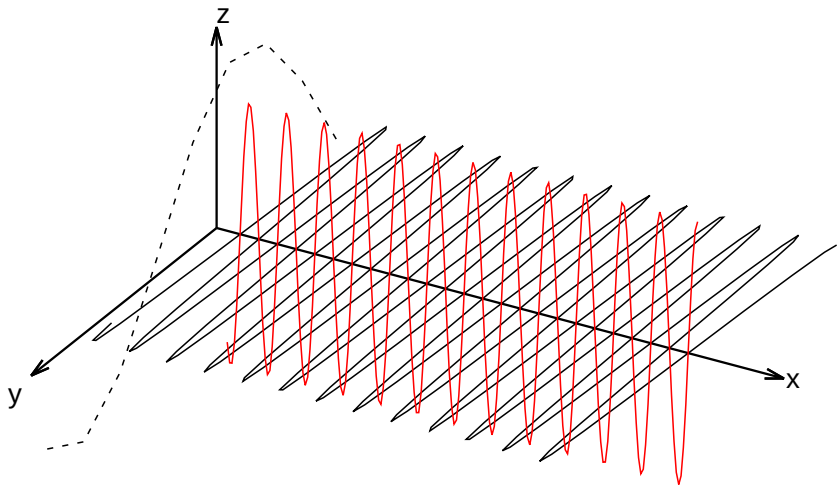

Figure 4.72: Components of the 3D incoming wave.

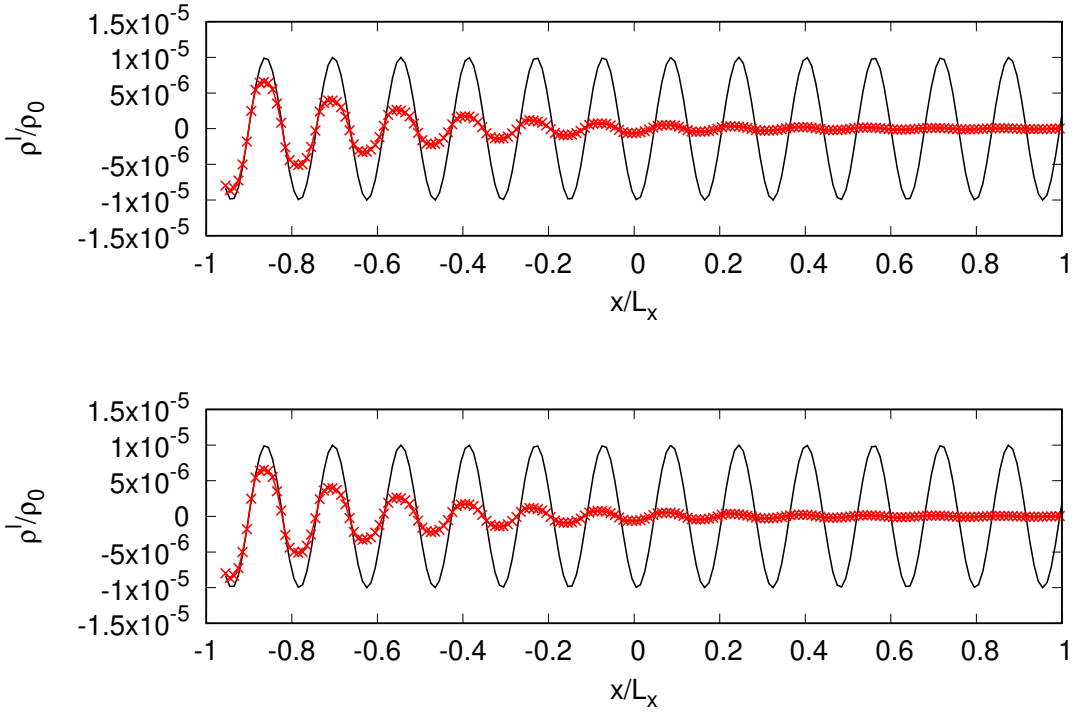

Figure 4.73: 3D incoming wave propagation using F-CAB at CFL=0.1 in the xy plane taken at $L_y = 0$ (top) and in the xz plane taken at $L_z = 0$ (bottom)

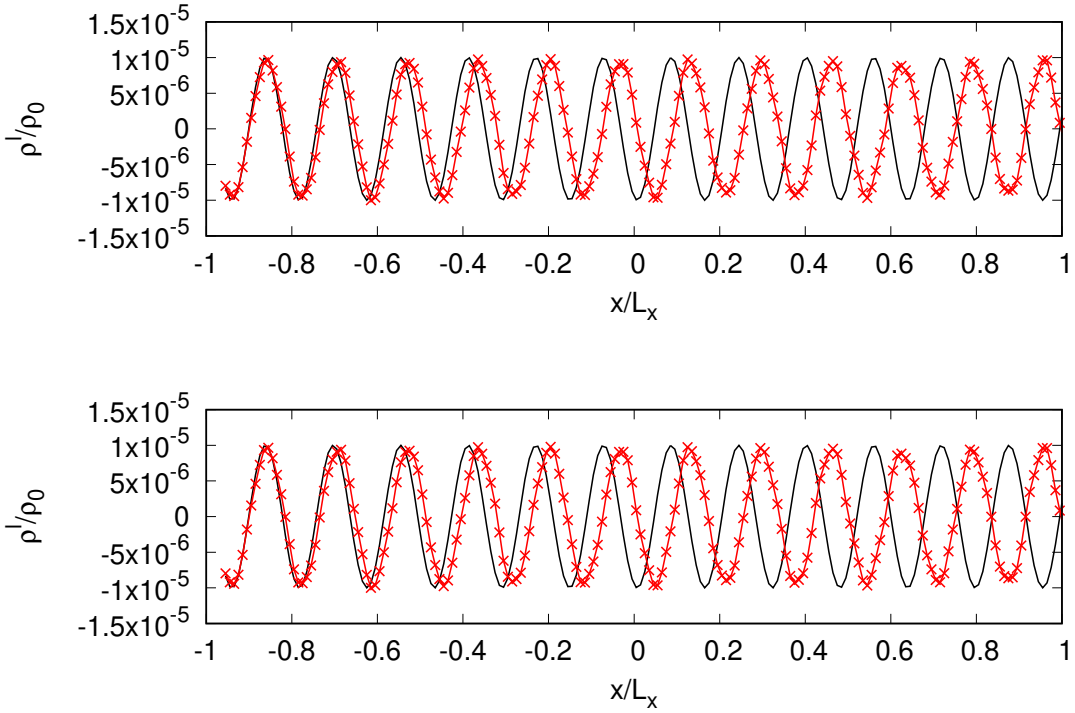

Figure 4.74: 3D incoming wave propagation using MR-CAB at CFL=0.1 in the xy plane taken at $L_y = 0$ (top) and in the xz plane taken at $L_z = 0$ (bottom)

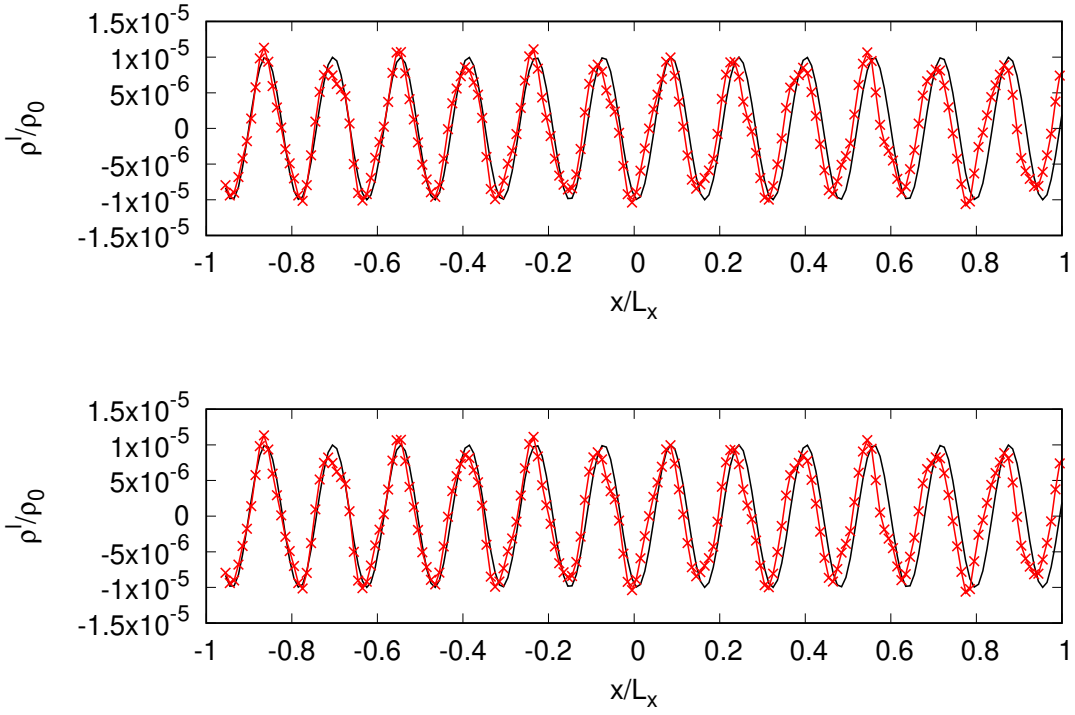

Figure 4.75: 3D incoming wave propagation using MR-CAB-DISP at CFL=0.1 in the xy plane taken at $L_y = 0$ (top) and in the xz plane taken at $L_z = 0$ (bottom)

4.2.2 Non-Linear wave propagation

A non-linear problem can be constructed using the incoming pressure wave presented in equation (4.12). This is achieved by increasing the perturbation amplitude to 0.5, i.e., $\epsilon_0 = 0.5$. Now, the analytical solution is no longer applicable but can be obtained from a numerical reference solution at higher mesh points using the standard CABARET, F-CAB scheme. The control time was taken as 15 when the steepening of the wave occurs producing a z-like profile. This happens as the waves crest travels faster than the trough. The fine grid solution corresponds to 2500 PPW of the incoming wave and is considered as converged compared to the numerical solutions obtained using CABARET variants at 100 PPW.

The F-CAB scheme and the MR-CAB scheme using the relaxation value of 0.2 are compared. Notably, two variants of the MR-CAB scheme, the non-linear limiter, which switched back to the standard F-CAB scheme in the shock re-

gions, and also, the switching of the anti-dispersion term in the shock regions. Hence, the purpose is to demonstrate the use of the limiter in the non-linear regions to switch to the original F-CAB scheme, and effectively switching off the anti-dispersion term in the same. The CABARET variant with both the non-linear switch and the anti-dispersion switch is denoted by the suffix 'LIM', as aforementioned in section 2.3.

The first Figure 4.76 shows the converged reference solution and the coarse grid solution for 2500 and 100 PPW, respectively, using the F-CAB scheme. As shown, the F-CAB scheme captures the non-linear shock region for just 3-4 cells even for 100 PPW. Also, the MR-CAB-DISP scheme for different relaxation parameters of 0.2 and 0.4, is shown in Figure 4.77, which allow oscillation due to the anti-dispersion term in the shock regions. The oscillations are aggravated for higher relaxation parameter. This is due to the feeding of the anti-dispersion term from the increased range of proper solution near the shocks. Finally, the addition of the limiters in both the relaxation and the anti-dispersion term free the solution of any oscillations and recovers the original standard CABARET in the shock region, as shown in Figure 4.78.

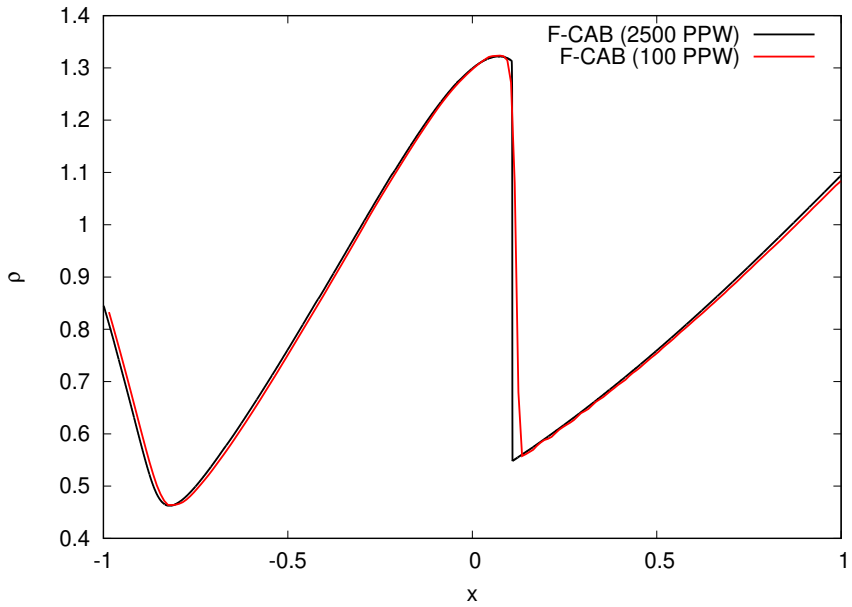

Figure 4.76: Non-linear wave propagation using F-CAB for PPW of 100 for the coarse grid and 2500 for the fine grid

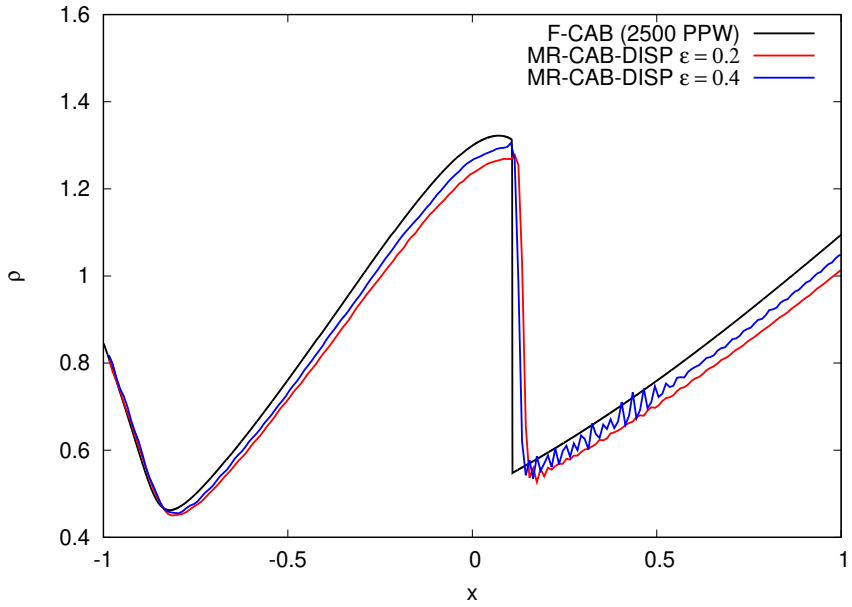

Figure 4.77: Non-linear wave propagation using MR-CAB-DISP for different relaxation parameters

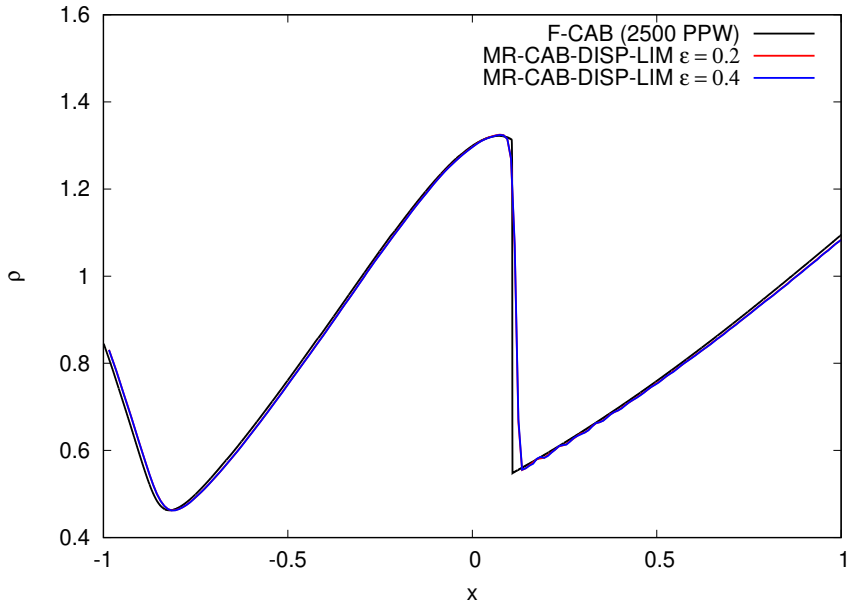

Figure 4.78: Non-linear wave propagation using MR-CAB-DISP with limiter for different relaxation parameters

4.3 Euler equations

The dispersion improved scheme is implemented for the two-dimensional Euler equations. The standard Sod problem Sod (1978) was solved in two-dimensions such that the planar waves generated are propagated at an oblique angle. The problem is solved on a rectangular grid and solved using the standard F-CAB scheme and the new MR-CAB scheme with dispersion, to demonstrate the non-linear scheme and the limiting of the dispersion term. In the numerical calculation, the discontinuity makes angle $\theta = 45^o$ degrees to the x-axis. The length (L) and the height (H) of the computational domain are taken to be 6 and 1, respectively. The standard initial conditions are

$$[\rho, u, v, p]_{left} = [1, 0, 0, 1], \qquad [\rho, u, v, p]_{right} = [0.125, 0, 0, 0.1] \tag{4.23}$$

Also, the diaphragm at $t = 0$ is placed at 2.25 units on the bottom boundary and inclined at an angle $\theta = arctan(1)$, such that the implementation of the boundary conditions is straightforward. The waves are propagated for a time of 1.2 units, such that the left and right conditions are maintained at the left and right boundaries, respectively. Also, for the top and bottom boundaries, a shifted-periodic manner of boundary conditions are applied, as shown in Figure 4.79. The ghost variables on the top and the bottom boundary are shifted to the right and left, respectively. This set-up is equivalent to solving the one-dimensional Sod problem on a domain of length, $L_\theta = \frac{L}{sin\theta}$ and of height $H_\theta = \frac{H}{sin\theta}$.

The density and velocity of the solution taken at $y = 0$ line, is shown in Figures 4.80 and 4.81, respectively, for the F-CAB and the MR-CAB with dispersion for a grid of 96×16, demonstrates the effectiveness of the anti-dispersion limiting in non-linear regions. The difference in the solution between the F-CAB and the MR-CAB with dispersion for density and velocity is shown in Figures 4.82 and 4.83, respectively. It is seen that the maximum difference in density is

approximately 0.3% and the maximum difference in velocity is 1.5%, demonstrating that the limiter is performing well. Finally, the density contours in the two-dimensional domain are presented in Figure 4.84, shows the solution free of oscillations for the MR-CAB scheme with dispersion improvement. The shock is captured by both the schemes approximately over 3 cells, without any oscillations.

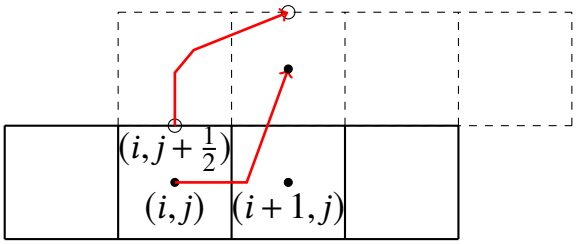

Figure 4.79: Schematic showing application of the shifted periodic boundary conditions for the oblique Sod problem.

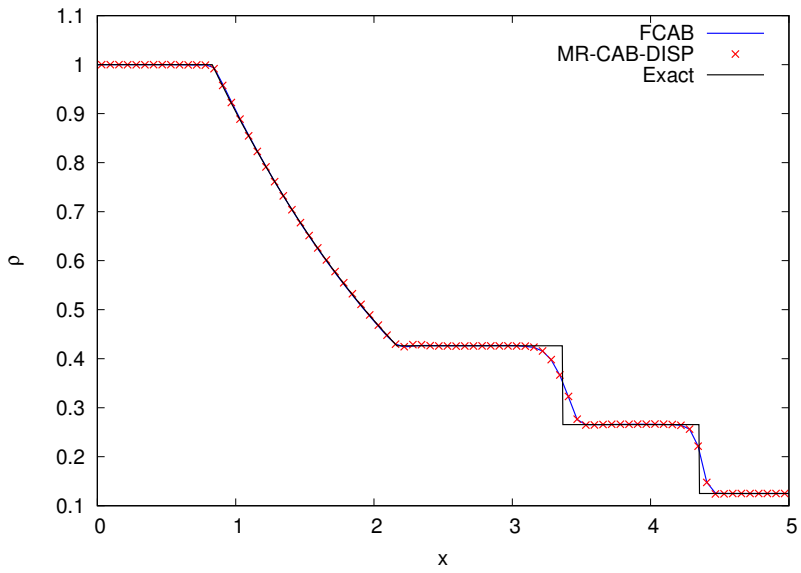

Figure 4.80: Comparison of density profiles for the F-CAB and the MR-CAB with dispersion schemes, for the oblique Sod problem.

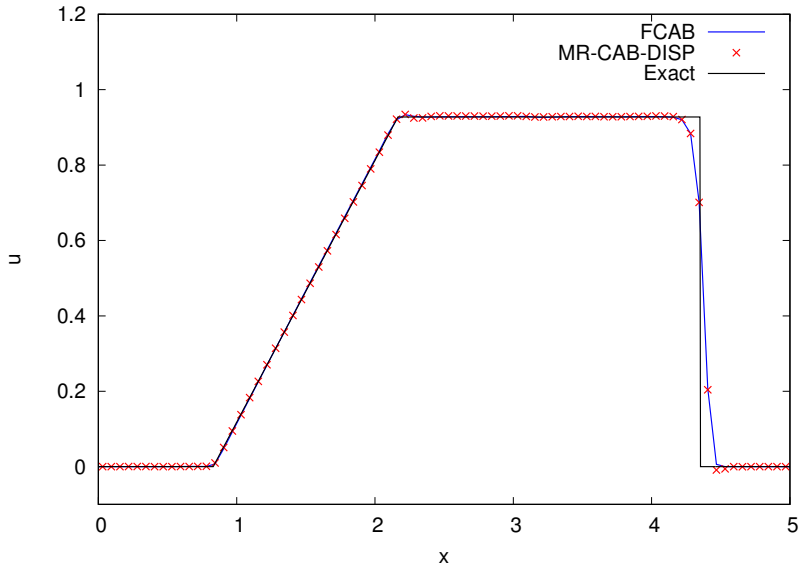

Figure 4.81: Comparison of velocity profiles for the F-CAB and the MR-CAB with dispersion schemes, for the oblique Sod problem.

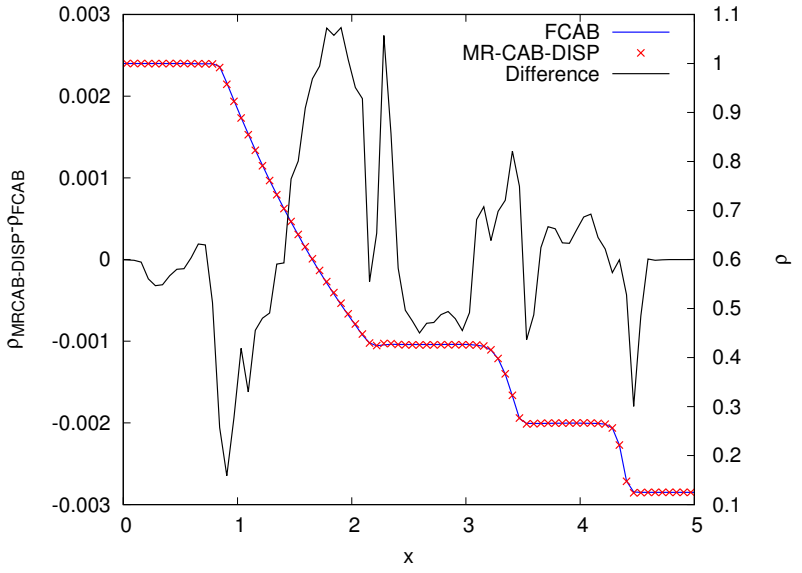

Figure 4.82: Difference in the density profile for the F-CAB and the MR-CAB with dispersion schemes, for the oblique Sod problem.

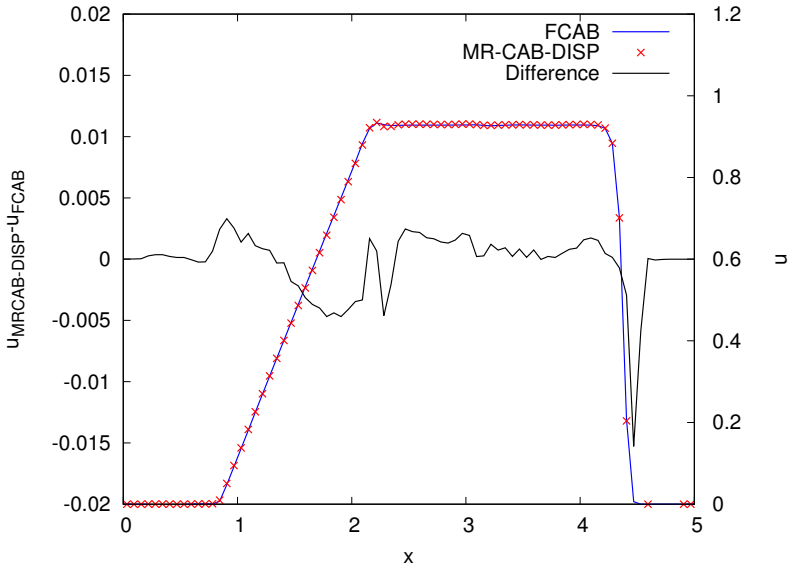

Figure 4.83: Difference in the velocity profile for the F-CAB and the MR-CAB with dispersion schemes, for the oblique Sod problem.

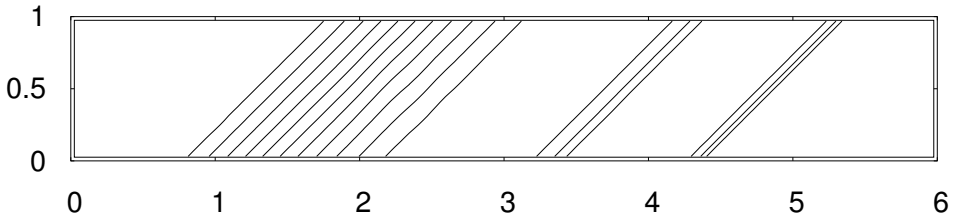

Figure 4.84: Density contours for the oblique Sod problem solved using the MR-CAB with dispersion.

4.4 Viscous modelling

The aforementioned collocated gradient method has been implemented in the CFOAM solver, replacing the existing vertex method. They are validated for the laminar flow over a flat-plate (Hirsch, 2007) problem and timed to observe the sequential performance on the CPU. Furthermore, the order-of-accuracy was also obtained through a series of grid sizes. The test case is presented in section 4.4.1, followed by its validation, accuracy test and sequential performance in section 4.4.2 and section 4.4.3, respectively.

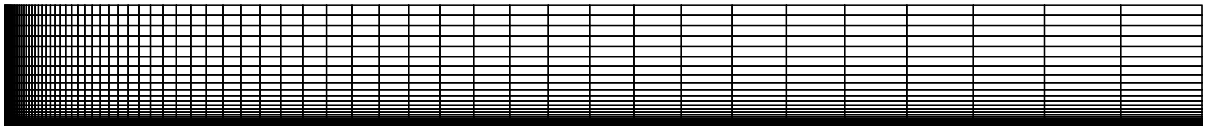

Figure 4.85: Flat plate computational domain in the XY-plane.

Grid name	Grid points in x, y, z directions
m0	$65 \times 33 \times 1$
m1	$130 \times 65 \times 1$
m2	$260 \times 130 \times 1$

Table 4.1: Grid sizes considered for the test of order-of-accuracy.

4.4.1 Flat plate test case

The flat plate geometry is shown in Figure 4.85 and is of $0.2m \times 0.02m \times 1m$ in size. The grid is stretched in the y-direction such that at least 30 grid points lie in the boundary layer and the first point lies at 1mm. The stretching in the x-direction is applied to reduce the grid size along the flat plate. Also, the mesh is extruded in the z-direction uniformly to a single layer of unit length, due to the two-dimensional nature of the flow. The boundary conditions are taken to be pressure inlet on the left boundary, pressure outlet on the top and the right boundaries, viscous wall on the bottom boundary and symmetry planes in the z-direction. The three grids are generated using a commercial grid generator ICEM CFD and are presented in Table 4.1.

The flat plate solutions are verified against the exact solution of the skin friction coefficient C_f using the laminar Blasius solution (Schlichting, 2003). The Mach number of the flow is taken to be 0.2 and the Reynolds number to be 10,000, respectively. The solver is run for 9×10^5 iterations and reaches a normalised (normalised to the first iteration residual) density residual convergence of three-orders of magnitude.

4.4.2 Validation

The coefficient of skin-friction is compared with the analytical Blasius solution, given by $C_f = \frac{0.664}{Re_x}$, where $Re_x = \frac{\rho u x}{\mu}$. They are presented for the vertex, and the collocated approaches in Figure 4.86. Moreover, are observed to be in good agreement, considering the convergence to three-orders of magnitude in the residual. The fluctuations may be attributed to the parabolic boundary conditions (Faranosov et al., 2013b), high stretching in the mesh and the lack of a full free-stream upstream of the flat-plate.

The L_2 norm of the error between the theoretical skin friction coefficient values and the obtained values is calculated for all grids and methods. The step size h is computed using the number of cells in the mesh. The order-of-accuracy of the schemes is computed and is presented in Figure 4.87. It is seen that all methods are nearly of the order 1.9 and may improve for finer meshes with less stretching in the x-direction. The sequential performance of these methods is discussed in the following section.

4.4.3 Sequential performance

The sequential performance is required to be understood as the first step towards efficient parallel performance. It also helps in identifying the effect of algorithmic changes on the performance and other bottlenecks. The performance tests were run on the grids shown in Table 4.2. The PSU nozzle grids (Doty and McLaughlin, 2003) are provided by Kalyan (2015) and were also generated using ICEM CFD. The PSU test grids were not run for validation but only used for performance measurements for the sake of completeness. All tests were run sequentially on an Intel i7 (4770S) processor with an 8MB cache memory and 8GB RAM, using GNU compilers (Gnu, 2014) and compiled without optimisation flags. The sequential performance of the gradient methods in computing

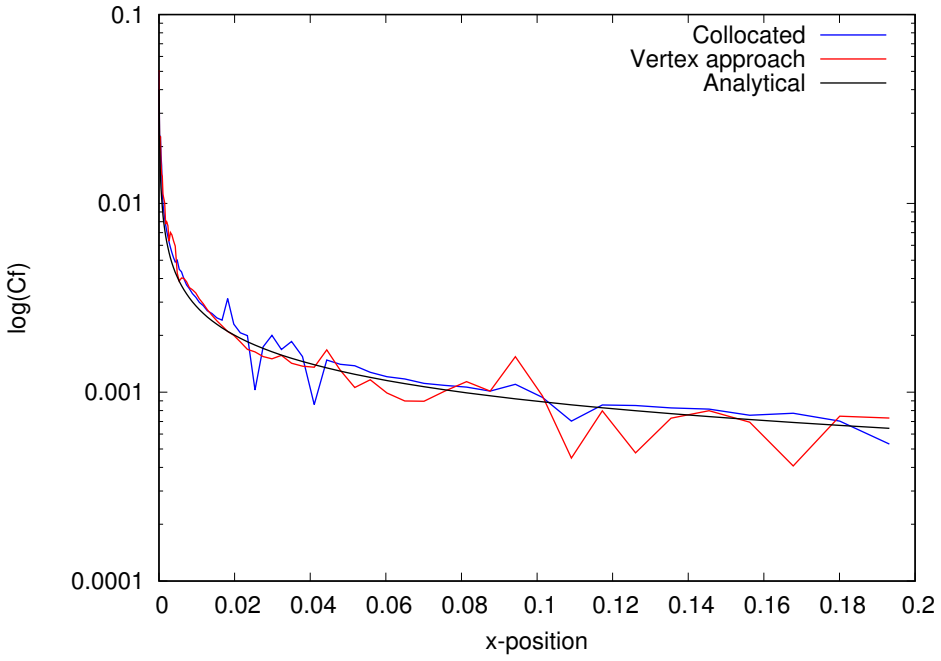

Figure 4.86: Skin friction co-efficient C_f for the collocated and the vertex approach.

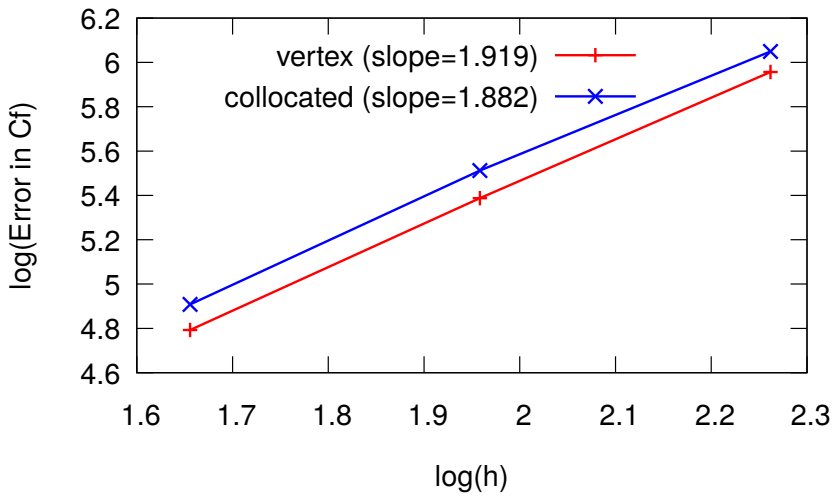

Figure 4.87: Order-of-accuracy for the vertex and the collocated approach.

Grid name	No. of Points	No. of Cells	No. of Faces
m0	4290	2048	8288
m1	16900	8256	33217
m2	67600	33411	134032
Psu_1	1658285	1612984	4883786
Psu_2	2415400	2355300	7125448

Table 4.2: Grid used for performance evaluation.

Grid name	Collocated runtime (s)	Vertex runtime (s)	Speed-up
Mapping	face-cell	node-cell	
m0	7.3E-04	1.8E-03	2.4
m1	3.0E-03	7.2E-03	2.4
m2	1.2E-02	2.9E-02	2.4
Psu_1	5.5E-01	2.0E+00	3.6
Psu_2	8.0E-01	2.9E+00	3.6

Table 4.3: Runtimes and comparison of Collocated and Vertex methods.

the face and cell gradients is taken as the starting point. Each method is timed for a single iteration (averaged for 100 samples) and is compared.

The collocated and the vertex gradients runtimes are compared to find the most economical method. The results are presented in Table 4.3. The collocated method outperforms the vertex-approach by a factor of 3.5× as observed for large grids. This could be due to multiple reads of the same data for every node when the node gradient is being computed.

The collocated method using the cell-faces mapping is modified to 3 variants based on storage. The first variant referred to as *all_store* involves storing both the cell and the face gradients. The second variant, referred to as $face\_store$, involves computation of face gradients directly without storing the cell gradients. Finally, the third variant referred to as *cell_store* involves the storage of cell-gradients and exchanging them at the flux calculation to compute face gradient.

Table 4.4 shows the time-per-iteration for the *all_store*, $face\_store$, and

grid	all_store runtime (s)	face_store runtime (s)	cell_store runtime (s)
m0	0.02	0.02	0.02
m1	0.07	0.08	0.06
m2	0.30	0.34	0.25
Psu_1	13.37	17.21	11.43
Psu_2	20.05	25.43	16.58

Table 4.4: Time per iteration for the three variants and comparison.

grid	vertex runtime (s)	cell_store vs vertex Percentage %	face_store vs vertex Percentage %	all_store vs vertex Percentage %
m0	0.02	27.54	-5.76	9.05
m1	0.08	24.20	-6.60	8.04
m2	0.31	26.08	-8.92	5.15
Psu_1	15.37	34.45	-10.69	15.02
Psu_2	23.09	39.25	-9.19	15.17

Table 4.5: Time per iteration for the three variants and comparison with vertex approach.

cell_store variants. It is observed that, the *cell_store* variant is 15-20% faster than *all_store* and 35-50% faster than the *face_store* variant. As expected, the *face_store* variant is the slowest and can be seen due to many reads of the face variables. Furthermore, the time spent to compute the gradients per iteration is 25% higher than the vertex-approach. Hence, in conclusion, the cell-gradients need to be stored for computational efficiency while using less memory. The comparison of the time per iteration of all the variants with the vertex approach is presented in Table 4.5. It is clear that the *face_store* variant is in-efficient, *all_store* variant is 15% better in the 3D case and 5% in the 2D case, and *cell_store* variant is 26% better in the 2D case and 39% in the 3D case, all with respect to the vertex approach. It can be seen that the use of large grids is useful in demonstrating the speed up as this difference was not observed for smaller grids.

The percentage of time spent by each of the variants in computing only the gradient per iteration is shown in Table 4.6. This helps in separating the storing and the computing the gradient, and hence identify the fastest variant in

grid	all_store	face_store	cell_store
m0	23.5	12.5	9.1
m1	24.1	12.5	9.1
m2	23.9	13.1	9.4
Psu_1	35.2	16.6	9.6
Psu_2	36.0	16.6	9.9

Table 4.6: Percentage of time spent in computing gradient per iteration.

computing the gradient, as the storage depends on the stencil. As expected the all_store variant spends more time per iteration, i.e., 36% in computing compared to other variants. Whereas, the cell_store variant uses only 10% of the time computing and rest of the time storing the variables compared to 16% of the face_store variant.

It has been demonstrated that the collocated approach while using nearly the same storage of the vertex approach, as the number of vertices and cells are the same in a grid. The collocated approach is at most 3.5× faster than the present method in the in-house solver. Although there are race-conditions in updating the cell-gradient which need to be serialised for parallel implementation, the trade-off could be beneficial in the resulting speed-up in accelerating the viscous flux computation.

4.5 Summary

- The dispersion improved CABARET (MRCAB-DISP) scheme has been demonstrated to work well for the linear advection equation. The choice of the relaxation parameter (ϵ) was tested for various test profiles, notably for a rectangular pulse (test case R) and a cosine wave modulated rectangular pulse (test case Z). It was found that $\epsilon = 0.2$ gave satisfactory solutions compared to the CABARET (F-CAB) scheme. Furthermore, the effect of the change in amplitude did not affect the solution for this optimal choice

of ϵ.

- Next, the isothermal gas dynamics equations were solved using the dispersion improved scheme with the suggested optimal value of the relaxation parameter.

  - Firstly, the linear wave propagation problem was solved for an incoming wave in one-, two-, and three-dimensions. It was demonstrated that the MRCAB-DISP scheme preserved well both the amplitude and the frequency of the wave, whereas the F-CAB scheme dispersed the wave.

  - Secondly, the non-linear wave propagation problem in one-dimension was solved to demonstrate the effect of the dispersion limiter discussed in section 2.3.1. With the use of the limiter the dispersion improved scheme reduced to the standard CABARET scheme, therefore, proving its effectiveness.

- The dispersion improved CABARET scheme is also demonstrated for the Euler equations. The Sod problem was solved in two-dimensions by keeping the initial conditions at an oblique angle. The results further showed the effectiveness of the limiters of the new scheme.

- The gradient computation of the in-house CABARET solver was updated from the vertex approach to the collocated approach. The implementation was validated for laminar flow over the flat plate. Additionally, the sequential performance of the gradient computation was found to be 3.5× faster for large test grids.

The conclusions of the present work and future work are suggested in the following Chapter.

Chapter 5

Conclusions and Future work

The focus of the present work is on the development of a new class of dispersion improved CABARET scheme for linear and non-linear wave propagation problems. The dispersion improvement to the three-time-level CABARET scheme given by Goloviznin and Samarskii (1998a) is extended to the two-level predictor-corrector CABARET scheme.

To improve the dispersion properties of the standard CABARET scheme, an anti-dispersion term is added to the flux terms. This inclusion of the anti-dispersion term led to a significant reduction in the dispersion error for the whole range of CFL numbers, especially at low CFL numbers (CFL<0.3). The anti-dispersion term consists of the third-order derivative of the flux scaled by a tuning parameter. Also, to maintain the low-dissipative properties of the non-linear CABARET scheme (which uses flux correction based on the maximum principle), relaxation procedures for the flux correction are developed. Also, the new scheme is extended and implemented for the full three-dimensional Euler equations.

Firstly, the optimal tuning parameter is found to be $\frac{-1}{12}$ based on the linear stability analysis. Also, the resulting linear scheme was demonstrated both analytically, and experimentally for the linear advection test case to be fourth-order accurate. A switch to turn-off the anti-dispersion term in the regions of shocks is developed. The effectiveness of this switch is demonstrated for different non-linear wave propagation problems.

Secondly, the relaxation scheme to accommodate this change in flux due to the addition of anti-dispersion term is developed. Two variants of relaxation schemes are proposed, and the most suitable scheme and the tunable parame-

ter is chosen based on the advection of a rectangular wave, and a rectangular wave superimposed by a cosine wave. Moreover, a limiter has been developed to switch-off this additional relaxation at regions of discontinuities. The best relaxation scheme (MR-CAB) is demonstrated for the two-dimensional oblique Sod problem and one-dimensional non-linear wave propagation test case.

In summary, the new dispersion improved CABARET scheme is proposed to have both the desired dispersion properties while holding to the standard CABARET scheme in regions of discontinuities. This results in the anti-dispersion term active in linear flow regions and de-active in non-linear flow regions and is demonstrated for different governing equations. The new scheme, the relaxation variants and the limiters are presented in detail in Chapter 2.

Firstly, various one-dimensional test profiles are advected using the linear advection equation. They demonstrate the superiority of the new scheme compared to the standard CABARET scheme in capturing a wide range of flow features. And these are presented in section 4.1. Also, the dispersion improved CABARET scheme is shown to be more accurate than the Dispersion Relation Preserving (DRP) scheme of Tam and Webb (1993b), especially for non-smooth test profiles.

Secondly, the scheme is implemented to gas dynamics problems and is demonstrated to preserve the incoming one-, two-, and three-dimensional acoustic waves. In comparison, the standard CABARET scheme dispersed the incoming waves, and these results are presented in section 4.2. Furthermore, it was shown that even for moderate grid resolutions the new scheme captures well the amplitude and phase of the oblique acoustic wave even near cut-off wavenumbers in both two-, and three-dimensions. Lastly, for the non-linear wave propagation problem, the new CABARET scheme automatically reduces to the standard CABARET scheme due to the limiters for the anti-dispersion flux term. The Sod test case (presented in section 4.3) and the non-linear wave

propagation test case demonstrated the effectiveness of the limiters.

Another part of the present work involved the implementation of the collocated method of computing the viscous gradients in the in-house solver and is presented in section 4.4. This was validated for the laminar flow over the flat-plate, and the order of accuracy of both methods is found to be 2.0. Also, compared to the existing vertex approach, the collocated approach was found to be almost 3.5× faster for large grids sizes, for a sequential implementation, while keeping the same memory consumption.

Appendix A

Tables

A.1 OOA of 1D Linear advection test cases

A.1.1 OOA of DRP scheme

Grid points	L1 error	OOA	L1 error	OOA	L1 error	OOA
	CFL=0.1		CFL=0.2		CFL=0.8	
6400	3.19e-06	2.30	3.05e-06	2.36	9.00e-07	3.77
3200	1.57e-05	1.25	1.57e-05	1.24	1.23e-05	1.27
1600	3.73e-05	2.22	3.70e-05	2.23	2.96e-05	2.03
800	1.73e-04	3.15	1.73e-04	3.15	1.21e-04	2.89
400	1.54e-03	2.69	1.53e-03	2.68	8.94e-04	2.50
200	9.89e-03	-	9.86e-03	-	5.06e-03	-

Table A.1: L1 errors for DRP scheme for case BB for different CFL

Grid points	L1 error	OOA	L1 error	OOA	L1 error	OOA
	CFL=0.1		CFL=0.2		CFL=0.8	
6400	3.01e-01	-	3.03e-01	-	3.11e-01	-
3200	3.00e-01	-	3.01e-01	-	3.05e-01	-
1600	2.97e-01	-	2.99e-01	-	3.06e-01	-
800	2.98e-01	-	2.99e-01	-	3.02e-01	-
400	3.00e-01	-	3.01e-01	-	2.96e-01	-
200	2.89e-01	-	2.90e-01	-	2.99e-01	-

Table A.2: L1 errors for DRP scheme for case JS for different CFL

A.1.2 OOA of F-CAB scheme

Grid points	L1 error	OOA	L1 error	OOA	L1 error	OOA
	CFL=0.1		CFL=0.2		CFL=0.8	
6400	6.02e-04	1.85	4.13e-04	1.86	6.05e-05	2.01
3200	2.16e-03	1.64	1.50e-03	1.73	2.43e-04	2.03
1600	6.76e-03	1.39	4.99e-03	1.55	9.93e-04	2.01
800	1.77e-02	1.49	1.46e-02	1.30	4.01e-03	2.00
400	4.97e-02	1.19	3.61e-02	1.44	1.60e-02	2.21
200	1.13e-01	-	9.77e-02	-	7.41e-02	-

Table A.3: L1 errors for F-CAB for case BB for different CFL

Grid points	L1 error	OOA	L1 error	OOA	L1 error	OOA
	CFL=0.1		CFL=0.2		CFL=0.8	
6400	4.59e-03	0.78	4.18e-03	0.77	1.13e-02	0.74
3200	7.90e-03	0.86	7.11e-03	0.79	1.89e-02	0.77
1600	1.44e-02	0.87	1.23e-02	0.84	3.23e-02	0.80
800	2.62e-02	0.83	2.20e-02	0.83	5.61e-02	0.84
400	4.66e-02	0.90	3.92e-02	0.84	1.00e-01	0.87
200	8.72e-02	-	6.99e-02	-	1.83e-01	-

Table A.4: L1 errors for F-CAB for case JS for different CFL

Grid points	L1 error	OOA	L1 error	OOA	L1 error	OOA
	CFL=0.1		CFL=0.2		CFL=0.8	
6400	2.08e-04	1.82	1.42e-04	1.85	2.32e-05	2.02
3200	7.31e-04	1.65	5.14e-04	1.72	9.39e-05	2.03
1600	2.30e-03	1.47	1.70e-03	1.54	3.83e-04	2.07
800	6.35e-03	1.35	4.95e-03	1.33	1.60e-03	2.07
400	1.62e-02	0.99	1.24e-02	1.09	6.74e-03	2.12
200	3.23e-02	-	2.65e-02	-	2.93e-02	-

Table A.5: L1 errors for F-CAB for case A for different CFL

Grid points	L1 error	OOA	L1 error	OOA	L1 error	OOA
	CFL=0.1		CFL=0.2		CFL=0.8	
6400	4.89e-04	1.83	3.35e-04	1.86	5.05e-05	2.03
3200	1.73e-03	1.66	1.21e-03	1.71	2.06e-04	2.04
1600	5.47e-03	1.31	3.96e-03	1.47	8.44e-04	2.05
800	1.36e-02	1.52	1.10e-02	1.41	3.50e-03	1.99
400	3.89e-02	0.98	2.91e-02	1.22	1.39e-02	2.18
200	7.65e-02	-	6.77e-02	-	6.29e-02	-

Table A.6: L1 errors for F-CAB for case B for different CFL

Grid points	L1 error	OOA	L1 error	OOA	L1 error	OOA
	CFL=0.1		CFL=0.2		CFL=0.8	
6400	1.44e-04	1.86	9.78e-05	1.88	1.87e-05	2.01
3200	5.23e-04	1.74	3.60e-04	1.76	7.54e-05	2.05
1600	1.74e-03	1.58	1.22e-03	1.74	3.12e-04	2.00
800	5.23e-03	1.07	4.07e-03	1.09	1.25e-03	2.04
400	1.10e-02	1.03	8.69e-03	1.13	5.11e-03	2.04
200	2.25e-02	-	1.91e-02	-	2.10e-02	-

Table A.7: L1 errors for F-CAB for case C for different CFL

Grid points	L1 error	OOA	L1 error	OOA	L1 error	OOA
	CFL=0.1		CFL=0.2		CFL=0.8	
6400	1.32e-03	0.67	1.15e-03	0.67	2.35e-03	0.59
3200	2.10e-03	0.67	1.83e-03	0.67	3.53e-03	0.57
1600	3.33e-03	0.67	2.91e-03	0.67	5.24e-03	0.60
800	5.28e-03	0.67	4.61e-03	0.66	7.93e-03	0.59
400	8.37e-03	0.66	7.31e-03	0.66	1.19e-02	0.60
200	1.33e-02	-	1.16e-02	-	1.80e-02	-

Table A.8: L1 errors for F-CAB for case R for different CFL

Grid points	L1 error	OOA	L1 error	OOA	L1 error	OOA
	CFL=0.1		CFL=0.2		CFL=0.8	
6400	4.64e-05	1.25	3.59e-05	1.25	2.36e-05	1.26
3200	1.10e-04	1.24	8.54e-05	1.24	5.66e-05	1.29
1600	2.60e-04	1.20	2.01e-04	1.22	1.39e-04	1.24
800	5.98e-04	1.17	4.69e-04	1.19	3.27e-04	1.22
400	1.35e-03	1.14	1.07e-03	1.15	7.62e-04	1.34
200	2.97e-03	-	2.38e-03	-	1.93e-03	-

Table A.9: L1 errors for F-CAB for case T for different CFL

Grid points	L1 error	OOA	L1 error	OOA	L1 error	OOA
	CFL=0.1		CFL=0.2		CFL=0.8	
6400	9.23e-06	1.90	6.29e-06	1.90	1.31e-06	1.74
3200	3.44e-05	1.81	2.34e-05	1.88	4.38e-06	1.87
1600	1.21e-04	1.68	8.60e-05	1.69	1.60e-05	1.98
800	3.87e-04	1.23	2.77e-04	1.47	6.35e-05	1.97
400	9.08e-04	1.65	7.67e-04	1.43	2.49e-04	1.95
200	2.84e-03	-	2.07e-03	-	9.62e-04	-

Table A.10: L1 errors for F-CAB for case Y for different CFL

Grid points	L1 error	OOA	L1 error	OOA	L1 error	OOA
	CFL=0.1		CFL=0.2		CFL=0.8	
6400	1.39e-03	0.74	1.20e-03	0.73	2.35e-03	0.59
3200	2.32e-03	0.78	1.99e-03	0.77	3.55e-03	0.59
1600	3.98e-03	0.78	3.40e-03	0.76	5.34e-03	0.65
800	6.84e-03	0.91	5.74e-03	0.92	8.36e-03	0.71
400	1.28e-02	0.60	1.08e-02	0.70	1.36e-02	0.97
200	1.95e-02	-	1.76e-02	-	2.67e-02	-

Table A.11: L1 errors for F-CAB for case Z for different CFL

A.1.3 OOA of MR-CAB-DISP scheme

Grid points	L1 error	OOA	L1 error	OOA	L1 error	OOA
	CFL=0.1		CFL=0.2		CFL=0.8	
6400	7.66e-05	1.46	7.97e-05	2.05	1.21e-05	2.01
3200	2.11e-04	2.25	3.30e-04	2.20	4.87e-05	2.13
1600	1.00e-03	1.47	1.51e-03	1.77	2.13e-04	2.04
800	2.78e-03	2.24	5.15e-03	1.87	8.72e-04	2.00
400	1.31e-02	-0.58	1.89e-02	0.63	3.48e-03	2.16
200	8.78e-03	-	2.92e-02	-	1.56e-02	-

Table A.12: L1 errors for MR-CAB with dispersion for case BB for different CFL

Grid points	L1 error	OOA	L1 error	OOA	L1 error	OOA
	CFL=0.1		CFL=0.2		CFL=0.8	
6400	1.93e-03	0.72	3.08e-03	0.79	5.73e-03	0.90
3200	3.19e-03	0.81	5.35e-03	0.80	1.07e-02	0.92
1600	5.59e-03	0.83	9.34e-03	0.84	2.03e-02	0.94
800	9.93e-03	0.88	1.67e-02	0.89	3.89e-02	0.95
400	1.82e-02	0.96	3.09e-02	0.94	7.51e-02	0.94
200	3.55e-02	-	5.92e-02	-	1.44e-01	-

Table A.13: L1 errors for MR-CAB with dispersion for case JS for different CFL

Grid points	L1 error	OOA	L1 error	OOA	L1 error	OOA
	CFL=0.1		CFL=0.2		CFL=0.8	
6400	2.16e-05	2.01	2.79e-05	1.97	5.01e-06	2.08
3200	8.67e-05	1.99	1.09e-04	2.00	2.12e-05	2.03
1600	3.45e-04	1.80	4.36e-04	1.82	8.63e-05	1.94
800	1.20e-03	1.44	1.54e-03	1.52	3.31e-04	2.17
400	3.26e-03	1.35	4.40e-03	1.15	1.49e-03	2.54
200	8.29e-03	-	9.78e-03	-	8.70e-03	-

Table A.14: L1 errors for MR-CAB with dispersion for case A for different CFL

Grid points	L1 error	OOA	L1 error	OOA	L1 error	OOA
	CFL=0.1		CFL=0.2		CFL=0.8	
6400	5.50e-05	1.98	7.36e-05	2.17	1.28e-05	1.99
3200	2.17e-04	1.92	3.32e-04	1.52	5.12e-05	2.03
1600	8.21e-04	1.84	9.53e-04	2.10	2.10e-04	2.04
800	2.95e-03	1.10	4.08e-03	1.35	8.64e-04	2.05
400	6.31e-03	1.23	1.04e-02	1.43	3.58e-03	2.34
200	1.48e-02	-	2.79e-02	-	1.81e-02	-

Table A.15: L1 errors for MR-CAB with dispersion for case B for different CFL

Grid points	L1 error	OOA	L1 error	OOA	L1 error	OOA
	CFL=0.1		CFL=0.2		CFL=0.8	
6400	1.26e-05	1.99	1.56e-05	1.90	3.04e-06	2.02
3200	5.03e-05	1.98	5.84e-05	2.01	1.24e-05	1.94
1600	1.98e-04	1.94	2.35e-04	1.88	4.75e-05	1.98
800	7.64e-04	1.51	8.63e-04	1.24	1.87e-04	2.46
400	2.18e-03	2.18	2.04e-03	1.81	1.03e-03	2.52
200	9.88e-03	-	7.18e-03	-	5.92e-03	-

Table A.16: L1 errors for MR-CAB with dispersion for case C for different CFL

Grid points	L1 error	OOA	L1 error	OOA	L1 error	OOA
	CFL=0.1		CFL=0.2		CFL=0.8	
6400	5.82e-04	0.79	8.50e-04	0.69	8.30e-04	0.73
3200	1.01e-03	0.87	1.37e-03	0.68	1.38e-03	0.72
1600	1.84e-03	0.89	2.20e-03	0.66	2.26e-03	0.71
800	3.42e-03	0.83	3.47e-03	0.65	3.69e-03	0.69
400	6.06e-03	0.84	5.46e-03	0.64	5.95e-03	0.75
200	1.09e-02	-	8.51e-03	-	1.00e-02	-

Table A.17: L1 errors for MR-CAB with dispersion for case R for different CFL

Grid points	L1 error	OOA	L1 error	OOA	L1 error	OOA
	CFL=0.1		CFL=0.2		CFL=0.8	
6400	9.44e-06	1.37	1.21e-05	1.26	7.74e-06	1.38
3200	2.45e-05	1.33	2.88e-05	1.25	2.01e-05	1.34
1600	6.16e-05	1.37	6.84e-05	1.31	5.11e-05	1.33
800	1.59e-04	1.40	1.70e-04	1.12	1.29e-04	1.20
400	4.20e-04	1.38	3.69e-04	1.47	2.95e-04	1.78
200	1.10e-03	-	1.02e-03	-	1.01e-03	-

Table A.18: L1 errors for MR-CAB with dispersion for case T for different CFL

Grid points	L1 error	OOA	L1 error	OOA	L1 error	OOA
	CFL=0.1		CFL=0.2		CFL=0.8	
6400	1.11e-06	2.00	1.44e-06	1.43	6.49e-07	1.63
3200	4.47e-06	1.73	3.87e-06	2.38	2.01e-06	1.65
1600	1.48e-05	2.21	2.01e-05	1.85	6.31e-06	1.75
800	6.84e-05	1.70	7.24e-05	1.60	2.12e-05	1.88
400	2.22e-04	0.65	2.20e-04	1.84	7.79e-05	2.12
200	3.47e-04	-	7.89e-04	-	3.40e-04	-

Table A.19: L1 errors for MR-CAB with dispersion for case Y for different CFL

Grid points	L1 error	OOA	L1 error	OOA	L1 error	OOA
	CFL=0.1		CFL=0.2		CFL=0.8	
6400	5.87e-04	0.82	8.60e-04	0.71	8.32e-04	0.73
3200	1.04e-03	0.93	1.41e-03	0.72	1.38e-03	0.73
1600	1.97e-03	0.97	2.33e-03	0.72	2.29e-03	0.72
800	3.86e-03	0.78	3.83e-03	0.83	3.78e-03	0.74
400	6.62e-03	0.97	6.83e-03	0.78	6.33e-03	1.04
200	1.30e-02	-	1.17e-02	-	1.30e-02	-

Table A.20: L1 errors for MR-CAB with dispersion for case Z for different CFL

A.1.4 OOA of P-CAB scheme

Grid points	L1 error	OOA	L1 error	OOA	L1 error	OOA
	CFL=0.1		CFL=0.2		CFL=0.8	
6400	3.32e-04	1.99	2.22e-04	1.99	5.60e-05	1.99
3200	1.32e-03	2.00	8.83e-04	2.00	2.22e-04	1.99
1600	5.28e-03	2.00	3.52e-03	2.00	8.82e-04	2.00
800	2.11e-02	1.98	1.41e-02	1.99	3.52e-03	2.00
400	8.33e-02	1.57	5.59e-02	1.82	1.41e-02	2.00
200	2.47e-01	-	1.97e-01	-	5.65e-02	-

Table A.21: L1 errors for P-CAB for case BB for different CFL

Grid points	L1 error	OOA	L1 error	OOA	L1 error	OOA
	CFL=0.1		CFL=0.2		CFL=0.8	
6400	2.48e-02	0.50	2.24e-02	0.49	1.76e-02	0.59
3200	3.51e-02	0.51	3.14e-02	0.50	2.65e-02	0.63
1600	4.98e-02	0.62	4.44e-02	0.57	4.10e-02	0.70
800	7.67e-02	0.56	6.60e-02	0.63	6.64e-02	0.74
400	1.13e-01	0.72	1.02e-01	0.63	1.11e-01	0.79
200	1.86e-01	-	1.59e-01	-	1.92e-01	-

Table A.22: L1 errors for P-CAB for case JS for different CFL

Grid points	L1 error	OOA	L1 error	OOA	L1 error	OOA
	CFL=0.1		CFL=0.2		CFL=0.8	
6400	1.30e-04	2.00	8.67e-05	2.00	2.17e-05	2.00
3200	5.20e-04	2.00	3.47e-04	2.00	8.67e-05	2.00
1600	2.08e-03	2.00	1.39e-03	2.00	3.47e-04	2.00
800	8.32e-03	1.95	5.55e-03	1.98	1.39e-03	2.01
400	3.21e-02	1.22	2.19e-02	1.61	5.60e-03	2.00
200	7.48e-02	-	6.68e-02	-	2.24e-02	-

Table A.23: L1 errors for P-CAB for case A for different CFL

Grid points	L1 error	OOA	L1 error	OOA	L1 error	OOA
	CFL=0.1		CFL=0.2		CFL=0.8	
6400	2.74e-04	2.00	1.83e-04	2.00	4.59e-05	1.99
3200	1.09e-03	2.00	7.30e-04	2.00	1.83e-04	2.00
1600	4.38e-03	2.00	2.92e-03	2.00	7.30e-04	2.00
800	1.75e-02	1.99	1.17e-02	1.97	2.93e-03	2.01
400	6.94e-02	1.29	4.57e-02	1.77	1.18e-02	1.99
200	1.70e-01	-	1.56e-01	-	4.69e-02	-

Table A.24: L1 errors for P-CAB for case B for different CFL

Grid points	L1 error	OOA	L1 error	OOA	L1 error	OOA
	CFL=0.1		CFL=0.2		CFL=0.8	
6400	1.06e-04	2.00	7.06e-05	2.00	1.77e-05	2.00
3200	4.24e-04	2.00	2.83e-04	2.00	7.07e-05	2.00
1600	1.70e-03	2.01	1.13e-03	1.99	2.83e-04	2.01
800	6.82e-03	1.91	4.51e-03	1.99	1.14e-03	2.01
400	2.56e-02	1.55	1.80e-02	1.59	4.60e-03	2.02
200	7.49e-02	-	5.39e-02	-	1.86e-02	-

Table A.25: L1 errors for P-CAB for case C for different CFL

Grid points	L1 error	OOA	L1 error	OOA	L1 error	OOA
	CFL=0.1		CFL=0.2		CFL=0.8	
6400	1.18e-02	0.47	9.85e-03	0.46	5.42e-03	0.46
3200	1.64e-02	0.47	1.35e-02	0.47	7.44e-03	0.49
1600	2.27e-02	0.45	1.88e-02	0.44	1.05e-02	0.44
800	3.10e-02	0.45	2.55e-02	0.48	1.42e-02	0.53
400	4.23e-02	0.49	3.55e-02	0.38	2.05e-02	0.49
200	5.94e-02	-	4.61e-02	-	2.88e-02	-

Table A.26: L1 errors for P-CAB for case R for different CFL

Grid points	L1 error	OOA	L1 error	OOA	L1 error	OOA
	CFL=0.1		CFL=0.2		CFL=0.8	
6400	8.35e-05	1.26	6.29e-05	1.26	2.45e-05	1.25
3200	2.00e-04	1.26	1.51e-04	1.26	5.83e-05	1.27
1600	4.81e-04	1.22	3.61e-04	1.21	1.41e-04	1.20
800	1.12e-03	1.21	8.36e-04	1.20	3.24e-04	1.20
400	2.59e-03	1.40	1.92e-03	1.34	7.42e-04	1.47
200	6.86e-03	-	4.88e-03	-	2.05e-03	-

Table A.27: L1 errors for P-CAB for case T for different CFL

Grid points	L1 error	OOA	L1 error	OOA	L1 error	OOA
	CFL=0.1		CFL=0.2		CFL=0.8	
6400	1.28e-05	0.90	1.66e-05	0.66	8.54e-06	0.66
3200	2.39e-05	1.67	2.61e-05	1.12	1.35e-05	0.94
1600	7.60e-05	1.97	5.69e-05	1.82	2.60e-05	1.26
800	2.98e-04	2.00	2.01e-04	1.99	6.22e-05	1.72
400	1.19e-03	1.97	7.95e-04	1.97	2.05e-04	1.98
200	4.67e-03	-	3.10e-03	-	8.09e-04	-

Table A.28: L1 errors for P-CAB for case Y for different CFL

Grid points	L1 error	OOA	L1 error	OOA	L1 error	OOA
	CFL=0.1		CFL=0.2		CFL=0.8	
6400	1.24e-02	0.47	1.08e-02	0.47	5.60e-03	0.47
3200	1.72e-02	0.48	1.49e-02	0.46	7.76e-03	0.48
1600	2.39e-02	0.46	2.05e-02	0.49	1.08e-02	0.48
800	3.30e-02	0.47	2.87e-02	0.47	1.51e-02	0.55
400	4.56e-02	0.42	3.97e-02	0.51	2.22e-02	0.64
200	6.12e-02	-	5.63e-02	-	3.46e-02	-

Table A.29: L1 errors for P-CAB for case Z for different CFL

A.1.5 OOA of R-CAB scheme

Grid points	L1 error	OOA	L1 error	OOA	L1 error	OOA
	CFL=0.1		CFL=0.2		CFL=0.8	
6400	1.43e-05	1.99	9.43e-06	2.07	3.03e-06	2.00
3200	5.67e-05	2.00	3.96e-05	2.08	1.21e-05	2.12
1600	2.27e-04	2.07	1.68e-04	2.03	5.27e-05	2.25
800	9.53e-04	2.32	6.87e-04	2.28	2.51e-04	2.28
400	4.75e-03	2.86	3.34e-03	2.79	1.22e-03	2.52
200	3.46e-02	-	2.31e-02	-	7.00e-03	-

Table A.30: L1 errors for R-CAB with dispersion for case 1 for different CFL

Grid points	L1 error	OOA	L1 error	OOA	L1 error	OOA
	CFL=0.1		CFL=0.2		CFL=0.8	
6400	5.01e-03	0.56	5.01e-03	0.61	9.02e-03	0.74
3200	7.40e-03	0.59	7.63e-03	0.62	1.51e-02	0.78
1600	1.11e-02	0.65	1.17e-02	0.68	2.58e-02	0.83
800	1.75e-02	0.69	1.88e-02	0.68	4.59e-02	0.85
400	2.83e-02	0.89	3.03e-02	0.90	8.26e-02	0.86
200	5.26e-02	-	5.63e-02	-	1.50e-01	-

Table A.31: L1 errors for R-CAB with dispersion for case 2 for different CFL

Grid points	L1 error	OOA	L1 error	OOA	L1 error	OOA
	CFL=0.1		CFL=0.2		CFL=0.8	
6400	5.22e-06	2.02	3.49e-06	2.02	9.08e-07	2.05
3200	2.11e-05	2.06	1.41e-05	2.07	3.76e-06	2.19
1600	8.81e-05	2.21	5.93e-05	2.22	1.72e-05	2.24
800	4.07e-04	2.63	2.75e-04	2.63	8.10e-05	2.82
400	2.53e-03	3.11	1.70e-03	3.18	5.70e-04	2.91
200	2.19e-02	-	1.54e-02	-	4.28e-03	-

Table A.32: L1 errors for R-CAB with dispersion for case A for different CFL

Grid points	L1 error	OOA	L1 error	OOA	L1 error	OOA
	CFL=0.1		CFL=0.2		CFL=0.8	
6400	1.13e-05	1.98	7.64e-06	1.97	2.15e-06	1.89
3200	4.47e-05	2.04	3.00e-05	2.04	7.97e-06	2.07
1600	1.84e-04	2.18	1.24e-04	2.19	3.35e-05	2.31
800	8.33e-04	2.54	5.66e-04	2.55	1.66e-04	2.45
400	4.85e-03	3.14	3.31e-03	3.11	9.05e-04	3.15
200	4.26e-02	-	2.85e-02	-	8.03e-03	-

Table A.33: L1 errors for R-CAB with dispersion for case B for different CFL

Grid points	L1 error	OOA	L1 error	OOA	L1 error	OOA
	CFL=0.1		CFL=0.2		CFL=0.8	
6400	4.27e-06	2.02	2.86e-06	2.03	7.70e-07	2.12
3200	1.74e-05	2.08	1.17e-05	2.09	3.35e-06	2.16
1600	7.36e-05	2.30	4.97e-05	2.31	1.50e-05	2.29
800	3.63e-04	2.90	2.46e-04	2.88	7.36e-05	2.97
400	2.70e-03	2.10	1.81e-03	2.37	5.76e-04	3.15
200	1.16e-02	-	9.32e-03	-	5.12e-03	-

Table A.34: L1 errors for R-CAB with dispersion for case C for different CFL

Grid points	L1 error	OOA	L1 error	OOA	L1 error	OOA
	CFL=0.1		CFL=0.2		CFL=0.8	
6400	2.59e-03	0.52	2.37e-03	0.53	2.32e-03	0.51
3200	3.72e-03	0.51	3.41e-03	0.51	3.30e-03	0.48
1600	5.28e-03	0.52	4.86e-03	0.56	4.62e-03	0.51
800	7.56e-03	0.58	7.17e-03	0.50	6.59e-03	0.57
400	1.13e-02	0.45	1.02e-02	0.51	9.78e-03	0.49
200	1.54e-02	-	1.45e-02	-	1.37e-02	-

Table A.35: L1 errors for R-CAB with dispersion for case R for different CFL

Grid points	L1 error	OOA	L1 error	OOA	L1 error	OOA
	CFL=0.1		CFL=0.2		CFL=0.8	
6400	1.70e-05	1.33	1.46e-05	1.35	7.15e-06	1.37
3200	4.27e-05	1.32	3.72e-05	1.34	1.84e-05	1.32
1600	1.07e-04	1.27	9.39e-05	1.33	4.61e-05	1.32
800	2.57e-04	1.24	2.36e-04	1.18	1.15e-04	1.20
400	6.07e-04	1.42	5.35e-04	1.41	2.64e-04	2.02
200	1.63e-03	-	1.42e-03	-	1.07e-03	-

Table A.36: L1 errors for R-CAB with dispersion for case T for different CFL

Grid points	L1 error	OOA	L1 error	OOA	L1 error	OOA
	CFL=0.1		CFL=0.2		CFL=0.8	
6400	3.40e-06	0.73	4.09e-06	0.67	2.76e-06	0.59
3200	5.62e-06	0.64	6.50e-06	0.64	4.16e-06	0.68
1600	8.73e-06	0.91	1.01e-05	0.85	6.67e-06	0.72
800	1.64e-05	1.88	1.82e-05	1.36	1.10e-05	0.87
400	6.04e-05	2.69	4.66e-05	2.48	2.01e-05	2.05
200	3.89e-04	-	2.60e-04	-	8.33e-05	-

Table A.37: L1 errors for R-CAB with dispersion for case Y for different CFL

Grid points	L1 error	OOA	L1 error	OOA	L1 error	OOA
	CFL=0.1		CFL=0.2		CFL=0.8	
6400	3.52e-03	0.52	3.20e-03	0.48	2.35e-03	0.65
3200	5.06e-03	0.52	4.45e-03	0.55	3.70e-03	0.36
1600	7.24e-03	0.53	6.53e-03	0.51	4.75e-03	0.65
800	1.05e-02	0.57	9.32e-03	0.52	7.45e-03	0.50
400	1.56e-02	0.74	1.34e-02	0.74	1.05e-02	0.65
200	2.60e-02	-	2.24e-02	-	1.65e-02	-

Table A.38: L1 errors for R-CAB with dispersion for case Z for different CFL

References

Blazek, J., 2005. Computational Fluid Dynamics: Principles and Applications, 2nd Edition. Elsevier. 54

Bogey, C., Bailly, C., 2004. A family of low dispersive and low dissipative explicit schemes for flow and noise computations. Journal of Computational Physics 194 (1), 194 – 214. 4, 5, 27, 76

Bogey, C., de Cacqueray, N., Bailly, C., 2009. A shock-capturing methodology based on adaptative spatial filtering for high-order non-linear computations. Journal of Computational Physics 228 (5), 1447 – 1465. 6

Chintagunta, A., Naghibi, S., Karabasov, S., 2017. Flux-corrected dispersion-improved cabaret schemes for linear and nonlinear wave propagation problems. Computers & Fluids. 7, 9

Cockburn, B., Karniadakis, G. E., Shu, C.-W., 2000. The development of discontinuous galerkin methods. In: Discontinuous Galerkin Methods. Springer, pp. 3–50. 6

Colonius, T., Lele, S. K., 2004. Computational aeroacoustics: progress on nonlinear problems of sound generation. Progress in Aerospace Sciences 40 (6), 345 – 416. 1

Crumpton, P., Mackenzie, J., Morton, K., 1993. Cell vertex algorithms for the compressible navier-stokes equations. Journal of Computational Physics 109 (1), 1 – 15. 53, 54

Danilin, A., 2013. A fourth order space-time scheme for the numerical solution of linear advection equation. Preprint IBRAE 03. 8, 24

Doty, M., McLaughlin, D., Jul 2003. Acoustic and mean flow measurements of high-speed, helium-air mixture jets. International Journal of Aeroacoustics 2 (3), 293–333. 117

Dumbser, M., Zanotti, O., Loubère, R., Diot, S., 2014. A posteriori subcell limiting of the discontinuous galerkin finite element method for hyperbolic conservation laws. Journal of Computational Physics 278, 47–75. 6

Faranosov, G. A., Goloviznin, V. M., Karabasov, S. A., Kondakov, V. G., Kopiev, V. F., Zaitsev, M. A., 2013a. Cabaret method on unstructured hexahedral grids for jet noise computation. Computers & Fluids 88 (Supplement C), 165 – 179. 8, 14

Faranosov, G. A., Goloviznin, V. M., Karabasov, S. A., Kondakov, V. G., Kopiev, V. F., Zaitsev, M. A., 2013b. CABARET method on unstructured hexahedral grids for jet noise computation. Computers and Fluids 88. 52, 117

Gnu, 2014. Gnu compiler collection, ver. 4.8.2. %urlhttp://www.gnu.org/. 117

Goloviznin, V., Samarskii, A., 1998a. Difference approximation of convective transport with spatial splitting of time derivative 10, 86–100. 7, 9, 18, 123

Goloviznin, V., Samarskii, A., 1998b. Some properties of the difference scheme "CABARET" 10. 9, 11

Haider, F., Bertier, N., Courbet, B., Vuillot, F., Croisille, J., 2015. Application of a high order finite volume scheme on unstructured grids to fluid dynamics and aerothermochemistry. hal-01111360. 4

Harten, A., 1983. High resolution schemes for hyperbolic conservation laws. Journal of computational physics 49 (3), 357–393. 4

Harten, A., Engquist, B., Osher, S., Chakravarthy, S. R., 1997. Uniformly high order accurate essentially non-oscillatory schemes, iii. Journal of Computational Physics 131 (1), 3 – 47. 6

Hirsch, C. P., 2007. Numerical computation of internal and external flows. volume 1. , fundamentals of computational fluid dynamics. Butterworth-Heinemann. 14, 115

Huang, X., Zhang, X., Richards, S. K., 2008. Adaptive mesh refinement computation of acoustic radiation from an engine intake. Aerospace Science and Technology 12 (5), 418–426. 5

Jiang, G.-S., Shu, C.-W., 1996. Efficient implementation of weighted eno schemes. Journal of computational physics 126 (1), 202–228. 76

Kalyan, A., 2015. private communication. 117

Karabasov, S., 2015. private communication. 54

Karabasov, S., Goloviznin, V., 2009. Compact accurately boundary-adjusting high-resolution technique for fluid dynamics. Journal of Computational Physics 228 (19), 7426–7451. 7, 9, 20, 24, 27, 29, 30, 35

Karabasov, Sergey A.and Goloviznin, V. M., Dec 2007. New Efficient High-Resolution Method for Nonlinear Problems in Aeroacoustics. AIAA Journal 45 (12), 2861–2871. 9

Lele, S. K., 1997. Computational aeroacoustics: a review. AIAA paper 18, 1997. 3

Leylekian, L., Lebrun, M., Lempereur, P., 2014. An overview of aircraft noise reduction technologies. AerospaceLab (6), p–1. 1

Liseikin, V. D., 1999. Grid generation methods. Vol. 1. Springer. 6

Rienstra, S. W., Hirschberg, A., 2004. An introduction to acoustics. Eindhoven University of Technology 18, 19. 93

Schlichting, H., 2003. Boundary layer theory. Springer. 116

Schoenwald, N., Panek, L., Richter, C., Thiele, F., 2007. Investigation of sound radiation from a scarfed intake by CAA-FWH simulations using overset grids. AIAA Paper 3524, 2007. 5

Smears, I., 2016. Robust and efficient preconditioners for the discontinuous galerkin time-stepping method. IMA Journal of Numerical Analysis 37 (4), 1961–1985. 7

Sod, G. A., 1978. A survey of several finite difference methods for systems of nonlinear hyperbolic conservation laws. Journal of Computational Physics 27 (1), 1 – 31. 112

Tam, C. K., 2004. Computational aeroacoustics: An overview of computational challenges and applications. International Journal of Computational Fluid Dynamics 18 (6), 547–567. 1

Tam, C. K., Webb, J. C., 1993a. Dispersion-relation-preserving finite difference schemes for computational acoustics. Journal of computational physics 107 (2), 262–281. 5

Tam, C. K., Webb, J. C., 1993b. Dispersion-relation-preserving finite difference schemes for computational acoustics. Journal of computational physics 107 (2), 262–281. 58, 76, 124

Tam, C. K. W., Oct 1995. Computational aeroacoustics - issues and methods. AIAA Journal 33 (10), 1788–1796. 3

Wagner, C., Hüttl, T., Sagaut, P., 2007. Large-Eddy Simulation for Acoustics. Cambridge Aerospace Series. Cambridge University Press. 1

Zaman, K., Bridges, J., Huff, D., 2011. Evolution from 'tabs' to 'chevron technology'-a review. International Journal of Aeroacoustics 10 (5-6), 685–709. 1